4D transverse and 2D longitudinal phase space characterization of high brightness electron beams at PITZ

Dissertation
zur Erlangung des Doktorgrades
an der Fakultät für Mathematik, Informatik und Naturwissenschaften
Fachbereich Physik
der Universität Hamburg

vorgelegt von
Namra Aftab

Hamburg
2024

Gutachter/innen der Dissertation:	Prof. Dr. Wolfgang Hillert Dr. Mikhail Krasilnikov
Zusammensetzung der Prüfungskommission:	Prof. Dr. Wolfgang Hillert Dr. Mikhail Krasilnikov Prof. Dr. Florian Grüner Prof. Dr. Daniele Pfannkuche Dr. Klaus Floettmann
Vorsitzende/r der Prüfungskommission:	Prof. Dr. Daniele Pfannkuche
Datum der Disputation:	11.03.2024
Vorsitzender des Fach- Promotionsausschusses Physik:	Prof. Dr. Markus Drescher
Leiter des Fachbereichs Physik:	Prof. Dr. Wolfgang J. Parak
Dekan der Fakultät MIN:	Prof. Dr.-Ing. Norbert Ritter

Dedication

To my parents, Aftab and Naheed, and my sisters, Hajira, Iqra and Qurat-ul-Ain, for their emotional support and believing in me when I was doubting myself.
To my husband Rehan and my little girl Rania, for being in my life.

Abstract

In the scope of this thesis work, the existing diagnostic setups for the transverse and longitudinal phase space characterization at the Photo Injector Test facility at DESY in Zeuthen (PITZ) have been utilized to obtain detailed and reliable results. PITZ, being a test facility for European XFEL and FLASH, needs to do detailed characterization of electron beams to ensure that they meet the requirements of the FELs, i.e., small transverse emittance and energy spread as well as high peak current.

For the reconstruction of the horizontal and vertical phase spaces, PITZ utilizes a slit scan technique as a standard tool because of its space charge dominated electron beams. A novel method for 4 dimensional transverse phase space characterization, known as virtual pepper pot, is proposed that can give insight to the transverse beam phase space coupling. It utilizes the horizontal and vertical single slit scan data to form pepper pot like beamlets. The systematic error of the methodology is explored and the loss of signal at the halo of the horizontal and vertical beamlets due to low signal to noise ratio is considered in the algorithm.

To reconstruct the Longitudinal Phase Space (LPS) before the booster accelerating structure, a tomographic reconstruction method called algebraic reconstruction technique was utilized, but the LPS results showed many artefacts. In this thesis, methodical studies were done to improve the existing LPS tomography technique. Some core concerns were addressed e.g. booster phase range, space charge effects and noisy artefacts in results. The reconstruction method adopted was an image space reconstruction algorithm which showed promising results owing to assurance of non-negative solution. Moreover, the initial guess of LPS for iterations was established from low energy section momentum measurements to give a unique solution.

Kurzfassung

Eine detaillierte Charakterisierung der Elektronenstrahlen aus einem Photoinjektor ist von entscheidender Bedeutung, um sicherzustellen, dass sie die Anforderungen der FELs erfüllen, d.h. eine geringe transversale Emittanz und Energieverteilung sowie ein hoher Spitzenstrom. Im Rahmen dieser Arbeit wurden die bestehenden Diagnoseeinrichtungen für die transversale und longitudinale Phasenraumcharakterisierung an der Photoinjektor-Testanlage bei DESY in Zeuthen (PITZ) genutzt und verbessert, um detaillierte und zuverlässige Ergebnisse zu erhalten.
Für die Rekonstruktion der horizontalen und vertikalen Phasenräume verwendet PITZ eine Einzelschlitzabtastung als Standardwerkzeug, da die Elektronenstrahlen von Raumladung dominiert werden. Zur vierdimensionalen Charakterisierung des transversalen Phasenraums, wird eine neue Methode vorgeschlagen, die als virtueller Pfefferstreuer bekannt ist und einen Einblick in die Phasenraumkopplung der transversalen Strahlen geben kann. Sie nutzt die horizontalen und vertikalen Einzelspalt-Scandaten, um durch sorgfältiges Kreuzen und Nachbearbeiten von Beamlets pfefferstreuerartige Beamlets zu bilden. Der Signalverlust an den Rundern der Beamlets aufgrund des geringen Signal-Rausch-Verhältnisses wird im Algorithmus berücksichtigt, und der systematische Fehler, der sich aus der Kreuzung der Beamlets ergibt, wird ebenfalls erforscht.
Zur Rekonstruktion des Longitudinalen Phasenraums (LPS) vor der Booster wurde eine tomografische Rekonstruktionsmethode, die so genannte algebraische Rekonstruktionstechnik, verwendet, wobei die LPS-Ergebnisse viele Artefakte aufwiesen. In dieser Arbeit wurden methodische Studien durchgeführt, um die bestehende LPS-Tomographietechnik zu verbessern. Es wurden einige zentrale Probleme angegangen, z. B. der Phasenbereich des Boosters, Raumladungseffekte und verrauschte Artefakte in den Ergebnissen. Als Rekonstruktionsmethode wurde ein Bildraum-

Rekonstruktionsalgorithmus verwendet, der vielversprechende Ergebnisse lieferte, da er eine nicht-negative Lösung garantiert. Außerdem wurde die anfängliche Abschätzung der LPS aus Messungen im Niederenergiebereich in den Algorithmus eingebracht um eindeutige Ergebnisse zu erzielen.

Contents

Chapter 1

Introduction

The exploration of the matter at the atomic and the sub-atomic level is an essential tool for accomplishing basic research in applied sciences [1]. This poses a demand on the measurement scales to be also of the same order. If one wants to measure the size of the atoms in the material under study, the length scale should be of the order of angstrom. Moreover, if one is interested to take a motion picture of chemical processes to unravel the structure and dynamics of complex molecular systems, e.g. proteins, the time scale should be of the order of femtoseconds. All of this has been made possible by the development of high brightness light sources.
A quick look into the history shows how these light sources have evolved over the years. In the 1960's, particle accelerators were built for nuclear and subnuclear physics. They were used parasitically as sources of photons for experiments in atomic, molecular and solid state physics and served as so called first generation light sources. Second generation light sources were designed to serve exclusively as light sources using the synchrotron radiation emitted in bending magnets [2]. In the 1990's, third generation light sources were developed [3, 4]. They provided more brilliant, quasi-monochromatic and tunable synchrotron radiation by the extensive use of the so called insertion devices such as e.g. undulators and wigglers. Free electron lasers (FELs) are the fourth generation light sources [5]. FELs produce radiation with full spatial coherence (i.e. laser-like) of extremely high peak brilliance (or spectral brightness) due to constructive interference between the fields radiated by the different electrons of the bunch [6]. The peak brilliance of the photon beams increased by eight orders of magnitude by going from synchrotron light

sources to FEL light sources. In case of long photon wavelengths, FELs can amplify the light intensity by an optical resonator based on two reflecting mirrors. For shorter wavelengths,i.e., in X-ray regime, it is challenging to produce mirrors with high reflectivity. Therefore, it is necessary to implement a single-pass high-gain process known as Self Amplified Spontaneous Emission (SASE) [7–12]. This requires a unique operational regime for the accelerator which puts stringent requirements on the quality and intensity of the electron beam. The source of the electron beam for most of these light sources is a photoinjector. The parameters of the radiation emitted from the light source depends upon the quality of the beam generated in the photoinjector.

The Photo Injector Test facility at DESY in Zeuthen (PITZ) is a unique accelerator facility owing to its dynamic parameter space. It was established to develop and characterize electron guns for the Free electron LASer in Hamburg (FLASH) and European X-ray Free Electron Laser (Eu-XFEL) [13](pp. 561-601). Now, it has expanded to perform proof-of-principle studies for an accelerator-based THz source [14] and to carry out research in state-of-the-art cancer radiation therapy with ultra-high dose rates [15]. The PITZ beamline allows methodological studies of electron beam phase space characterization techniques in parallel to simulations and analytical modelling.

Beam dynamics and diagnostic studies are a crucial part of research work at PITZ in order to characterize the electron beams, improve the beam transport and manipulate the beam properties, namely its distribution in the transverse phase space. The transverse phase space characterization is mainly done by a slit scan technique [16, 17]. A transverse deflecting structure is used to measure bunch length as well as slice energy spread [18]. The longitudinal phase space after the gun is measured by utilizing a tomographic reconstruction technique [19]. The goal of this thesis work was to further improve the beam characterization techniques in the transverse as well as the longitudinal phase spaces. The slit scan data used to characterize the horizontal and vertical phase space was combined and manipulated to develop Virtual Pepper Pot (VPP) technique. It was used to characterize the beam in 4D phase space to resolve additional coupling information between both transverse planes. For longitudinal phase space characterization, the existing method of tomography was updated. The experimental conditions and the reconstruction

algorithm were improved to achieve more reliable results.
The thesis is organized as follows: Chapter 2 describes the linear beam dynamics as well as the beam dynamics with space charge. The basic terms in accelerator physics like phase space, emittance and twiss parameters are described. The beam envelope equation is introduced to differentiate between space charge and emittance dominated beam. Since the acceleration of the beam to the relativistic velocities is based on RF technology, RF systems are introduced by describing the modes of operation for RF cavities. Finally RF photoinjectors are explained highlighting their main components. The importance of emittance optimization for FELs is also explained. Chapter 3 describes the PITZ facility. The components related to the thesis work are explained in more detail. Chapter 4 describes the virtual pepper pot technique that is utilized for 4D transverse phase space characterization and chapter 5 explains the tomographic reconstruction technique for longitudinal phase space characterization. Both of these chapters cover the major research work conducted during the thesis. They start with the analytical model, demonstrate the proof-of-principle simulations with methodological studies and finally display the experimental results. The end of the chapter summarizes the method and the findings along with the challenges and short-comings. Chapter 6 gives a conclusion and an outlook of the thesis work. It describes the improvements that can be made in the aforementioned methods and gives some ideas to mitigate the limitations of the techniques to make them more useful to the accelerator community in general, and PITZ in particular.

Chapter 2

Theoretical Background

This chapter provides an overview of beam dynamics in accelerator physics, with a focus on its application in photoinjectors. The charged particle dynamics in the presence of external electromagnetic fields as well as self-induced forces will be described. Radio Frequency (RF) technology used for particle acceleration is also briefly explained. Then, photoinjectors that produce and accelerate relativistic electrons utilizing RF cavities are discussed. The chapter concludes with a discussion of the application of RF photoinjector as a source in free electron lasers (FELs), as PITZ is a test facility for Eu-XFEL and FLASH.

2.1 Linear beam dynamics

When a particle beam is generated and accelerated in a linear or circular accelerator, it is necessary to focus it to keep the beam size finite as well as steer it to keep it on the nominal trajectory. A group of beam particles, known as bunch, always has a certain divergence and without proper measures, the bunch would be lost on the walls of the vacuum chamber. Therefore, external electric or magnetic fields are required to guide the particles. This phenomena is known as beam optics or beam dynamics. In our case, the Lorentz force is the only force which acts on the charged particles (we are neglecting e.g. gravitational forces). The Lorentz force equation tells us how charged particles interact with the electromagnetic fields. All the acceleration and guidance of particles in accelerator physics comes from the

Lorentz force $\vec{F_L}$, described by the expression:

$$\vec{F_L} = e(\vec{E} + \vec{v} \times \vec{B}). \tag{2.1}$$

where e is the charge, $\vec{E}$ is the electric field, $\vec{B}$ is the magnetic field and $\vec{v}$ is the velocity of the particles in the bunch. Lets assume that the particles go along the longitudinal direction, so their velocity $\vec{v} = (0, 0, v_s)$ and that the magnetic field has only transverse component $\vec{B} = (B_x, B_y, 0)$. For a particle moving through a horizontal plane in a magnetic field, there is a balance between Lorentz force $F_x = -ev_sB_y$ and the centrifugal force $F_r = mv_s^2/R$. Here m is the particle mass and R is the radius of curvature of the trajectory. Using $p = mv_s$, this balance of forces leads directly to the relation

$$\frac{1}{R(x, y, s)} = \frac{e}{p} B_y(x, y, s). \tag{2.2}$$

A coordinate system whose origin moves along the ideal trajectory and follows the longitudinal motion of the particle can be used to describe the motion of an individual particle. The x and y coordinates measure the transverse displacement from this trajectory, see Figure 2.1. Since transverse dimensions of the beam are

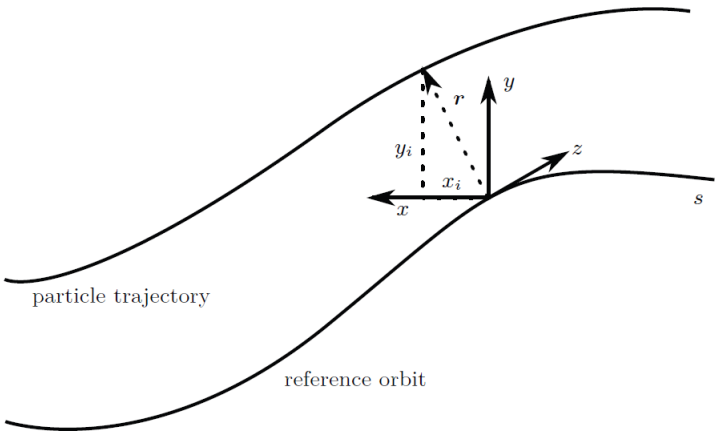

Figure 2.1: A coordinate system whose origin moves along the ideal trajectory [20].

small compared to the radius of curvature of the particle trajectory, we may expand

the magnetic field in the vicinity of the nominal trajectory:

$$B_y(x) = B_{y0} + \frac{dB_y}{dx}x + \frac{1}{2!}\frac{d^2B_y}{dx^2}x^2 + \frac{1}{3!}\frac{d^3B_y}{dx^3}x^3 + ... \tag{2.3}$$

Multiplying each side by e/p gives the accordingly normalized magnetic field around the beam as a sum of multipoles, each of which has a different effect on the path of the particle.

$$\begin{aligned}\frac{e}{p}B_y(x) =& \frac{e}{p}B_{y0} + \frac{e}{p}\frac{dB_y}{dx}x + \frac{e}{p}\frac{1}{2!}\frac{d^2B_y}{dx^2}x^2 + \frac{e}{p}\frac{1}{3!}\frac{d^3B_y}{dx^3}x^3 + ... \\ =& \frac{1}{R} + kx + \frac{1}{2!}mx^2 + \frac{1}{3!}ox^3 + ... \\ =& dipole + quadrupole + sextupole + octupole + ...\end{aligned} \tag{2.4}$$

When only the two lowest multipoles are considered in the Lorentz force acting on the beam (and thus limiting the approach to contributions scaling linearly with x and y),it is called **Linear beam optics**. Thus the Lorentz force consists of two contributions only: a constant dipole field which causes a bending of the trajectory on a circular orbit with curvature $1/R$ and a quadrupole field which acts like a focusing or defocusing lens with focal length $f = 1/(kL)$, where L is the length of the (thin) quadrupole and k is the quadrupole strength. Higher multipoles can be used to fix or adjust the field in specific cases, e.g., in circular accelerators to correct chromatic effects.

2.1.1 Equations of motion

In the presence of only s-dependent magnetic fields $B_x(s)$ and $B_y(s)$ from the dipole and quadrupole magnets, where s is the particle's longitudinal coordinate measured along the design trajectory, x is the horizontal and y is the vertical displacement from the design trajectory, respectively, one obtains:

$$B_x(s) = -g(s) \cdot y, \tag{2.5}$$

$$B_y(s) = B_0(s) - g(s) \cdot x. \tag{2.6}$$

Here the presence of only a vertical dipole field $B_0(s)$ and a quadrupole gradient $g(s)$ was considered. The equations of motion for a particle in such fields will have the following form [21].

$$x'' - \left(k(s) - \frac{1}{R(s)^2}\right) \cdot x = \frac{1}{R(s)}\delta p, \tag{2.7}$$

$$y'' + k(s) \cdot y = 0, \tag{2.8}$$

where $1/R(s) = (eB_0(s))/p_0$ is the Larmor radius and $k(s) = eg(s)/p_0$ is the normalized quadrupole gradient along the trajectory, p is the particle's momentum, p_0 the design reference momentum and the relative momentum deviation $\delta p = (p - p_0)/p_0$. For particles having the design momentum $p = p_0$, the equations of motion simplify to:

$$x'' + K_x(s) \cdot x = 0, \tag{2.9}$$

$$y'' + K_y(s) \cdot y = 0, \tag{2.10}$$

where $K_x(s) = \frac{1}{R(s)^2} - k(s)$ and $K_y(s) = k(s)$. Eq. 2.9 and 2.10 are also called Hill's equations of linear transverse particle motion (considering periodic K). A general solution for Eq. 2.9 for the particle motion in the x-plane can be written in the form [21].

$$x(s) = \sqrt{\epsilon_x \beta_x(s)}\cos(\psi + \psi_0), \tag{2.11}$$

where ϵ_x is called the horizontal (geometrical) emittance and $\beta_x(s)$ is called the horizontal beta function. A similar solution can be obtained for Eq. 2.10 [21].
The beta function $\beta(s)$ is related to the transverse size of the particle beam at the location s along the nominal beam trajectory and is defined in order to treat the optics independently from the intrinsic beam properties. The focusing by optical elements causes an oscillation around the design trajectory - the betatron oscillation, which advances with $\Delta\psi$, known as the phase advance. ψ_0 is the betatron phase at the initial position, $\psi + \psi_0$ is the betatron phase function at the current s position and the cosine term reveals that the particles undergo an oscillating motion in the transverse planes. The phase advance between two points s_0 and s_1 along the trajectory can be calculated as the difference $\Delta\psi$ between the values of the betatron

phase function at these two points and expressed as follows [21]:

$$\Delta\psi = \psi(s_1) - \psi(s_0) = \int_{s_0}^{s_1} \frac{1}{\beta(s)} dz. \tag{2.12}$$

2.1.2 Transverse emittance and twiss parameters

Each particle of a beam can be represented in the 4-dimensional transverse phase space by (x, p_x, y, p_y) at any point along the beamline. In the case when there is no coupling between the transverse particle motion, one can split the 4-dimensional phase space into two independent 2-dimensional phase spaces, (x, p_x) and (y, p_y). In beam physics, it is common to use particle's angles in the transverse planes and work in trace space (x, x') and (y, y'), where $x' = dx/ds$ and $y' = dy/ds$. In the paragraph that follows, only the 2-dimensional transverse phase space will be considered. 4-dimensional phase space will be discussed in chapter 4.
The beam transverse, geometric rms emittance ϵ characterizes the volume in the trace space which is occupied by the beam. Its numerical value, multiplied by π, is equal to the area occupied by the beam in the trace space.

$$\int_{ellipse} dx \cdot dx' = \pi\epsilon_x, \tag{2.13}$$

When the statistical rms definitions are used, it is calculated via [22]:

$$\epsilon_x = \sqrt{\langle x^2\rangle\langle x'^2\rangle - \langle xx'\rangle^2}, \tag{2.14}$$

from the second-order beam momenta $\langle x^2\rangle$, $\langle x'^2\rangle$ and $\langle xx'\rangle$ of the particle distribution. If the beam experiences acceleration during its propagation, the emittance described according to Eq. 2.14 is not conserved. For such cases the normalized transverse emittance can be introduced. The normalized rms emittance is defined as rms transverse emittance multiplied by $\beta\gamma = p_0/mc$:

$$\epsilon_{n,x} = \beta\gamma\epsilon_x, \tag{2.15}$$

where $\beta = v/c$, v is the particle speed, c is the speed of light, $\gamma = 1/\sqrt{(1-\beta^2)}$ is the relativistic Lorentz factor and m is the mass of the particle.

Liouville's theorem states that under the influence of conservative forces the particle density in the phase space stays constant [21]. The knowledge of the area occupied by the particles in the phase space at the beginning of a beam transport line allows to determine the location and distribution of the beam at any other place along the transport line without the need to calculate the trajectory of every individual particle. All the particles in the trace space can be represented by an equivalent ellipse – the trace space ellipse, described by [21]:

$$\gamma x^2 + 2\alpha x x' + \beta x'^2 = \epsilon_x, \tag{2.16}$$

where α, β, γ and ϵ are called the Twiss or Courant-Snyder parameters, see Figure 2.2. They determine the shape and orientation of the ellipse. The following equations are valid [21]:

$$\begin{aligned} \gamma\beta - \alpha^2 &= 1, \\ \alpha(s) &= -\frac{1}{2}\beta'(s), \end{aligned} \tag{2.17}$$

The parameters $\langle x^2 \rangle$, $\langle x'^2 \rangle$ and $\langle x x' \rangle$ can be calculated by [21]:

$$\begin{aligned} \langle x^2 \rangle &= \epsilon\beta, \\ \langle x'^2 \rangle &= \epsilon\gamma, \\ \langle x x' \rangle &= -\epsilon\alpha, \end{aligned} \tag{2.18}$$

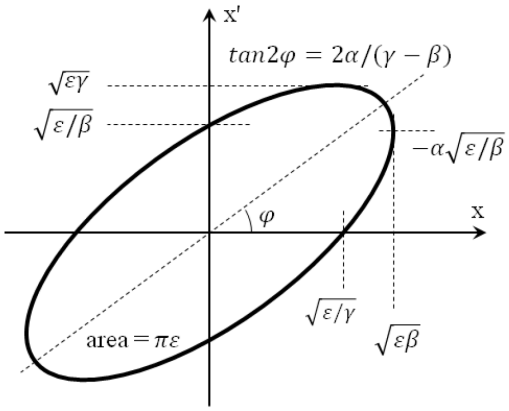

Figure 2.2: The particle distribution in trace space represented by an ellipse [21].

2.1.3 Particle trajectories and transfer matrices

The transformation of the particles' coordinates between two points s_0 and s_1 along a trajectory can be expressed by the six-dimensional transport matrix M since we have reduced the dynamics to a linear system:

$$\begin{bmatrix} x \\ x' \\ y \\ y' \\ z \\ \delta p \end{bmatrix}_{s_1} = \begin{bmatrix} M_{1,1} & \dots & M_{1,6} \\ \vdots & \ddots & \vdots \\ M_{6,1} & \dots & M_{6,6} \end{bmatrix} \cdot \begin{bmatrix} x \\ x' \\ y \\ y' \\ z \\ \delta p \end{bmatrix}_{s_0} , \tag{2.19}$$

where $x, x', y, y', z, \delta p$ are the particles spatial displacements, angular displacements and longitudinal relative momentum deviation at the start position s_0 and at the end position s_1. The matrix M is the transport matrix between the start and the end position. In the absence of correlation between the $x - y$ transverse motion as well as between the transverse and the longitudinal motion, the particles' spatial coordinates and divergences can be described separately for each plane with a two-dimensional transport matrix (similar for y and z):

$$\begin{bmatrix} x \\ x' \end{bmatrix}_{s_1} = \begin{bmatrix} M_{1,1} & M_{1,2} \\ M_{2,1} & M_{2,2} \end{bmatrix} \cdot \begin{bmatrix} x \\ x' \end{bmatrix}_{s_0} . \tag{2.20}$$

If the optical functions at the start and end positions are know (and as well the phase advance between these two points), the transport matrix can be expressed in terms of these parameters which is called the Twiss representation of the transfer matrix or in short the Twiss matrix ([21] p. 170).

$$M = \begin{bmatrix} \frac{\beta_1}{\beta_0}(\cos\Delta\psi + \alpha_0 \sin\Delta\psi) & \beta_1\beta_0 \sin\Delta\psi \\ \frac{\alpha_0 - \alpha_1}{\sqrt{\beta_1\beta_0}} \cos\Delta\psi - \frac{1+\alpha_1\alpha_0}{\sqrt{\beta_1\beta_0}} \sin\Delta\psi) & \frac{\beta_0}{\beta_1}(\cos\Delta\psi + \alpha_0 \sin\Delta\psi) \end{bmatrix}, \tag{2.21}$$

where $\alpha_0, \alpha_1, \beta_0$ and β_1 are the Twiss parameters at the beginning and at the end points, respectively, $\Delta\psi$ is phase advance of the betatron function between start and end points.

For a drift space, the two-dimensional transport matrix is defined as:

$$M_d = \begin{bmatrix} 1 & l_d \\ 0 & 1 \end{bmatrix}, \tag{2.22}$$

where l_d is the drift length.
For an ideal focusing quadrupole magnet (hard-edge model without the fringe fields) the transport matrix has the form [21]:

$$M_{qf} = \begin{bmatrix} \cos\varphi & \frac{1}{\sqrt{k}\sin\varphi} \\ -\sqrt{k}\sin\varphi & \cos\varphi \end{bmatrix}, \tag{2.23}$$

and for an ideal defocusing quadrupole magnet:

$$M_{qdf} = \begin{bmatrix} \cosh\varphi & \frac{1}{\sqrt{k}\sinh\varphi} \\ \sqrt{k}\sinh\varphi & \cosh\varphi \end{bmatrix}, \tag{2.24}$$

where k is the quadrupole strength $k = eg/p, e$ is the particle charge, g is the quadrupole gradient, p is the particle momentum and $\varphi = l_{eff}\sqrt{k}$. l_{eff} is the effective length of the quadrupole magnet. If the thin-lens model of the quadrupole is assumed, the transfer matrix can be given by:

$$\begin{bmatrix} x \\ x' \end{bmatrix}_{s_2} = \begin{bmatrix} 1 & l_d \\ 0 & 1 \end{bmatrix} \cdot \begin{bmatrix} 1 & 0 \\ -kl_q & 1 \end{bmatrix} \begin{bmatrix} x \\ x' \end{bmatrix}_{s_1} = \begin{bmatrix} 1 - kl_q l_d & l_d \\ -kl_q & 1 \end{bmatrix} \begin{bmatrix} x \\ x' \end{bmatrix}_{s_1}. \tag{2.25}$$

Besides the particles' transverse coordinates and divergences, the transport matrix for dipole magnets should include the relative momentum deviation $\delta p = \Delta p/p_0$ from the design reference particle momentum p_0:

$$\begin{bmatrix} x \\ x' \\ \delta p \end{bmatrix}_{s_1} = \begin{bmatrix} M_{1,1} & M_{1,2} & M_{1,3} \\ M_{2,1} & M_{2,2} & M_{2,3} \\ M_{3,1} & M_{3,2} & M_{3,3} \end{bmatrix} \cdot \begin{bmatrix} x \\ x' \\ \delta p \end{bmatrix}_{s_0}. \tag{2.26}$$

In the deflecting plane of a pure sector magnet with bending angle θ, bending radius ρ and constant bending field along the beam trajectory, the transport matrix has

the following form (see [21]):

$$M_x = \begin{bmatrix} \cos\theta & \rho\sin\theta & \rho(1-\cos\theta) \\ -\frac{1}{\rho}\sin\theta & \cos\theta & \sin\theta \\ 0 & 0 & 1 \end{bmatrix}. \tag{2.27}$$

The direction of bending is negative with respect to the x axis. For the opposite direction of bending, coinciding with the x axis, this matrix can be calculated from Eq. 2.27 by changing the sign of θ and ρ :

$$M'_x = \begin{bmatrix} \cos\theta & \rho\sin\theta & -\rho(1-\cos\theta) \\ -\frac{1}{\rho}\sin\theta & \cos\theta & -\sin\theta \\ 0 & 0 & 1 \end{bmatrix}. \tag{2.28}$$

In the nondeflecting plane, the sector magnet behaves like a drift space with length $l = \rho \cdot \theta$:

$$M_y = \begin{bmatrix} 1 & l & 0 \\ 0 & 1 & 0 \\ 0 & 0 & 1 \end{bmatrix}. \tag{2.29}$$

In the case of a sector magnet and a drift space with length L downstream the magnet, the resulting transport matrix in the deflecting plane can be calculated as a product of the magnet matrix and the drift matrix:

$$M = \begin{bmatrix} 1 & L & 0 \\ 0 & 1 & 0 \\ 0 & 0 & 1 \end{bmatrix} \cdot \begin{bmatrix} \cos\theta & \rho\sin\theta & \rho(1-\cos\theta) \\ -\frac{1}{\rho}\sin\theta & \cos\theta & \sin\theta \\ 0 & 0 & 1 \end{bmatrix}. \tag{2.30}$$

Knowing the initial particle coordinates x_0, divergences x'_0 and relative momentum δp one can calculate the particle transverse coordinates x downstream the dipole and the drift space:

$$x = x_0(\cos\theta - \frac{L}{\rho}\sin\theta) + x'_0(L\cos\theta + \rho\sin\theta) + \delta p \cdot D, \tag{2.31}$$

where,

$$D = L\sin\theta + \rho(1-\cos\theta), \tag{2.32}$$

is the dispersion downstream the drift space. Eq. 2.31 shows that a particle transverse coordinate on a screen has a linear dependence on its momentum. This gives the possibility to perform measurements of the beam momentum and momentum distribution by measuring the beam transverse projection on a screen downstream a dipole magnet.

2.2 Beam dynamics with space charge

The particle motion described by the Lorentz force in Eq. 2.1 does not take beam current into account. However, in reality the beam current is a source of self-induced electromagnetic fields and affects the beam dynamics. These self-fields are categorized into space charge fields [23] and wakefields [24]. Space charge forces are generated by a continuum of charge distribution over a region of space (volume or area). For the purpose of understanding, the space charge force in an electron beam can be considered as an external force F_{sc}. It can be categorized into linear and non-linear terms based on the displacement from the beam axis. The linear space charge term typically causes the beam to defocus and increases its size, while the non-linear space charge term distorts the phase-space distribution and increases the rms beam emittance.

To calculate the space charge forces in a beam moving with velocity $v = \beta c$ along the z direction, one can consider a perfectly conducting smooth round pipe. The transverse fields produced by an ultra-relativistic charge inside the pipe are identical to those in free space due to symmetry and relativistic effects. Therefore, the total force acting on a charge inside the beam with uniform radial distribution and a longitudinal linear density $\lambda(z)$ is given by:

$$F_{sc} = e(E_r - \beta c B_\Phi) = q(1-\beta^2)E_r = \frac{q}{\gamma^2}\frac{\lambda(z)}{2\pi\epsilon_0}\frac{r}{a^2}. \tag{2.33}$$

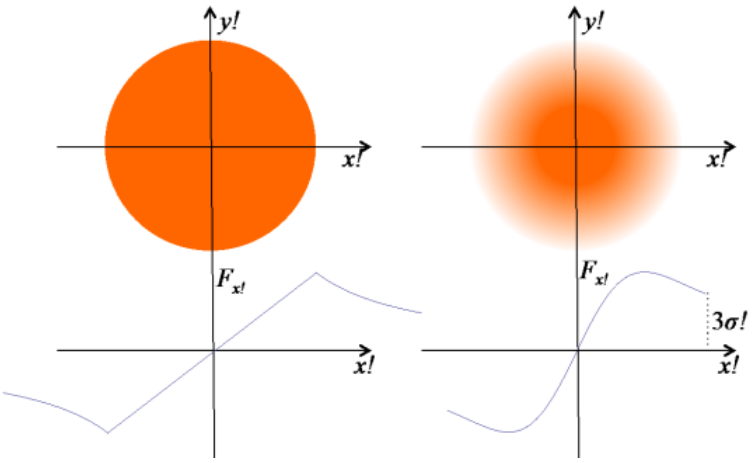

Figure 2.3: Transverse defocusing forces produced by space charge for (left) uniform (right) Gaussian distribution. Taken from [23].

If the electron bunch generated has a transverse and temporal Gaussian distribution, one can consider the following distribution:

$$\rho(r,z) = \frac{e}{(2\pi)^{3/2}\sigma_z\sigma_r^2} e^{\frac{-z^2}{2\sigma_z^2} - \frac{r^2}{2\sigma_r^2}}. \tag{2.34}$$

In this case, the expression for the space charge is modified to:

$$F_{sc} = \frac{e}{(2\pi)^{3/2}\epsilon_0\gamma^2}\frac{Q}{\sigma_z} e^{-\frac{z^2}{2\sigma_z^2}} \left(\frac{1 - e^{\frac{-r^2}{2\sigma_r^2}}}{r}\right). \tag{2.35}$$

Eq. 2.35 shows that the radially defocusing space charge force F_{sc} of such a charge distribution is non-linear in r, while also changing along the longitudinal position z. The amplitude of the space charge forces is suppressed for increasing beam energy with $\propto \gamma^{-2}$. Therefore, space charge effects degrade the beam stronger at lower energies and are of less concern at high energies. Figure 2.3 shows comparison between transverse defocusing fields.

Space charge effects on beam

Direct space charge effects in a linear accelerator can cause significant longitudinal-transverse correlations of the bunch parameters. This can lead to a mismatch with

the focusing and accelerating devices, resulting in a projected emittance growth and energy spread increase. The transverse dynamics of a beam characterized by an rms envelope σ can be described under the paraxial ray approximation, i.e., $p_x <<< p_z$, by the rms envelope equation for an axisymmetric beam [23]

$$\sigma'' + \frac{\gamma'}{\gamma}\sigma'' + k_{ext}^2\sigma = \frac{K_{sc}}{\gamma^3\sigma} + \frac{\epsilon_{n,th}^2}{\gamma^2\sigma^3}. \tag{2.36}$$

There are three terms on the left hand side of Eq. 2.36. The first term corresponds to the change in the slope of the beam envelope, the second term causes damping of the envelope oscillation due to acceleration where $\gamma' = eE_{acc}/mc^2$, E_{acc} being the accelerating field, and the third term corresponds to the linear external focusing forces, e.g., by a solenoid. The right hand side of the Eq. 2.36 is a combination of two terms. The first one corresponds to the space charge defocusing effect where $K_{sc} = \hat{I}/2I_A$ is the beam perveance, $\hat{I}$ being the peak current and $I_A \approx 17$ kA being the Alfven current. The second term describes the internal pressure due to emittance where $\epsilon_{n,th} = (m_0c)^{-1}\sqrt{\langle x^2\rangle\langle p_x^2\rangle}$ is the transverse normalized thermal RMS emittance at the source.
When the space charge term is dominant, the beam particle trajectories do not cross each other, and beam transport requires careful tuning of focusing elements. This causes correlated emittance growth which can be made reversible only if proper beam matching is done. When the ratio of space charge and emittance terms is nearly unity, the beam is emittance dominated and therefore, the space charge effects can be neglected. The beam energy at which the beam transits from the space charge dominated regime to the emittance dominated is called transition energy [23],

$$\gamma_{tr} = \frac{\hat{I}}{2I_A}\frac{\sigma^2}{\epsilon_n^2}. \tag{2.37}$$

For linac-driven free electron lasers where bunch compressors are used to increase the peak current in the beamline, the transitional energy is changed.

2.3 Accelerating structures for Linacs

An RF electric field gives energy to the beam in every RF accelerator [22]. The beam and the field have to be in sync for the energy transfer to last. Pulsed power tubes like klystrons supply the RF power. It often goes into the linac structure as TE_{10} mode in a rectangular waveguide which joins the cylindrical TM_{01} mode cavity perpendicularly. In order to have acceleration, the phase velocity $v_\phi = w\lambda_z/2\pi$ of the wave must match the velocity of the particles. For a relativistic beam, a structure is loaded with iris-shaped sheets at a constant separation in the waveguide, known as disc-loaded structures. The RF power can be coupled into the cavity either by loop coupling or slot coupling. The total acceleration of the whole structure can be calculated by multiplying the acceleration of one cell by the total number of cells. Linac structures can be operated using both travelling wave and standing wave, depending whether the structure is closed by a reflection-free boundary or not. The irises form a periodic structure within the cavity, allowing loss-free propagation only if the wavelength is an integer multiple of the iris separation d, namely, $\lambda_z = pd$, where $p = 1, 2, 3, ...$ These fixed wave configurations are also called modes. In principle there are arbitrarily many modes, but only the following three are usually used for acceleration.

$$k_z d = \begin{cases} \pi & (\pi\text{mode i.e. } \lambda_z = 2d)\text{if p} = 2 \\ \frac{2\pi}{3} & (2\pi/3\text{mode i.e. } \lambda_z = 3d)\text{if p} = 3 \\ \frac{\pi}{2} & (\pi/2\text{mode i.e. } \lambda_z = 4d)\text{if p} = 4 \end{cases}$$

Particle acceleration in an RF cavity

Energy can be transferred to a particle in a resonant RF cavity. The amplitude of the electric field on the axis of a standing wave structure at a specific time varies with the longitudinal coordinate along the structure. This field oscillates in time according to the harmonic law:

$$E_z(z,t) = E_0(z)\cos(\omega t + \Phi), \tag{2.38}$$

where $E_z(z,t)$ is the longitudinal electric field on the axis of the structure, $E_0(z)$ is the electric field amplitude as a function of the longitudinal coordinate, $\omega = 2\pi f$, where f is the RF frequency, t is the time and Φ is the initial RF phase of the structure when a particle enters it. Here it is assumed that the structure consists of several identical cells, so $E_0(z)$ is a periodic function. Therefore, to have the most efficient acceleration, the time of flight of the particle through one cell should be equal to the half period of the RF. The single cut disk cell of a PITZ booster accelerating cavity is shown in Fig. 2.4. The structure consists of 14 cells, operating in $2\pi/3$ mode. Fig. 2.4 (right) shows the electric field distribution along the whole structure.

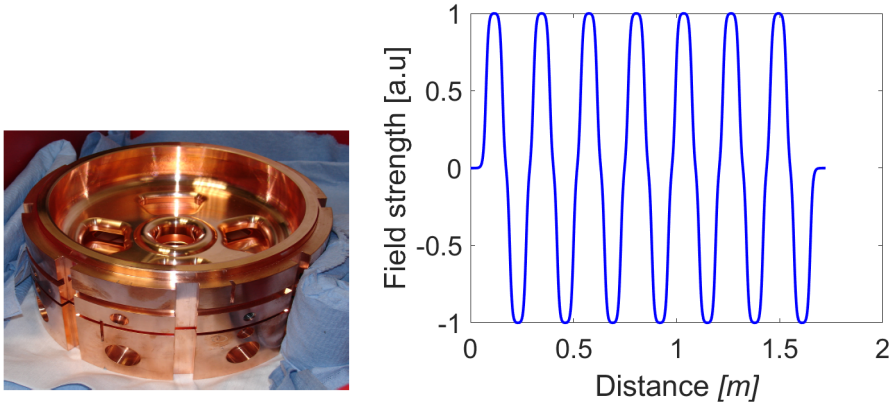

Figure 2.4: (left)Single cell structure (right) Electric field variation along booster.

Another important fact is the RF phase focusing in the design of all accelerators. The energy transferred to the particles depends on the amplitude as well as nominal phase, lets say, Φ_0. In case of multiple cells, a slight deviation from the nominal accelerating voltage can result in a phase shift relative to the RF voltage and loss of synchronization of particles. The trick is not to use $\Phi_0 = \pi/2$, but slightly less value. In this way if a particle has gained too much energy in the preceding stage and arrives earlier, it sees an average RF phase $\Phi = \Phi_0 - \Delta\Phi$ and is accelerated below the ideal voltage. Therefore it gets less energy and returns to the nominal voltage. The opposite happens to the particles whose energy is low. Thus all particles oscillate about the nominal phase Φ_0.

2.4 RF photo injectors

Since now we have the knowledge of beam dynamics as well as the RF systems, we can utilize it to introduce the RF photo injectors. A photo injector is a source of electrons for short wavelength light sources like high gain free electron lasers or energy recovery linacs. It is used to generate and accelerate electrons to relativistic energies. The design and development of a photo injector depends upon the application.

A photo injector consists of an electron gun which may use DC (direct current) or RF (radio frequency) fields to accelerate the electrons. In case of a DC source, a ceramic insulation is required between a cathode and an anode to avoid corona discharge. Therefore, the electrons can be accelerated within the gun upto 350 keV. Nowadays, RF source based electron guns can have a cavity that is either normal conducting (NC) made of copper or super conducting (SRF) made of niobium. Both of them can sustain high electric field gradients and therefore, accelerate the electron beam to a few MeVs.

Electrons can be emitted from the cathode with the desired time structure and frequency. They can be released either by a thermionic emission where the cathode is heated to emit electrons or by photoemission where a drive laser gates the emission of electrons from the cathode. A photocathode can either be a metal e.g. copper, magnesium, e.t.c. or a semiconductor e.g., cesiated antimonide or telluride. Since the semiconductor photocathodes have high quantum efficiency (ratio of number of electrons to incident number of photons) with low work function (the minimum quantity of energy required to remove an electron from the surface of the cathode), they are the preferred choice in a photoinjector. Generally, the demand of a light source facility is to maximize the single bunch brightness, which means to concentrate a maximum of charge in the smallest possible 6D phase space volume. Assuming there is no significant coupling between the transverse phase spaces, and the transverse and the longitudinal phase spaces, the beam brightness $\mathcal{B}$ is expressed as:

$$\mathcal{B} = \frac{Q}{\epsilon_{n,x}\epsilon_{n,y}\epsilon_{n,z}}, \tag{2.39}$$

where Q is the charge, and $\epsilon_{n,\mu} \in \{x, y, z\}$ are the normalized emittances.

There are many factors that contribute to the total transverse emittance ϵ_{tot} of the

beam and thus deteriorate the quality of the beam. For example, when the laser shines on the photocathode, the electron energies are in the eV range. At this point, the transverse beam emittance is given by the thermal emittance ϵ_{th}, which is defined by the cathode properties, the laser wavelength and the beam spot size on the photocathode. As the electron cloud is extracted, it experiences repulsive space charge forces that degrade the phase space, and thus the beam goes into space charge dominated regime with emittance ϵ_{SC}. Then, there is also RF-induced emittance growth ϵ_{RF} specially for long pulses. Thus, the total emittance can be expressed by:

$$\epsilon_{tot} = \sqrt{\epsilon_{th}^2 + \epsilon_{SC}^2 + \epsilon_{RF}^2}. \tag{2.40}$$

One of the advantage of RF based guns is that the cathode is present at the high gradient region so the beam exits already at a few MeVs, reducing the effect of space charge forces. Inspite of that, if the charge is high, the beam stays in the space charge dominated regime at the exit of the gun that not only defocuses the beam but also causes different time slices within the beam to expand at different rates. Typically, a solenoid is present around the RF gun to suppress the space charge induced emittance growth. One has to then tune the solenoid current to overlap the slices in the phase space to obtain the minimum possible projected emittance (transverse emittance of the whole particle bunch). Figure 2.5 shows the profile of a 1.6 cell L band RF cavity along with RF generated $\vec{E}$ field and solenoid generated $\vec{B}$ field. Figure 2.6 shows an electron bunch consisting of 5 slices that expand radially at different rates. The emittance of the individual slices contribute to the projected emittance.

The emittance growth compensation using solenoid only works for linear defocusing forces. For the non-linear defocusing space charge forces, the regime of laser shaping techniques has been explored. The laser can be adjusted to have a transverse Gaussian or a truncated transverse Gaussian shape as well as a temporal Gaussian or a flat top shape [20]. Also, of particular importance is the central slice emittance (transverse emittance of a short, longitudinal disc of the bunch) as it contributes the most to the lasing process in free electron lasers [20].

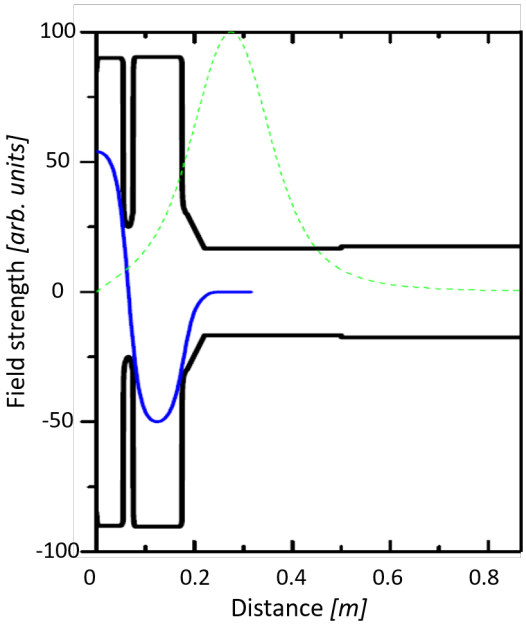

Figure 2.5: Field distribution along a 1.6 cell normal conducting photo injector. The blue solid line shows the electric field of the gun and the green dashed line shows the magnetic field distribution of the solenoid [17].

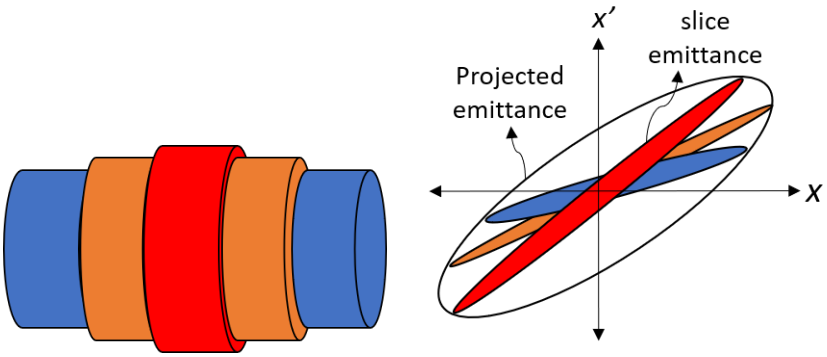

Figure 2.6: (left) Bunch with 5 slices expanding radially at different rates. (right) Slice emittance comes from phase space ellipses of individual slices. Together they contribute to the projected emittance.

Free electron lasers

The application of high brightness photo injectors for Free Electron Lasers (FELs) is crucial in the accelerator community, owing to their utilization to investigate matter at their length and time scales [1]. In the last years, the main focus has been on maximizing the electron beam brightness, i.e. the number of charged particles per unit volume in the six-dimensional phase space of the beam. Such high brightness electron beams serve for the production of high intensity, high brilliance synchrotron and FEL light.

Basically, in an FEL, the magnetic field of the undulator magnet causes the electrons to oscillate transversely and at period λ_u. These oscillations induce micro-bunching on a scale of λ_r, which causes electrons within the micro-bunch to radiate coherently at the resonant wavelength. The expression for λ_r is give by [6]:

$$\lambda_r = \frac{\lambda_u}{2\gamma^2}\left(1 + \frac{K^2}{2} + \gamma^2\phi^2\right), \tag{2.41}$$

where λ_u is the period length of the undulator magnet, γ is the relativistic Lorentz factor, ϕ the observation angle w.r.t. the beam axis and K is the undulator parameter:

$$K = \frac{eB\lambda_u}{2\pi m_e c}, \tag{2.42}$$

where B is the peak magnetic field, m_e and e are the mass and the charge of the electron, and c is the speed of light. Figure 2.7 shows the schematics of an undualtor with an electron beam passing through.

The FEL power gain length L_G is the length needed for exponential growth rate in the radiation power. In the one-dimensional (1D) model which assumes that the electron beam has a uniform transverse spatial distribution with zero emittance and energy spread, the power gain length can be expressed as follows [6]:

$$L_{G0} = \frac{1}{4\pi\sqrt{3}} \cdot \frac{\lambda_u}{\rho_{FEL}}, \tag{2.43}$$

where ρ_{FEL} is the FEL or Pierce parameter:

$$\rho_{FEL} \propto \frac{I^{1/3}}{\gamma \cdot \sigma_t^{2/3}}, \tag{2.44}$$

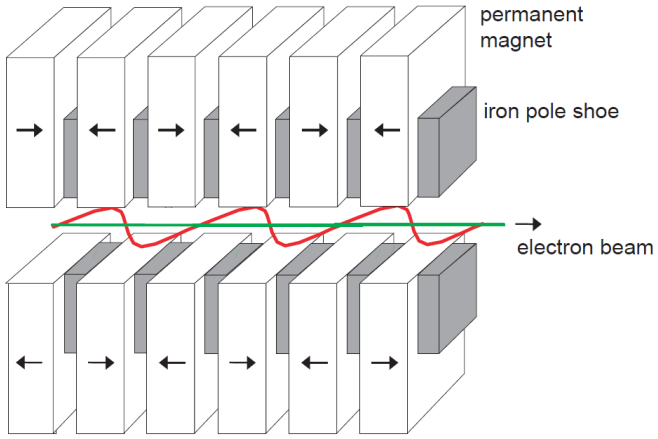

Figure 2.7: Schematic view of a planar hybrid undulator magnet with alternating polarity of the magnetic field and of the sine-like trajectory of the electrons [6].

where I is the peak current of the electron beam, and σ_t its transverse beam size:

$$\sigma_t = \sqrt{\sigma_x \sigma_y}. \tag{2.45}$$

In the 1D approximation, the FEL saturation radiation power is about ρ_{FEL} times the eletron beam power. The relative bandwidth at saturation is approx. ρ_{FEL}.

$$P_{sat} \approx \rho_{FEL} \cdot P_{beam}. \tag{2.46}$$

Taking into account that the electron current is inversely proportional to the longitudinal beam size (i.e. $I \approx \sigma_l^{-1}$), a crucial parameter for the FEL process is the electron beam density in the 3-dimensional space. We can define the total size of the electron beam σ_{3D} as:

$$\sigma_{3D} = (\sigma_l \sigma_x \sigma_y)^{\frac{1}{3}}. \tag{2.47}$$

From the above relations, one can conclude that $\rho_{FEL} \propto \sigma_{3D}^{-1}$, i.e., smaller the beam size, shorter the relative bandwidth and better the FEL performance [25]. Hence, to have high FEL gain, the beam should have small transverse and longitudinal sizes, small divergence and energy spread and high peak current. In order to achieve this, it is important to do proper beam diagnostics to be able to tune and characterize the beam.

Chapter 3

Photoinjector Test Facility at DESY in Zeuthen

The Photo Injector Test facility at DESY in Zeuthen (PITZ) was built in 2000-2002 [26] to develop, condition, and characterize the high brightness electron sources for high gain free-electron lasers (FELs), such as Free electron LASer in Hamburg (FLASH) and the European XFEL in Hamburg [13]. The domain of PITZ research also includes photo cathode laser shaping to reduce emittance [27,28], slice emittance characterization [20], slice energy spread measurements, [18] and photo cathode developments e.g. green cathodes [29]. Apart from the basic research, there have also been research activities on applications of high brightness injectors, such as the investigation of plasma wakefield acceleration [30,31] and tests of electron diffraction experiments [32]. Recently, PITZ successfully performed proof-of-principle studies of accelerator-based terahertz radiation [33,34] and has now embarked to carry out research in state-of-the-art cancer radiation therapy with ultra-high dose rates [15]. Therefore, PITZ has a flexible parameter space to support a wide range of research activities. This chapter will give an overview of the major components of the facility and its diagnostic devices.

Figure 3.1 shows the schematics of the PITZ beamline. The main components of the PITZ setup are a photocathode laser system, an RF photo-electron gun and a post-accelerating cavity, the Cut Disk Structure (CDS) – also called booster cavity. There are also many diagnostic devices installed in the beamline for detailed electron beam characterization. Faraday cups and Integrated Current Transformers (ICTs)

are used for bunch charge measurements and scintillating screens are used for beam transverse position and transverse distribution measurements. The transverse phase space is measured using a slit scan technique at three different locations downstream the booster cavity. A phase space tomography module is also installed that can simultaneously restore the horizontal and vertical transverse planes in contrast to the slit scan technique. A low-energy spectrometer (Low Energy Dispersive Arm – LEDA) and two high-energy spectrometers (High Energy Dispersive Arm – HEDA1 and HEDA2) are used for momentum characterization of the electron bunches after the gun and booster, respectively. The Transverse Deflecting Structure (TDS) enables bunch length measurement as well as slice emittance measurement of the electron bunches and is an adequate tool for high-resolution longitudinal phase space measurements downstream the booster. Phase space tomography is also performed to reconstruct the longitudinal phase space after the gun with the existing set up. Steering magnets together with Beam Position Monitors (BPMs) allow for realizing the proper beam trajectory along the entire beamline. Quadrupole magnets are used for controlled beam transport and enable beam focusing for measurements.
PITZ beamline was extended to perform proof-of-principle Tera Hertz (THz) experiments. The beamline now extends over two tunnels that can be operated independently. An undulator along with related diagnostics (pyrodetectors, coherent transition radiation detection screen, e.t.c.) and a beam dump is installed in Tunnel 2 to generate and measure THz radiation. Furthermore, to improve the pulse energy of the THz radiation, a bunch compressor is installed in Tunnel 1. Another recent upgrade is the radiation biology beamline. At the entrance of Tunnel 2, a switchyard magnet is installed to bend the beam and perform irradiation of biological samples.

3.1 Main components of PITZ beamline

The section will explain the main components that constitute the PITZ beamline.

3.1.1 Photocathode laser

Electron bunches are generated from the photocathode when laser light is incident on the cathode surface. A flexible laser setup is required at PITZ in order to

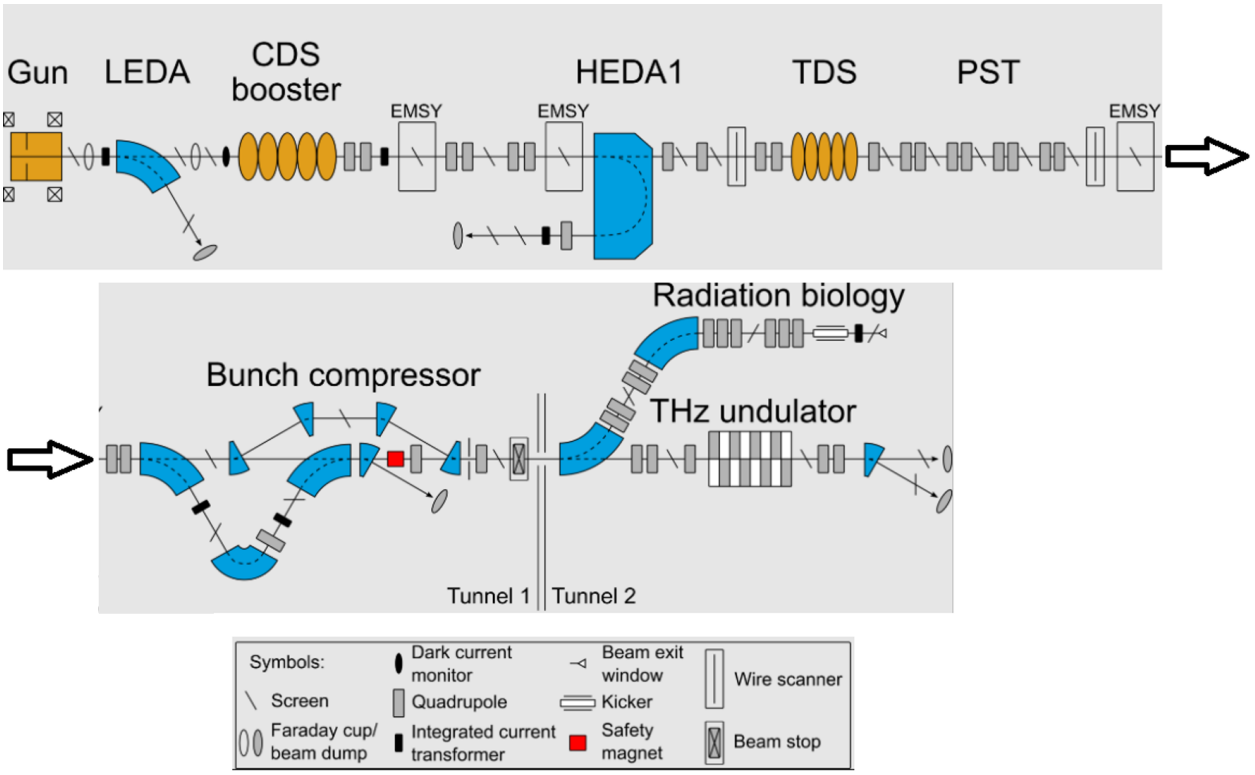

Figure 3.1: Layout of the PITZ facility. Electron bunches are generated in the RF gun by a photocathode laser and travel from left to right.

achieve the desirable laser pulse shape, pulse repetition rate, and power, required for the wide parameter range. The customized laser developed at the Max-Born-Institute (MBI) [35] was installed at PITZ in summer 2008 with the aim to achieve reduction in emittance [36] and achieve advanced pulse shaping. Because of the aging of its components, it has been replaced in 2023 with a new laser built at Hamburg. The PITZ facility also has another photocathode laser system based on a commercial 20W front-end laser (PHAROS) [37]. Both laser systems are located in the same room and can be swapped by moving in a mirror. The laser beamline is approximately 25 m-long starting from the laser room exit, going all the way through the shaft into the tunnel at the photocathode location. It is split into two parts; the first part realizes an imaging of the laser pulses from the laser system onto the Beam Shaping Aperture (BSA) with a proper magnification so that the BSA cuts out the central part of the magnified transverse distribution and the second

part of the laser transport system provides an imaging onto the photocathode with unit magnification. The transverse laser spot size on the cathode can be varied by choosing BSAs with different diameters. A laser trolley is placed next to the photocathode area for laser pulse diagnostics. A UV camera is placed to measure the laser transverse profile and a Ultra Violet (UV) energy meter is used to measure the laser pulse energy. Since the measurements for this thesis were taken with the MBI laser, it will be explained in a bit more detail in the following subsection.

MBI laser

The MBI laser [35] can generate the desired trains of longitudinally shaped picosecond UV pulses. It consists of an infrared laser oscillator with a repetition rate of 54 MHz and a Gaussian profile of 0.7 ps FWHM. A pockels cell is used to downsample it to 1 MHz to synchronize it to the RF master oscillator of the linear accelerator. This is followed by a pulse shaper which consists of 13 birefringent crystals. Each of the crystals splits the incoming laser pulse into two pulses, which are slightly shifted temporally due to the birefringence. This setup allows to create laser pulses with a flattop distribution with FWHM pulse length up to 24 ps. For short pulses, for example, 1.5 ps, it can be bypassed. After this stage, the laser pulse power is increased in two amplifier stages. A wavelength converter then converts the infrared laser pulses of the laser to the ultraviolet (fourth harmonics) i.e. the laser pulses are converted from a wavelength of 1030 nm to 515 nm in a LBO crystal and then down to 257.5 nm in a BBO crystal. The second non-linear crystal is succeeded by a half wave plate with a birefringent crystal, which separates the polarizations spatially, which is used as an attenuator. The MBI laser is also equipped with an optical sampling system (OSS). OSS cross-correlates the short Infra Red (IR) laser pulses from the oscillator with the shaped UV pulses, allowing measurements of the temporal laser profile. Figure 3.2 gives an overview of different stages of amplifier [38].
Additionally, MBI can also produce modulated laser pulses by special tuning of the Lyot filter in the regenerative amplifier section. The temporal intensity profile of the generated infrared (IR) pulses can be modeled as [39]:

$$I_{IR}(t) = G(t, \sigma)\,(1 + \sin(2\pi f t))\,, \tag{3.1}$$

where I_{IR} is the IR pulse intensity at time t, f is the beating frequency, $G(t, \sigma)$ is a Gaussian envelope with RMS duration σ. The intensity profile after conversion into UV is $I_{UV}(t) \propto I_{IR}^4(t)$.

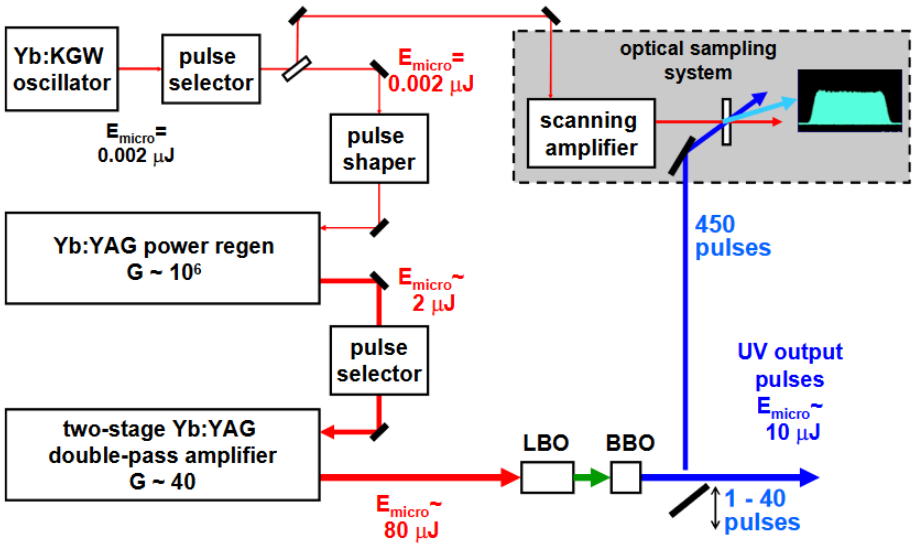

Figure 3.2: Overview of the MBI laser system. The laser is synchronized to produce electron bunches. The pulses are shaped and converted to UV before sending to the photocathode [38].

3.1.2 Electron source

A normal conducting 1.6 cell standing-wave gun cavity operating at 1.3 GHz (L-band) is used to accelerate electron bunches up to 6.5 MeV/c at PITZ [40]. A high Quantum Efficiency (QE) Cs_2Te semiconductor cathode is used to generate a high bunch charge at MHz repetition rate after illumination with a UV laser pulse. Electrons bunches are created as a result of the photoemission process. The gun is fed by a 10 MW klystron and can operate at a 10 Hz repetition rate with a 650 µs RF pulse length. Within each RF pulse, a peak RF power of about 6.5 MW is supplied to the cavity, achieving an electric field strength of approximately 60 MV/m at the photocathode. The cavity is surrounded by two solenoid magnets; a main solenoid magnet located at the extraction side of the cavity is used to focus the beam and a bucking solenoid located behind the gun cavity is used to compensate the magnetic

field of the main solenoid on the cathode surface. A 3D model of the PITZ electron source is presented in Fig. 3.3.

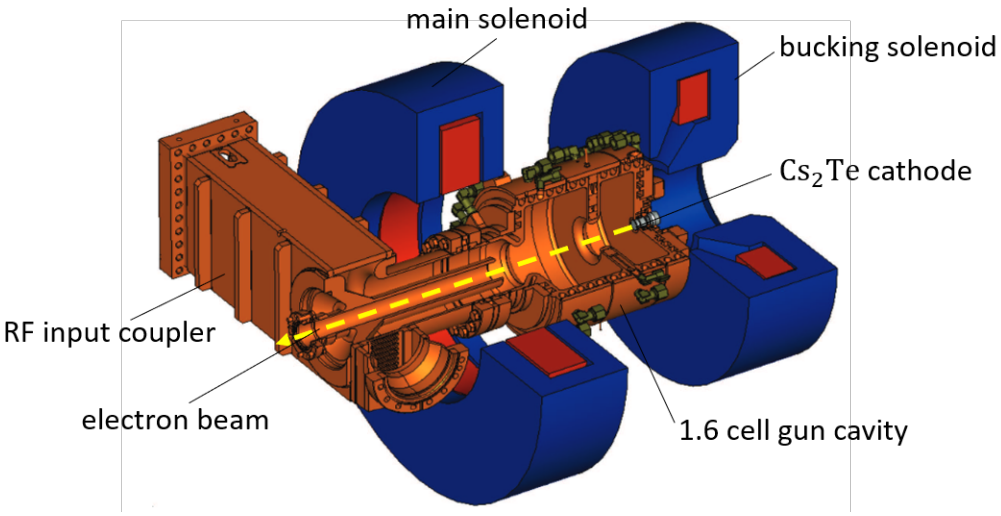

Figure 3.3: 3D model of PITZ RF gun. The electrons are emitted from the photocathode (grey), which is located at the back wall of the half cell. The RF power is coupled into the gun cavity through the doorknob-type coaxial coupler. The cavity is surrounded by the main and bucking solenoid magnets [41].

3.1.3 Accelerating structure

To further increase the electron beam energy, a normal-conducting cut-disk structure (CDS) is used at PITZ [42]. It was designed by the Institute for Nuclear Research in Troitsk, Russia and built by DESY, Hamburg. It is a standing wave cavity with 14 cells and operates at a frequency of 1.3 GHz. The RF pulses can have a maximum duration up to 900 µs with a 10 Hz repetition rate. It has a maximum gradient of 14 MeV/m and can accelerate the electron beam up to 25 MeV/c. A 3D model of the PITZ CDS booster cavity is presented in Fig. 3.4.

3.1.4 Applications of PITZ beam

Tunnel 2 contains beamline components that allow applications of the high brightness PITZ beam, generated and accelerated in tunnel 1. The overview of these beamlines is given in this subsection:

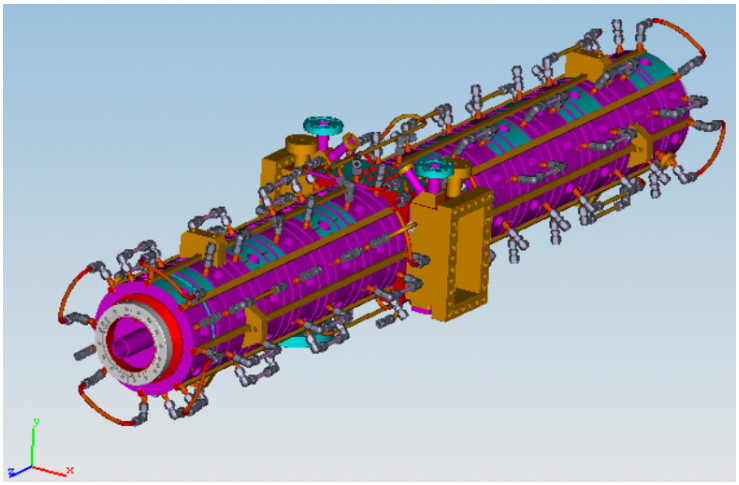

Figure 3.4: 3D model of booster at PITZ. The beam propagates from left to right [17].

Terahertz beamline

The European XFEL has planned to perform Terahertz (THz) pump–X-ray probe experiments at 4.5 MHz bunch repetition rate for users. Therefore, developments of a prototype for a high-power, tunable, accelerator-based THz source are also ongoing at PITZ [33, 34]. The THz beamline has been installed as an extension of the existing PITZ linac in the tunnel annex, see Figure 3.5. A planar LCLS-I undulator (module L143-112000-26 on-loan from SLAC) is used to generate the THz radiation from a Self-Amplified Spontaneous Emission (SASE) FEL. The undulator parameters require an electron beam energy around 17 MeV for the centre radiation wavelength of 100 µm. Untill now, a single pulse energy of up to 80 µJ has been demonstrated experimentally. High radiation power can be achieved by utilizing high charge (up to several nC) electron bunches from the PITZ RF photogun.

Radiation biology beamline

A research and development platform for electron radiation therapy and radiation biology is under development at PITZ (FLASHlab at PITZ) [15]. This platform is based on the unique beam parameters available at PITZ: ps scale electron bunches of up to 22 MeV energy with up to 5 nC bunch charge at MHz bunch repetition rate in bunch trains of up to 1 ms length repeating at 1 to 10 Hz. A startup beamline has

Figure 3.5: Undulator installed in the tunnel annex. The beam comes from left to right and after lasing, is sent to the beam dump.

been installed to allow dosimetry studies and irradiation experiments on chemical, biochemical and biological samples and cell cultures after a 60° dispersive arm. Figure 3.6 shows the current setup in the beamline. The measured dose and dose rates under different beam conditions are being carried out. In addition, a dedicated beamline has been designed for better control of the high brightness electron beams. This includes a dogleg to translate the beam and a 2D kicker system to scan the tiny beam focused by quadrupoles across the samples within less than 1 ms.

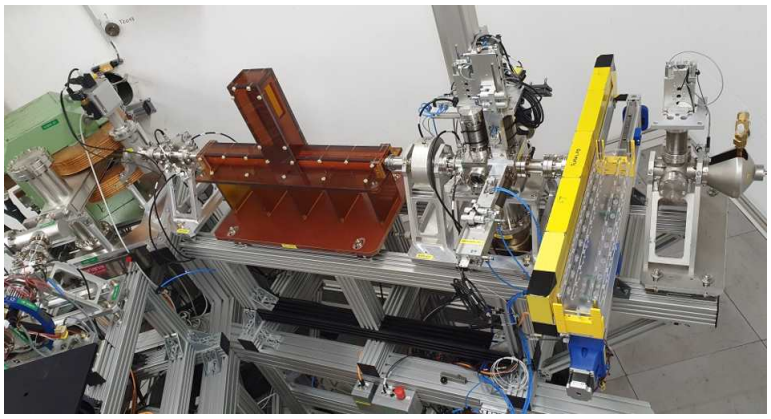

Figure 3.6: Current radiation biology setup at PITZ. The electron beam comes from left to right in the second tunnel and is bent 60° by a switchyard magnet towards samples.

3.2 Diagnostics at PITZ

The diagnostics used in a beamline depends upon the beam parameters and the beam properties to be measured. This section describes the main diagnostic equipment installed at PITZ.

3.2.1 Screen stations

A number of screen stations are present along the beamline for the measurement of the transverse beam position and distribution. The beam profile is translated to a light signal which is imaged onto a CCD camera chip. The screen material used at PITZ are inorganic cerium-doped ytterbium aluminium garnet (YAG) powder screens, and cerium-doped lutetium yttrium orthosilicate (LYSO) screens [43]. They are placed at 90° with respect to the direction of the beam propagation. Behind the screen, a mirror on a silicon substrate behind is used to reflect the light emitted from the screen to a CCD camera. The optical readout system for each screen includes at least the following components: the screen, the mirror, the lens, an aperture and the CCD camera. Usually two lenses for each screen can be used: the first, to see the whole screen, and the second, to have a zoomed image of the central part of the screen. Figure 3.7 shows a typical screen station setup.
The spatial resolution for the transverse beam size measurements will be limited by the alignment of the optical readout system, lens imperfections, aperture size, and pixel size of the CCD camera. In order to determine the magnification between the screen image and the camera image accurately, a mirror can be inserted into the optical beam path, to image a calibration grid with known size onto the camera chip. The calibration grid has the same distance to the imaging optics as the screen. In order to suppress the imaging distortions based on spherical aberration, an iris is installed before the lens. Increasing the size of the iris opening gives better signal but worse signal resolution. Another source of imaging imperfections is chromatic aberration. Since the light emitted from scintillators has a narrow spectrum, the setup's chromatic aberrations are negligible.
The cameras used at PITZ are a 12-bit CCD Prosilica GC 1350 from Allied Vision Technologies GmbH [44]. This type of camera has an array of 1360 × 1024 pixel,

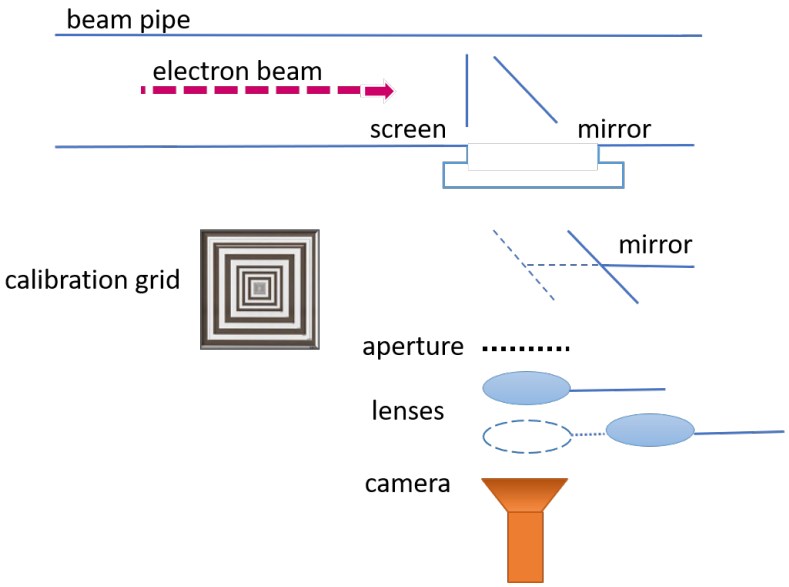

Figure 3.7: Schematic of the screen stations at PITZ. Adapted from [20].

each with a size of 4.65 µm × 4.65 µm. Additionally, the camera can be operated in a 2 × 2-binned mode, in which four pixels are merged to a single macro pixel, reducing the spatial resolution but improving the signal-to-noise ratio. The camera is triggered and read out at 10 Hz with a minimal exposure time of 10 µs, supporting the bunch pattern at PITZ.

3.2.2 Slit stations

The PITZ beamline is equipped with three slit-scan stations, namely Emittance Measurement SYstem (EMSY), to measure transverse phase space [16, 17]. They were designed in a collaboration of DESY and the Institute for Nuclear Research and Nuclear Energy in Sofia [45]. The slit stations are equipped with both vertical and horizontal actuators, which are moved precisely with stepper motors. Each actuator has a multi slit, two single slits (with 10 µm and 50 µm wide opening), and a screen installed, see Figure 3.8.

The purpose of the slit mask is to scatter the residual electrons from the beam so that they do not affect the beamlet propagation. The ideal thickness of the slit mask is a trade-off between the need to scatter electrons that do not pass through

the slit and the acceptance of the slit. Tungsten was chosen as the primary material for the slit due to its high atomic number, which implies a short radiation length of 0.35 cm, and its ability to withstand high thermal loads. Therefore, slit masks made of 1 mm-thick tungsten were used [16]. The 10 µm-slit allows to measure the projected emittance with a higher resolution which results in reduced space charge effects in the beamlets and thus a smaller systematic error. The 50 µm slit allows the transmission of more electrons, leading to a higher signal-to-noise ratio on the observation screen. This has relatively higher systematic errors in the beamlets. To maximise the number of electrons passing through the slit opening, the yaw and pitch angle of the whole station can also be tuned. Besides the slit masks, the slit stations are also equipped with scintillator screens and simultaneously serve as screen stations. A detailed description of the transverse phase space measurement via slit station will be be in chapter 4.

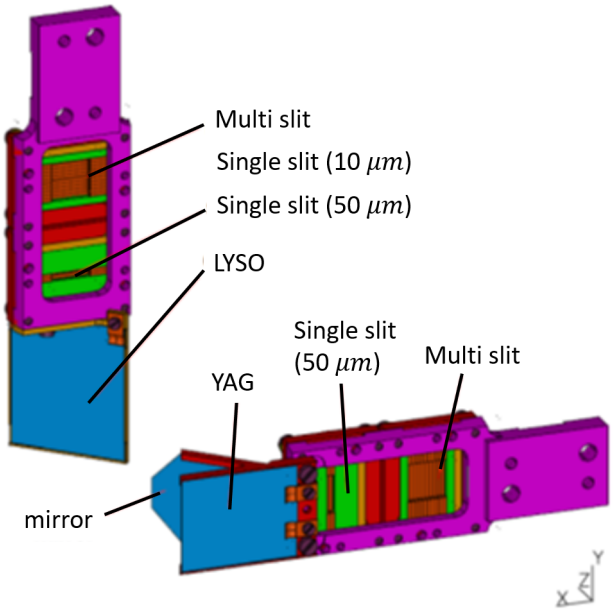

Figure 3.8: EMSY station consisting of a 10 µm and 50 µm wide slit, multi-slit, a YAG and a LYSO screen on horizontal and vertical actuator respectively [17].

3.2.3 Dipole stations

Currently, the PITZ beamline has six dipole stations that can be used for momentum measurements. In the tunnel 1, there is one to measure the beam momentum after the gun, namely, Low Energy Dispersive Arm (LEDA), and two for measuring the beam momentum after the booster, namely High Energy Dispersive Arm 1 and 2 (HEDA1 and HEDA2), respectively. There is also one installed after the bunch compressor and currently serves to bend the beam towards the beam dump when there is access in tunnel 2. In the second tunnel, there is a dipole magnet at the start of the beamline, known as switchyard, that can be used to bend the electron beam 60° towards the radiation biology beamline. The last dipole station is installed at the end of THz beamline to bend the beam away from the THz diagnostic station, towards the beam dump. This section will describe the LEDA and HEDA1 dipole stations only, since they were used in the thesis work. More detail will follow in chapter 5.

Low energy dispersive arm

The Low Energy Dispersive Arm (LEDA) located about 1.1 m downstream the electron gun consists of a 60° dipole magnet and a screen station, see Figure 3.9. It is used for the measurement of the beam momentum distribution with a mean momentum up to 7 MeV/c. The momentum distribution is measured as a vertical profile of the beam on the observation screen, namely Disp1.Scr1. The beam is focused vertically by the main solenoid for the best resolution by minimizing the effect of the transverse distribution. The schematics are shown in Figure 3.9.

High energy dispersive arm 1

The first High Energy Dispersive Arm (HEDA1) located about 8 m downstream the electron gun, consists of a 180° vertical dipole magnet, see Figure 3.10. It is designed for the measurement of the beam momentum up to 40 MeV/c [46]. The momentum distribution is measured as a vertical profile of the beam on the observation screen Disp2.Scr1. A reference screen, High1.Scr5, and quadrupole magnets upstream the dipole can be used to optimize the transverse beam size and orbit for the best momentum resolution [19, 47].

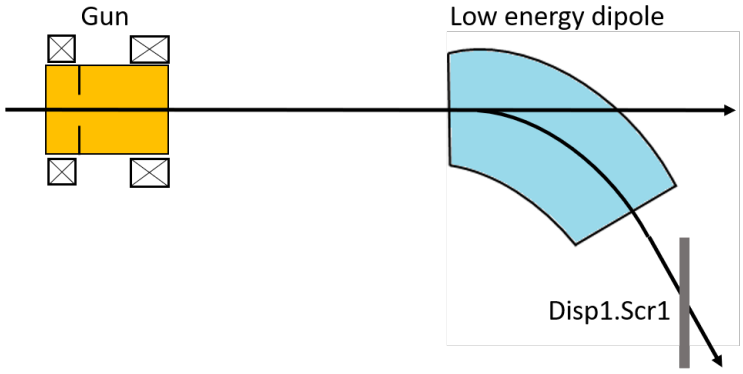

Figure 3.9: LEDA momentum measurement setup. The beam propagates from left to right. The main solenoid focuses the beam on Disp1.Scr1 where the momentum distribution is measured as a vertical profile of the beam.

3.2.4 Transverse deflecting structure

A transverse Deflecting Structure (TDS) deflects the particles of the beam transversely with respect to their design trajectories. It is widely used for the characterization of the electron bunch longitudinal profile, longitudinal phase space [48, 49] and even bunch transverse slice emittance [20]. The first iris-loaded RF deflecting structure was built at SLAC in the 1960's for particle separation and called LOLA for the first letters in the names of its inventors. TDS for PITZ was designed and manufactured by the Institute for Nuclear Research (INR, Troitsk, Russia) as a prototype of the TDS cavity for the European XFEL injector [50]. Operation principle of TDS is based on the fact that the particles get a time dependent perpendicular kick, which translates to a transverse offset on a downstream screen.

$$y = S \cdot z. \tag{3.2}$$

Here, y is the the transverse particle offset, z is the longitudinal particle coordinate w.r.t. the longitudinal beam centroid and S is the TDS shear parameter. More information on the working principle with detailed illustrations can be found in references [19, 20] and references therein. Figure 3.11 shows the shearing principle of TDS.

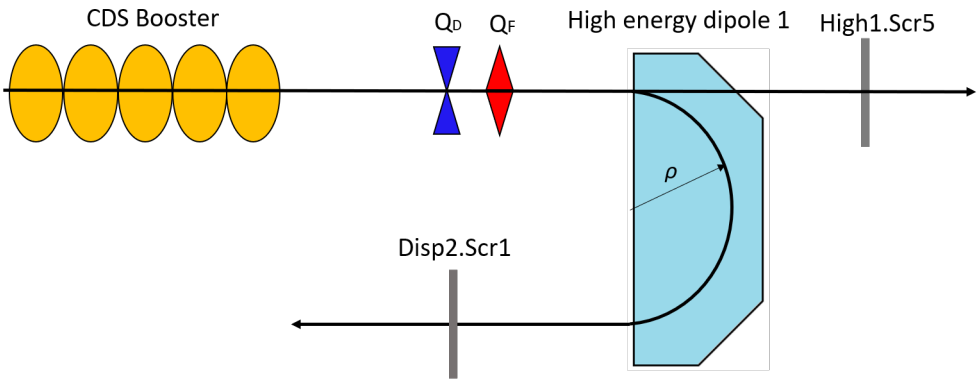

Figure 3.10: HEDA1 momentum measurement setup. The beam propagates from left to right. A set of quadrupoles is used to focus the beam on High1.Scr5 and the momentum distribution is measured as a vertical profile of the beam on Disp2.Scr1.

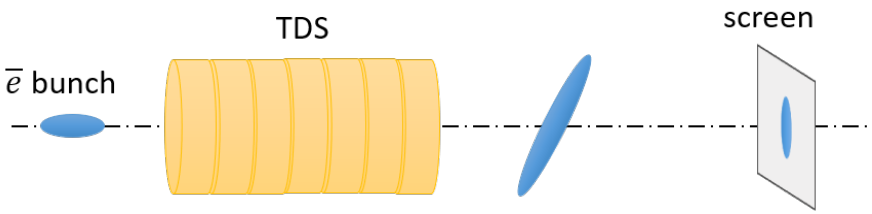

Figure 3.11: TDS kicks the particles depending on their longitudinal position. This appears as a transverse offset on a downstream screen [20].

3.2.5 Magnets

The PITZ beamline has many magnets to manipulate, control and focus/defocus the beam. This includes solenoid magnets, quadrupoles and steerers. Steerers were used both after the gun and the booster to guide the beam on the ideal trajectory. Quadrupoles were used to focus the beam to improve the measurements for the scope of this thesis work. Downstream the booster, there are several Danfysik quadrupole magnets [51]. They have an effective length of almost 40 mm and can reach a magnetic field gradient of up to 8.4 T/m. The longitudinal field profile of a quadrupole magnet is shown in Figure 3.12. Apart from them, there are also quadrupoles present around the gun cavity that are used to make the beam symmetric [52]. A more detailed description is present in chapter 4.

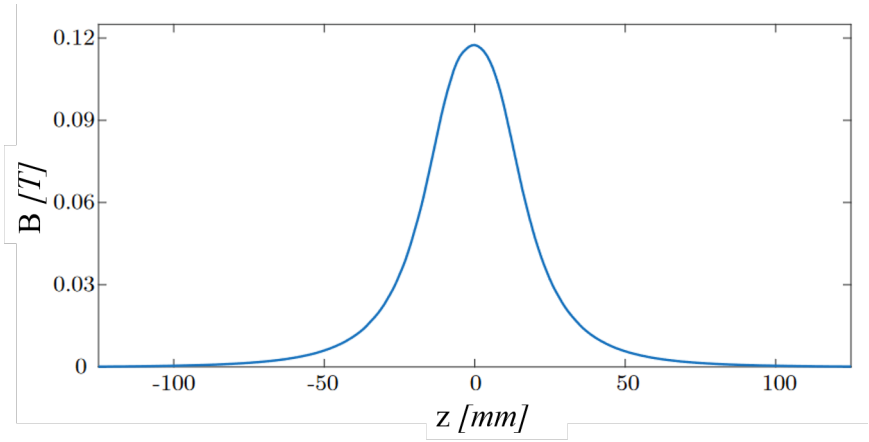

Figure 3.12: Longitudinal field map of one of the quadrupole magnets used at PITZ, measured at a radius of 16 mm [20].

3.3 Summary of e-beams at PITZ

Since PITZ is a test facility, it has a wide parameter space. The bunch charge varies from 5 pC to 5 nC and the beam energy can range from 17 MeV/c to 22 MeV/c. This depends upon the requirements of the measurement program, e.g., THz generation requires high charge, >2 nC and energy around 17 MeV/c [33]. For emittance measurement, the nominal beam energy after the gun and booster is kept around 6.3 MeV/c and 19.3 MeV/c, respectively. The bunch charge used is 250 pC since this is the working point of Eu-XFEL [40]. The typical beam size at the cathode is around 0.25 mm and the laser pulse length is kept around 6.6 ps FWHM, which was also kept for this thesis work. The emittance values for such a beam are generally less than 1 µm rad. Since the electron beam at PITZ has high beam charge and low beam energy, it is space charge dominated. This makes the beam transport complicated and requires special considerations in diagnostics. The imperfections in the beam symmetry and coupling between the transverse planes as well as transverse to longitudinal plane are caused by the solenoid and RF coupler kick. The aim of this thesis was to diagnose the space charge dominated beams in 4D transverse phase space and 2D longitudinal phase space using the existing setup by optimizing measurement programs and post-processing of data.

Chapter 4

4D transverse phase space characterization via virtual pepper pot

4.1 Introduction

The 2-dimensional Transverse Phase Space (TPS) characterization is done at PITZ using the single slit scan technique as already mentioned in the PITZ facility overview [17, 53]. There is considerable interest in the accelerator community in general, and at PITZ in particular, to understand and characterize the 4-Dimensional (4D) TPS, to remove the transverse plane coupling and minimize the emittance in order to optimize the performance of the photoinjector. The Virtual Pepper Pot (VPP) is a novel method that is recently established at PITZ for 4D TPS measurements after first preliminary studies discussed in [54]. Its detailed characterization and implementation at PITZ is one of the main topic of this thesis. Let us review the pepper pot technique in general [55, 56] and the slit scan technique with reference to the methodology adopted at PITZ [17, 40]. This will be followed by an overview of the VPP, its advantages as well as challenges.

Pepper pot

The pepper pot technique is well-known in accelerators for measuring the 4D transverse phase space of beam particles [55–57]. It can yield information about the beam profile and the angular divergence in a single measurement, with the help of a pepper pot plate and a downstream observation screen. The pepper pot plate

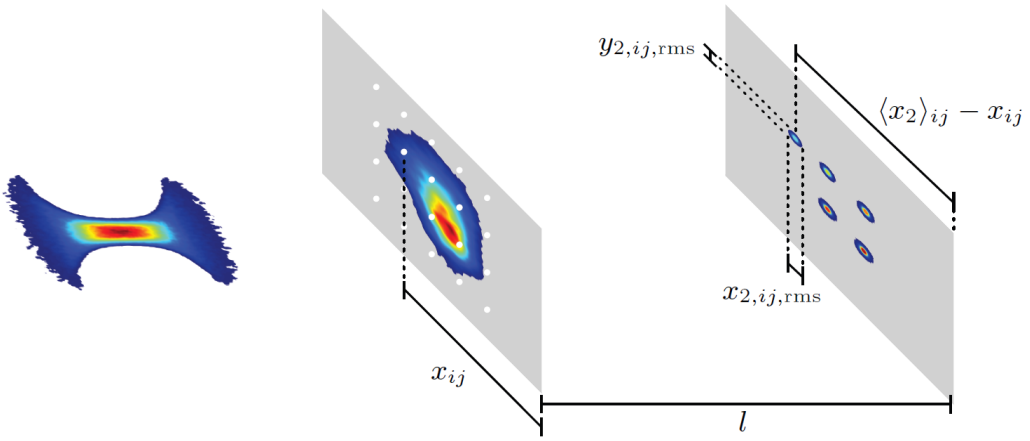

Figure 4.1: Schematics of a pepper pot measurement system. The pepper pot mask creates beamlets. Their x and y rms sizes and positions w.r.t the holes can be measured to reconstruct the 4D TPS and calculate the emittance [20].

contains a regular array of identical holes that allows only the beam incident on a hole to pass through and scatters the rest of the particles. The particles passing through the holes, appear as beamlets on the observation screen after propagating a sufficient distance l, see Figure 4.1. The total intensity of each beamlet as a function of the position of the defining hole provides a spatial profile of the beam, and can be measured on the observation screen. The size $x_{2,ij,rms}$ of the beamlet after a distance l is given by [20]

$$x_{2,ij,rms} = \sqrt{\sigma_{ij}'^2 \cdot l^2 + \sigma_{ij}^2}, \tag{4.1}$$

where σ_i' denotes the angular rms spread of the particles passing the $(i,j)_{\mathrm{th}}$ hole and σ_{ij} is the rms size of the hole. For circular holes with radii r, $\sigma_{ij} = r/2$, and since it is very small compared to the beamlet size, it can be neglected. The profiles of individual beamlets can be used to extract information on the angular distribution of the beam at the position of the hole defining the beamlet. It can be expressed as

$$\sigma_{ij}' = \frac{x_{2,ij,rms}}{l}. \tag{4.2}$$

Since the angular distribution x' at different hole positions x is known, the transverse

phase space can be reconstructed and the emittance can be calculated. However, the emittance may be underestimated, as the setup is susceptible to underestimation of the beamlet size. There is reduction in signal strength of the beamlet due to the small holes in the mask, since only a very small fraction of particles can pass through. Also, the beamlets should not overlap for a correct calculation of the beam moments. This requires the beam to be divergent at the slit mask, i.e., $\langle xx' \rangle \geq 0$, and the uncorrelated divergence $\langle x'^2 \rangle$ to be sufficiently small. Moreover, for a correct calculation of the beam momenta, the number of holes covering the beam has to be sufficient. This makes pepper pot technique unsuitable for small and space charge dominated beams, like the ones at PITZ. The manufacturing of masks containing small holes with minimum distance is also a challenge.

Slit scan

The slit scan technique is a variant of the pepper pot technique, the difference being that instead of having an array of holes in the mask, there is only a single slit of a certain width Δ. It is also based on the measurement of the electron beam size and its angular spread. The set up consists of a movable slit to chop the beam and a screen downstream to measure the spread of the resultant beamlet, see Figure 4.2. For the phase space reconstruction, the angular spread is calculated analogue to Eq. 4.2, whereas the rms size of the beam at the location right after the slit is given by $\sigma_i = \Delta/\sqrt{12}$. Since the scanning of the slit is required, it is a multishot method and requires a stable beam. By scanning the slit (vertical slit to reconstruct horizontal phase space and horizontal slit to reconstruct vertical phase space), the 2D transverse phase space is reconstructed and ϵ_x and ϵ_y are calculated. Since there is only one beamlet at a time, it cannot overlap with the other beamlets. However, this method is also prone to emittance underestimation due to the low charge density on the observation screen, but less as compared to the pepper pot.
At PITZ, the slit scan technique is utlized to measure the 2D transverse phase space [16, 17, 40]. The beam size is measured on a YAG screen installed at the slit station which is often slightly larger than the phase space beam size $\sqrt{\langle x^2 \rangle}$. This is because the low signal-to-noise ratio at the outer slit positions leads to an underestimation of the beam size calculated from the phase space. The fraction

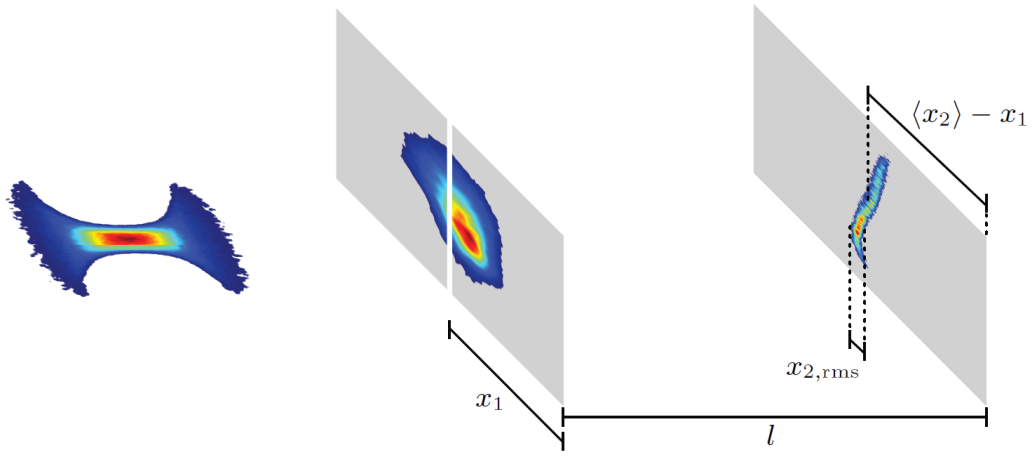

Figure 4.2: A vertical slit traversing the beam and a beamlet is observed on the beamlet collector screen for every slit position i [40].

between both sizes is used to calculate the scaled emittance, with the scaling factor f defined as

$$f = \frac{\sigma_x}{\sqrt{\langle x^2 \rangle}}. \tag{4.3}$$

The unscaled emittance is regarded as the lower limit for the emittance and the square of this scaling factor is regarded as the upper limit. The projected emittance can be measured both in the horizontal plane and the vertical plane. Then the ϵ_{xy} emittance is calculated via

$$\epsilon_{xy} = \sqrt{\epsilon_x \epsilon_y}. \tag{4.4}$$

where ϵ_x and ϵ_y are the scaled emittance in the horizontal and vertical plane, respectively. Note, that this is not the same as the transverse 4d-emittance, as the correlation terms between the two transverse planes are not determined here.

Virtual pepper pot

The virtual pepper pot is a novel method that is introduced at PITZ for 4D phase space measurements. It eliminates the mechanical design considerations imposed by small beams and the requirement for diverging beams but relies on stable machine operation due to its multi-shot measurement procedure. The method is named so, because there is no actual pepper pot plate, rather a pepper pot like pattern is

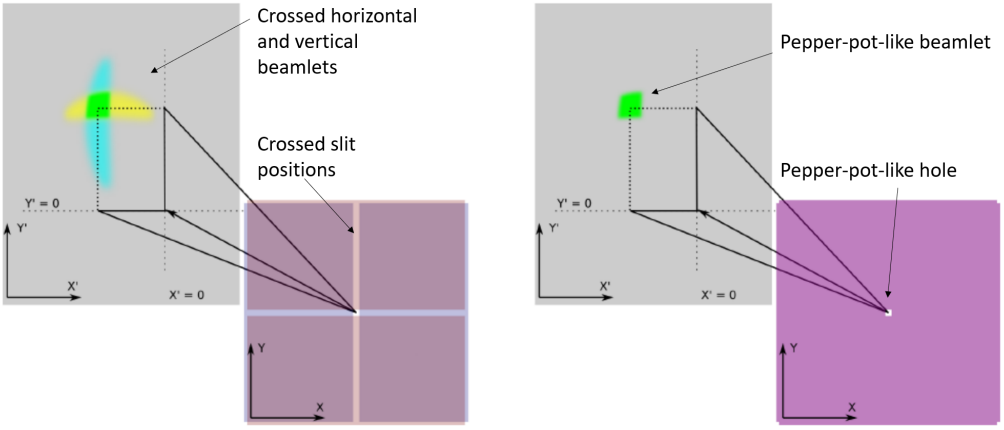

Figure 4.3: The image illustrates the idea of horizontal and vertical beamlet crossing in order to form a pepper-pot-like beamlet and known slit positions to form a pepper-pot-like hole [54].

generated by the horizontal and vertical slit scan data. From the slit scan technique, we have the beam intensity distribution at the slit location, the slit positions during the horizontal and vertical scans, and the beamlets at the beamlet collector screen. By finding the 2D beamlet distribution from the horizontal and vertical beamlets, one can determine the transverse coupling terms and calculate the 4D emittance.
In order to accurately determine the coupling in the beam, a crucial step is *how* to obtain the 2D beamlet distribution function from the slit scan beamlets. In the virtual pepper pot technique, the 2D beamlet distribution function is obtained by applying the *minimum bit principle*, i.e, generation of the virtual 2D beamlet from the intersection of the n^{th} x-beamlet and the m^{th} y-beamlet. This is done by setting each pixel value equal to the minimum from the corresponding values from both beamlets $min(x_{bl_n}, y_{bl_m})$. This 2D beamet will be a pepper-pot-like beamlet which will be assigned a pepper-pot-like hole determined by the horizontal and vertical slit positions, see Figure 4.3. The virtual holes with the beam distributions at those locations is referred to as *VPP mask* and the local beam distribution at the location of hole is called *VPP mask subimage*. These names will be used in the thesis onwards.

This chapter will describe the analytical model to find the horizontal and vertical phase space along with the transverse coupling terms in order to find the 4D transverse beam matrix. The proof-of-principle simulations done on ASTRA generated beams will be described step-by-step and the systematic error of the technique will be quantified by comparing the slit scan results to the VPP 2D sub-phase space results. The charge that is lost during the slit scan experiment due to low signal to noise ratio will be considered while applying VPP. Simulated beam with background noise level from the experiment will be used to estimate the charge cut and its effect on the emittance values. The VPP technique will also be applied to a simulated beam with coupled transverse phase space to demonstrate the diagnostic capability. Next, the technique will be implemented on the experimental data at PITZ. First, it will be bench marked with the slit scan results for beams with different focusing from the main solenoid and then, to the beams with a fixed solenoid current but undergoing effective rotation from a normal and skew gun quadrupoles. The chapter ends with a summary of the method and its findings.

4.2 Analytical modelling

The horizontal and vertical 2D phase space distribution functions $F(x, p_x)$ and $F(y, p_y)$ can be represented as a superposition of contributions from the beamlets' distribution functions $\sum_n F_n(x, p_x)$ and $\sum_m F_m(y, p_y)$, respectively. For practical considerations, let us introduce a coordinate transformation. For particles propagated downstream the slits, one obtains the following coordinates at the screen for the beamlet (bl) observation:

$$\begin{aligned} x_{bl} &= x + \frac{p_x}{p_z} \cdot L, \\ y_{bl} &= y + \frac{p_y}{p_z} \cdot L, \end{aligned} \tag{4.5}$$

where L is a distance from the slit mask to the beamlet observation screen and p_z is the beam longitudinal momentum. For further integrations, the following relationship will be used:

$$F(x, p_x) \cdot dx \cdot dp_x = \frac{p_z}{L} \cdot F(x, x_{bl}) \cdot dx \cdot dx_{bl}, \tag{4.6}$$

which is also valid for the partial distribution functions of the beamlets. The slit method assumes no correlations between a measuring beamlet, so the beamlet distribution function can be factorized as:

$$F_n(x, x_{bl}) = F_{1n}(x) \cdot F_{2n}(x_{bl}). \tag{4.7}$$

Using this assumption, the expression for the average squared transverse momentum takes the form:

$$\begin{aligned} \langle p_x^2 \rangle &= \iint p_x^2 \cdot F(x, p_x) \cdot dx \cdot dp_x \\ &= \left(\frac{p_z}{L}\right)^2 \cdot \iint (x_{bl} - x)^2 \cdot F(x, x_{bl}) \cdot dx \cdot dx_{bl} \\ &= \left(\frac{p_z}{L}\right)^2 \cdot \sum_n \iint (x_{bl} - x)^2 \cdot F_{1n}(x) \cdot F_{2n}(x_{bl}) \cdot dx \cdot dx_{bl} \\ &= \left(\frac{p_z}{L}\right)^2 \cdot \sum_n w_n \cdot \{\langle x^2 \rangle_n + \langle x_{bl}^2 \rangle_n + (\langle x \rangle_n - \langle x_{bl} \rangle_n)^2\}, \end{aligned} \tag{4.8}$$

where $\langle x_{bl}^2 \rangle_n$ is the square of the rms size of the n^{th} beamlet at the beamlet observation screen and $\langle x^2 \rangle_n$ is the square of the distribution within the slit at the n^{th} position. Note that $(x_{bl} - x)^2 = x_{bl}^2 + x^2 - 2x_{bl}x$. Solving this expansion by substituting $x_{bl} = \Delta x_{bl} + \bar{x}_{bl}$ and $x = \Delta x + \bar{x}$ yields $(x_{bl} - x)^2 = \Delta x_{bl}^2 + \Delta x^2 + (\bar{x} - \bar{x}_{bl})^2$. Integrating the first two terms give the rms size for the n^{th} beamlet on the observation screen and the rms beam size at the n^{th} slit location. The last term represents position of the center of n^{th} beamlet corresponding to the center of the n^{th} slit.

By assumption of a small slit opening Δ (or assuming homogeneous distribution within the slit opening) $\langle x^2 \rangle_n \approx \Delta^2/12$. $\langle x \rangle_n$ and $\langle x_{bl} \rangle_n$ are mean values of the slit positions and the corresponding beamlets' positions, respectively and w_n corresponds to the weight (charge) of each beamlet. The correlation term can be calculated using the same approach:

$$\begin{aligned}
\langle x \cdot p_x \rangle &= \iint x \cdot p_x \cdot F(x, p_x) \cdot dx \cdot dp_x \\
&= \left(\frac{p_z}{L}\right) \cdot \iint x \cdot (x_{bl} - x) \cdot F(x, x_{bl}) \cdot dx \cdot dx_{bl} \\
&= \left(\frac{p_z}{L}\right) \cdot \sum_n \iint x \cdot (x_{bl} - x) \cdot F_{1n}(x) \cdot F_{2n}(x_{bl}) \cdot dx \cdot dx_{bl} \\
&= \left(\frac{p_z}{L}\right) \cdot \sum_n w_n \cdot \{\langle x \rangle_n \cdot \langle x_{bl} \rangle_n - \langle x \rangle_n^2 - \langle x_{bl}^2 \rangle_n\}.
\end{aligned} \tag{4.9}$$

The equation for the rms beam size squared can be calculated using the same formula:

$$\langle x^2 \rangle = \sum_n w_n \cdot \{\langle x \rangle_n^2 + \langle x^2 \rangle_n\} = (X_{rms})^2 . \tag{4.10}$$

Similar to the horizontal scan, the equations for the vertical beam size, divergence and correlation can be derived from the M vertical beamlets and the corresponding slit positions. They are expressed as:

$$\langle y^2 \rangle = \sum_m w_m \cdot \{\langle y \rangle_m^2 + \langle y_{bl}^2 \rangle_m\} = (Y_{rms})^2 , \tag{4.11}$$

$$\langle p_y^2 \rangle = \left(\frac{p_z}{L}\right)^2 \cdot \sum_m w_m \cdot \{\langle y^2 \rangle_m + \langle y_{bl}^2 \rangle_m + (\langle y \rangle_m - \langle y_{bl} \rangle_m)^2\}, \tag{4.12}$$

$$\langle y \cdot p_y \rangle = \left(\frac{p_z}{L}\right) \cdot \sum_m w_m \cdot \{\langle y \rangle_m \cdot \langle y_{bl} \rangle_m - \langle y \rangle_m^2 - \langle y_{bl}^2 \rangle_m\}. \tag{4.13}$$

Following the same pattern, one could estimate $x - y$ correlation in 4D phase space (x, y, p_x, p_y). The 4D TPS distribution function can be represented as

$$F(x, y, p_x, p_y) = \sum_{n,m} F_{nm}(x, y, p_x, p_y) = \sum_{n,m} F_{1nm}(x) \cdot F_{2nm}(y) \cdot F_{3nm}(p_x, p_y). \tag{4.14}$$

Here x and y are assumed independent since the slit opening is only 50 µm. Applying coordinate substitution again, one obtains for the 2D beamlet distribution function

$$F_{3nm}(p_x, p_y) = F_{3nm}(x_{bl}, y_{bl}), \tag{4.15}$$

and for the 4D distribution function:

$$F(x, y, p_x, p_y) = \left(\frac{p_z}{L}\right)^2 \cdot \sum_{n,m} F_{1nm}(x) \cdot F_{2nm}(y) \cdot F_{3nm}(x_{bl}, y_{bl}) \cdot dx \cdot dy \cdot dx_{bl} \cdot dy_{bl}. \tag{4.16}$$

The calculation of the $\langle x \cdot y \rangle$ correlation can be obtained from the entire beam distribution at the slit location and can be determined by the beam tilt in a straightforward way.

$$\langle x \cdot y \rangle = \sum_{n,m} w_{x,nm} \cdot \{\langle x \rangle_n \cdot \langle y \rangle_m + \langle x_n \cdot y_m \rangle\}. \tag{4.17}$$

For the correlation term $\langle x \cdot p_y \rangle$ (assuming centered phase space distribution - $\langle x \rangle = 0; \langle p_y \rangle = 0$):

$$\begin{aligned} \langle x \cdot p_y \rangle =& \frac{p_z}{L} \cdot \sum_{n,m} \iiiint x \cdot (y_{bl} - y) \cdot F_{1nm}(x) \cdot F_{2nm}(y) \cdot F_{3nm}(x_{bl}, y_{bl}) \cdot dx \cdot dy \cdot dx_{bl} \cdot dy_{bl} \\ =& \frac{p_z}{L} \cdot \sum_{n,m} w_{x,nm} \cdot w_{y,nm} \cdot w_{bl,nm} \cdot \{\langle x \rangle_n \cdot \langle y_{bl} \rangle_m - \langle x \rangle_n \cdot \langle y \rangle_m - \langle x_n \cdot y_m \rangle\}. \end{aligned} \tag{4.18}$$

Analogously for $\langle y \cdot p_x \rangle$:

$$\langle y \cdot p_x \rangle = \frac{p_z}{L} \cdot \sum_{n,m} w_{x,nm} \cdot w_{y,nm} \cdot w_{bl,nm} \cdot \{\langle y \rangle_n \cdot \langle x_{bl} \rangle_m - \langle y \rangle_n \cdot \langle x \rangle_m - \langle x_n \cdot y_m \rangle\}. \tag{4.19}$$

For the momentum-momentum correlation $\langle p_x \cdot p_y \rangle$:

$$\begin{aligned}\langle p_x \cdot p_y \rangle &= \left(\frac{p_z}{L}\right)^2 \cdot \sum_{n,m} \iiiint (x_{bl} - x) \cdot (y_{bl} - y) \cdot F_{1nm}(x) \cdot F_{2nm}(y) \cdot \\ &\quad F_{3nm}(x_{bl}, y_{bl}) \cdot dx \cdot dy \cdot dx_{bl} \cdot dy_{bl} \\ &= \left(\frac{p_z}{L}\right)^2 \cdot \sum_{n,m} w_{x,nm} \cdot w_{y,nm} \cdot w_{bl,nm} \cdot \{\langle x_{bl} \rangle_n \cdot \langle y_{bl} \rangle_m - \langle x_{bl} \rangle_n \cdot \langle y \rangle_m - \langle x \rangle_n \cdot \langle y_{bl} \rangle_m \\ &+ \langle x \rangle_n \cdot \langle y \rangle_m + \langle x_{bl_n} \cdot y_{bl_m} \rangle + \langle x_n \cdot y_m \rangle\},\end{aligned} \tag{4.20}$$

where $\langle x_{bl_n} \cdot y_{bl_m} \rangle = \iint (x_{bl_n} \cdot y_{bl_m}) \cdot F_{3nm}(x_{bl}, y_{bl}) \cdot dx_{bl} \cdot dy_{bl}$ is the term corresponding to the beamlet tilt.
After the correlations terms are estimated from the VPP beamlets and mask subimages, the correlation C_{xy} can be calculated as:

$$C_{xy} = \langle x \cdot y \rangle \cdot \langle p_x \cdot p_y \rangle - \langle x \cdot p_y \rangle \cdot \langle y \cdot p_x \rangle. \tag{4.21}$$

Since now we have all the horizontal, vertical and coupling terms, the 4D Transverse Beam Matrix (TBM) that describes the transverse statistical properties of the beam can be defined as follows [58]:

$$\sigma_{4D} = \begin{bmatrix} \langle x^2 \rangle & \langle x \cdot p_x \rangle & \langle x \cdot y \rangle & \langle x \cdot p_y \rangle \\ \langle x \cdot p_x \rangle & \langle p_x^2 \rangle & \langle y \cdot p_x \rangle & \langle p_x \cdot p_y \rangle \\ \langle x \cdot y \rangle & \langle y \cdot p_x \rangle & \langle y^2 \rangle & \langle y \cdot p_y \rangle \\ \langle x \cdot p_y \rangle & \langle p_x \cdot p_y \rangle & \langle y \cdot p_y \rangle & \langle p_y^2 \rangle \end{bmatrix} = \begin{bmatrix} \sigma_{xx} & \sigma_{xy} \\ \sigma_{xy}^T & \sigma_{yy}. \end{bmatrix} \tag{4.22}$$

The 4D emittance can be found by taking determinant of the 4D TBM:

$$\epsilon_{4D} = \sqrt[4]{det(\sigma_{4D})}. \tag{4.23}$$

The matrices σ_{xx} and σ_{yy} describe the 2D horizontal and vertical distributions, and σ_{xy} describes the cross-plane coupling. If the beam is transversely decoupled, i.e, $\sigma_{xy} = 0$, the 2D beam matrices are sufficient to characterize the beam. If one or more elements of σ_{xy} are nonzero, the beam is $x - y$ coupled, and the projections

onto the x and y planes exhibit an increase of the observed emittance values. The diagonalization of the 4D beam matrix yields the intrinsic emittances ϵ_1 and ϵ_2 [58].

$$U^T \sigma_{4D} U = \begin{bmatrix} \epsilon_1 & 0 & 0 & 0 \\ 0 & \epsilon_1 & 0 & 0 \\ 0 & 0 & \epsilon_2 & 0 \\ 0 & 0 & 0 & \epsilon_2 \end{bmatrix}. \tag{4.24}$$

The product of the intrinsic emittances will always be less than the product of the apparent emittances:

$$\epsilon_1 \cdot \epsilon_2 \leq \epsilon_x \cdot \epsilon_y. \tag{4.25}$$

The transverse coupling contribution to the apparant emittances can be quantified by the coupling factor. From this one can find the beam coupling factor defined by [59],

$$t = \frac{\epsilon_{xy}}{\epsilon_{4D}} - 1 \geq 0. \tag{4.26}$$

For t=0, the beam is decoupled and the apparent emittances have minimal values, while for $t > 0$ the beam is transversely coupled and the apparent emittances are increased. Also, the generalized emittance invariant in 4D phase space can be calculated. The invariant remain constant when the beam travels in linear accelerator optics [60].

$$I_s = \epsilon_x^2 + \epsilon_y^2 + 2C_{xy}^2. \tag{4.27}$$

One can also calculate the rotation angle φ_{cal} between the transverse planes with the help of coupling terms e.g.

$$\varphi_{cal} = atan\left(\frac{\langle x \cdot p_y \rangle}{\langle x \cdot p_x \rangle}\right). \tag{4.28}$$

The correlation angle φ_{cor} can then be calculated from the rotation angle φ_{cal} by [61]:

$$\tan \varphi_{cor} = -\frac{1}{2} \cdot \tan 2\varphi_{cal} \cdot \frac{p_{y,max}^2 - p_{x,max}^2}{p_{x,max}^2}. \tag{4.29}$$

The axis defined by the angle φ_{cor} is not a principle axis of the ellipse, but it is a symmetry axis in the sense that at any position x the distance Δy between the axis

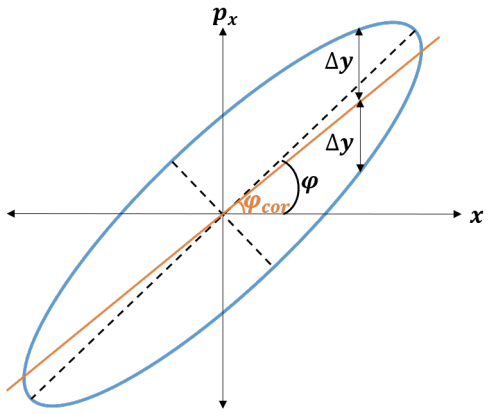

Figure 4.4: Ellipse with principle axes and correlation axis [61].

and the upper and the lower branches of the ellipse is equal as indicated in Fig. 4.4. Thus the line defined by φ_{cor} corresponds to a line obtained by a straight line fit through the distribution with an RMS minimization. While the angle φ_{cal} defines the rotation angle of the principle axes of the ellipse, φ_{cor} is related to a shearing of the ellipse. If the ellipse is sheared by an angle φ_{cor} the principle axes of the ellipse will be on the axes of the coordinate system as in the case of a rotation by an angle φ_{cal} [61].

Most FEL main linac lattice design assumes no transverse coupling and therefore the injector needs to decouple x/y phase space to make full use of beam brightness $\mathcal{B}$.

$$\mathcal{B} = \frac{Q}{\epsilon_x \cdot \epsilon_y} = \frac{Q}{\epsilon_{4D}^2}. \tag{4.30}$$

After the analytical modelling, a VPP tool was developed and tested on simulated beams. The systematic error of the method was estimated with a simulated beam and the algorithm's accuracy in case of coupled beams was also studied.
One possible problem from a practical implementation point of view is the different normalization of x and y measured phase spaces, which could be caused by variable number of pulses used for the slit scans and different effective slit opening (i.e. slit orientation). The solution adapted was a renormalization of the profiles obtained from the slit scans to unity with a subsequent renormalization of the corresponding 1D beamlets.

4.3 Proof-of-principle simulation

To perform the proof-of-principle simulations for VPP, A Space Charge Tracking Algorithm (ASTRA) [62] was used to generate and track the particles until EMSY1. The ASTRA beam was produced by a 6 ps FWHM temporal-gaussian laser and a charge of 250 pC was extracted. The beam parameters were kept close to the typical experimental conditions. Gun momentum was close to 6.3 MeV/c, and after the booster it was around 19.3 MeV/c. A solenoid current scan was done to find the minimum emittance point. The current was varied from 364 A to 368 A with a step size of 1 A. Then, the solenoid current was kept constant (corresponding to minimum emittance point) and number of macroparticles were varied as follows; 0.2, 0.5, 0.7, 1 and 2 million. Simulation of 2 million macroparticles is computationally expensive and takes approximately 48 hours. The idea behind the simulation with different number of particles was to know the dependence of emittance results, if any, on the number of macroparticles. A minimum projected horizontal and vertical emittance of 0.61 mm mrad was calculated from ASTRA. The 4D transverse phase space for 2 million particles is shown in Figure 4.5. The resolution is kept 0.05 mm per pixel.

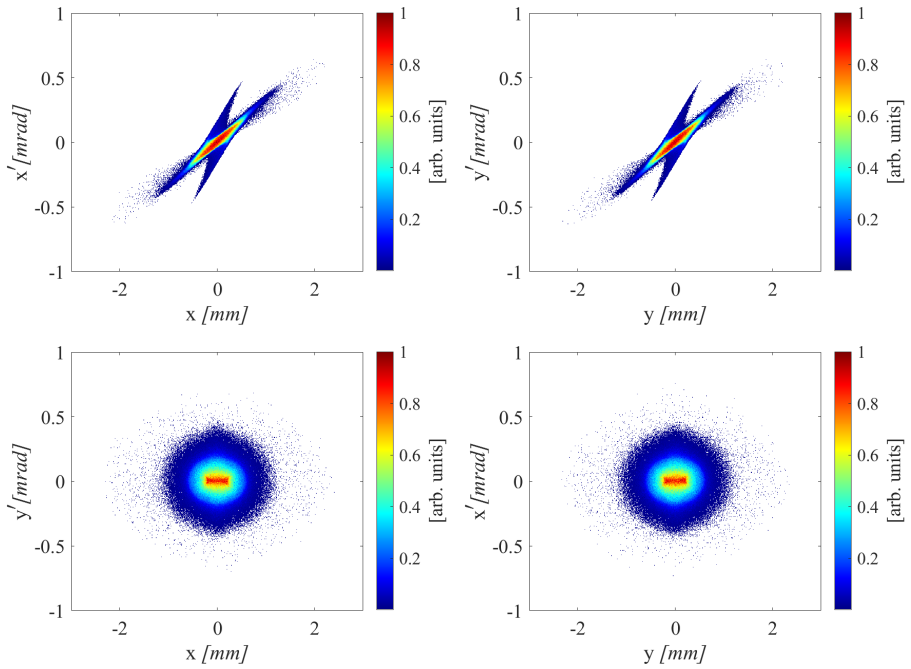

Figure 4.5: 4D TPS of simulated beam, charge 250 pC and momentum 19.3 MeV/c.

Next, the beam distribution at the slit location was used to generate slit scan files similar to the experimental data files. To create the slit scan files, a beamlet collector screen, also known as Mask Of Interest (MOI), at a distance of 3.133 m from the slit location was used, analogous to the experimental set up. The image resolution of the beam distribution at the slit location and at the beamlet collector screen was kept 0.035 mm and 0.039 mm, respectively, identical to the camera resolution at these locations. The files included the following information about the beam; beam distribution at the slit location and its size, beam distribution at the beamlet collector screen, beamlet images, beam momentum, drift length between the two screens, slit scan speed and the slit position coordinates. All these files were generated in matlab. Initially, the conventional slit scan methodology was applied to the simulated slit scan data and the 2D horizontal and vertical phase spaces were reconstructed. Then the same data was fed to the VPP tool to reconstruct 4D phase space. The slit scan results were used to bench mark VPP horizontal and vertical sub phase spaces in order to investigate the systematic error of the VPP technique.

Before explaining the VPP algorithm in detail, a quick comparison of emittance values for ASTRA, slit scan and VPP with different number of particles is done. Figure 4.6 shows emittance results (identical for x and y) for all the cases. Using ASTRA monitor, the results show constant numbers. For the case of slit scan, as the number of particles increase, the emittance is increased by 0.1 mm mrad until it stabilizes at 2 million particles. For the case of VPP, it was found that the emittance numbers are very sensitive to the number of particles. Even at 2 million particles, they are just at the onset of stable values. All the simulations for the methodological studies of VPP were done with 2 million particles. One can also do the charge cut on phase space to do a quick check on where does this difference in emittance values come from. The charge cut on phase space is defined as the integral of the particles that is removed when we slice the phase space transversely. All the curves coincide after approximately 20 % of the phase space charge cut, see Figure 4.7. This shows that the difference in emittance comes from the halo part of the beam phase space.

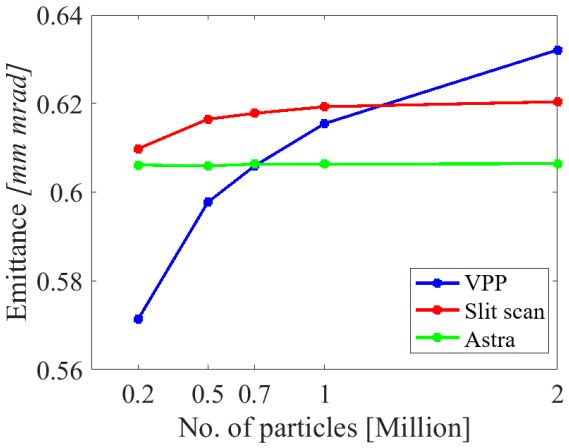

Figure 4.6: Effect of changing the number of ASTRA macroparticles on the emittance values for a solenoid current value of 366 A.

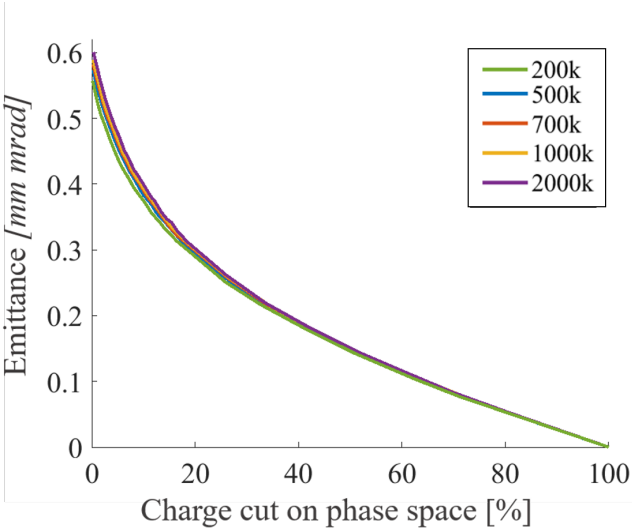

Figure 4.7: The curves coincide after approximately 20 % of the phase space charge cut, indicating the difference in emittance comes from the halo part of the beam phase space.

4.3.1 Methodical studies

Let us study the real and the phase space distribution for the beam with the minimum emittance found in simulations after the solenoid scan. Beam distribution of the simulated beam at the slit position EMSY1 with an x and y rms beam size is 0.37 mm. Beam distribution of the simulated beam at the beamlet collector screen (MOI) with x and y rms beam sizes 0.7417 mm. Figure 4.8 shows the beam distribution at EMSY1 and MOI screen with the screen resolution similar to the experimental set up. The projected x and y emittance using the slit scan technique was found to be 0.6227 mm mrad. The relative error between ASTRA and slit scan emittance value is found to be approximately 2.08 %.

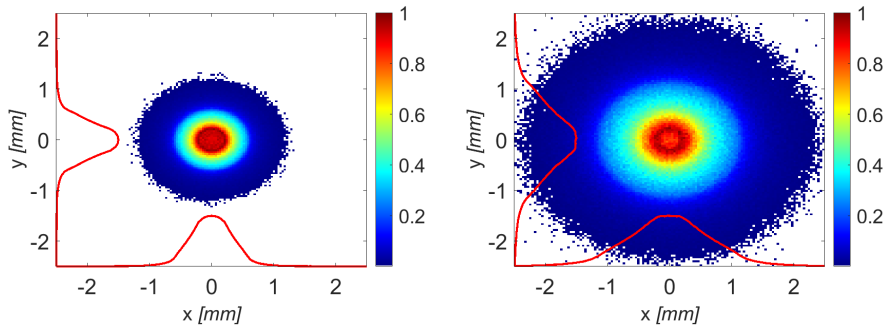

Figure 4.8: (left) Beam distribution at EMSY1 with an x and y rms beam size 0.37 mm. (right) Beam distribution at MOI with x and y rms beam sizes 0.7417 mm.

The post-processing of the slit scan data to generate the VPP results consists of many steps. For the purpose of illustration, every 5^{th} horizontal and vertical beamlet will be used (0.25 mm distant beamlets) to generate VPP beamlet and VPP mask.

- First, all the horizontal and vertical beamlets are renormalized to the beam distribution at EMSY1 location. Fig. 4.9 shows the Sum of Pixels (SoP) of the horizontal and vertical beamlets before and after normalization, see y scale.
- The normalized beamlets are crossed, i.e., the pixel wise minimum of these beamlets is used to generate a VPP beamlet. Figure 4.10 shows the result of crossing different horizontal and vertical beamlets. The distribution of the VPP beamlet depends upon the distribution of the particles in the horizontal and vertical beamlets that are being crossed.

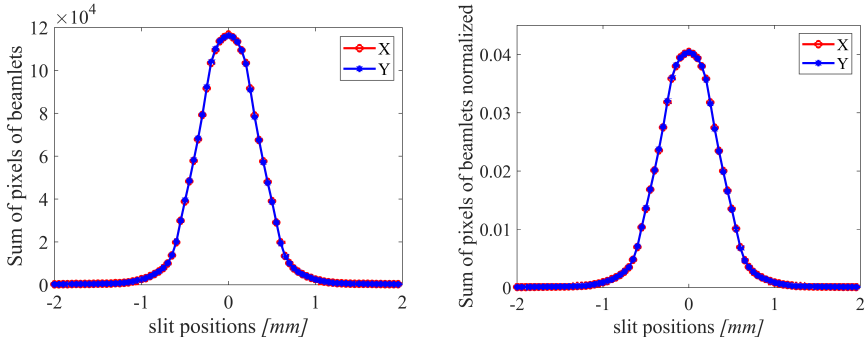

Figure 4.9: (left) Sum of pixels of horizontal and vertical beamlets. (right) Sum of pixels of beamlets nomarlized to EMSY1 projections.

- The VPP mask sub-images are created from the known slit positions and the whole beam distribution at these positions. Figure 4.11 shows the VPP mask and the beamlets. Since every 5^{th} beamlet was crossed, the mask subimages and beamlets are well apart and visible. The different size of mask sub-images inspite of fixed slit width is because of rounding off of pixels with defined camera resolution.

- The SoP(normalized) of the VPP beamlets is used as a weighting factor of all beamlets and mask subimages. The center of mass of each VPP beamlet and mask subimage is computed, followed by calculation of the common center of mass of all VPP beamlets and mask subimages. Then the beamlets and mask subimages are centralized w.r.t the common center of mass.

- The variance and covariance of the beamlets and mask subimages is calculated next. In case of no coupling between the transverse phase space, covariance values are negligible. The mask subimages variance values are less than a µm because of small slit width.

- All the values of first and second order centralized moments and their corresponding weights are finally plugged in the formulas of beam sizes, divergences and correlations to construct the 4D Transverse Beam Matrix (TBM). The TBM, in turn, can be used to calculate the beam parameters that defines the properties of the beam.

- The knowledge of the VPP mask locations, first and second order centralized moments of beamlets can be used to reconstruct the 4D TPS, see Figure 4.12. The results show good agreement with the simulated 4D TPS shown in figure 4.5. The systematic error in the methodology are explained in section 4.3.2.

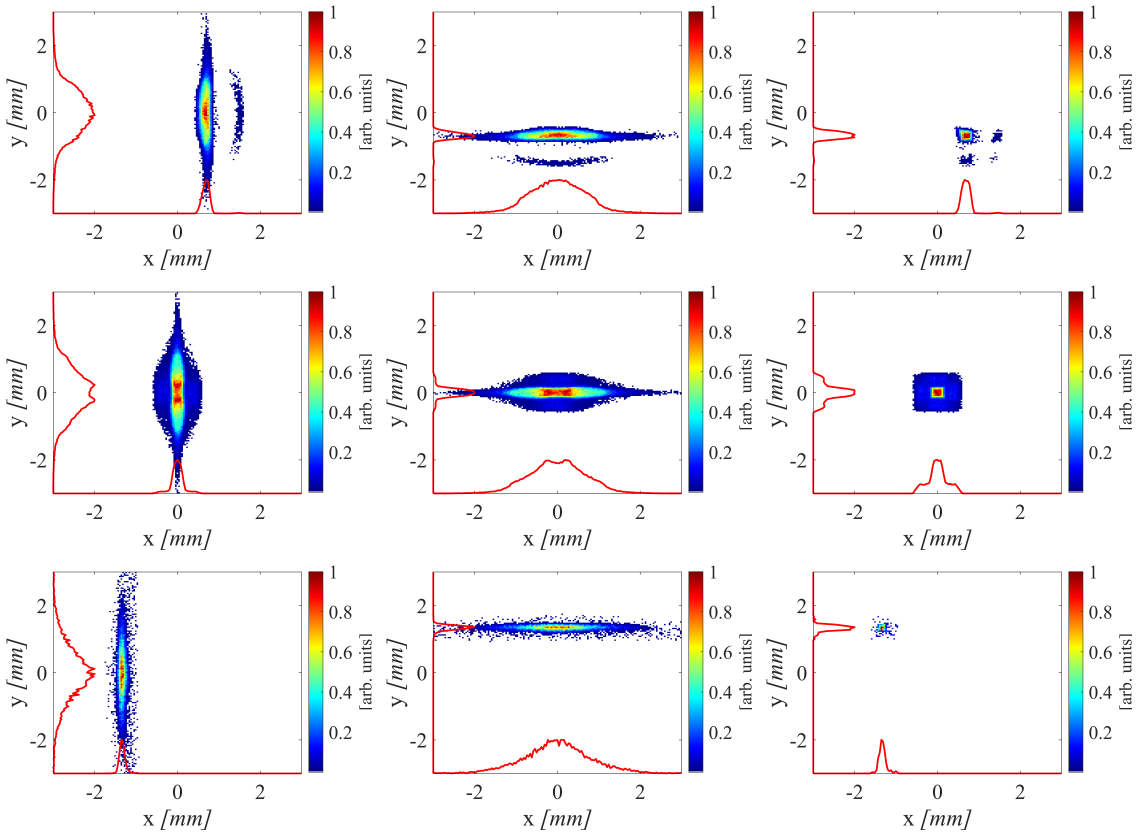

Figure 4.10: 1^{st} column shows the horizontal beamlets and the 2^{nd} column shows the vertical beamlets at different slit locations. The 3^{rd} column shows the VPP beamlet generated by taking pixel-wise minimum of the horizontal and vertical beamlets.

For practical beams, there are many challenges of the VPP method. The finite slit opening 50 µm plays a role. The EMSY1 station has a 10 µm slit installed too which gives better resolution, but since the signal strength becomes low, it is not used for VPP [16]. The core and halo structure in the beam distribution which is effected by the background noise, also poses a challenge for beam characterization by VPP (discussed in section 4.3.4).

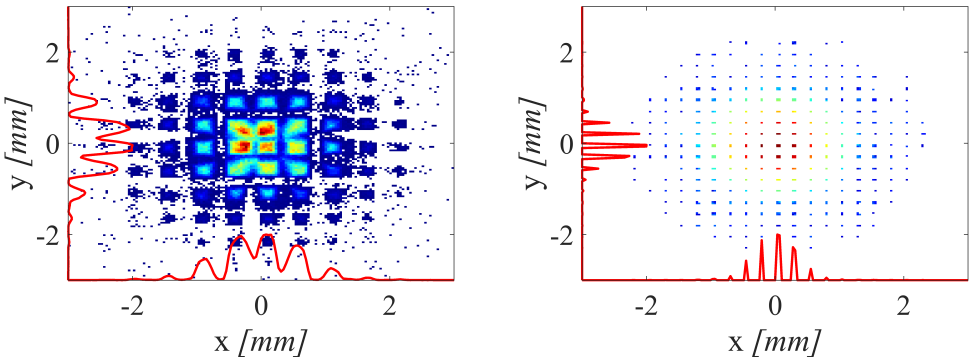

Figure 4.11: (left) VPP beamlets formed after crossing every 5^{th} horizontal and vertical beamlet (MOI). (right) VPP mask formed from known slit positions and beam distribution at the slit location (EMSY).

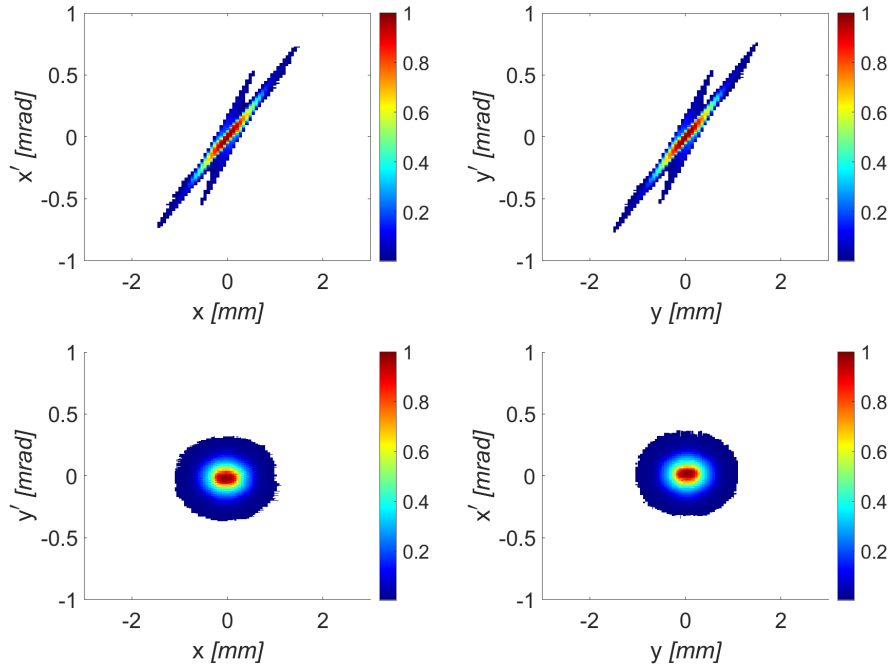

Figure 4.12: 4D transverse phase space for 250 pC beam.

The emittance results of the VPP simulation are shown for the case of crossing all the horizontal and vertical beamlets. The beam matrix gives the horizontal and vertical emittance values as well as the coupling term which enables to find the 4D emittance. In this case, since there is no coupling, the 4D emittance will be approximately equal to the 2D emittances. The relative error between ϵ_{xy} for both cases is approximately $-2.2\,\%$. Table 4.1 summarizes the results of slit scan and VPP and their relative error $\left(\frac{\epsilon_{slitscan}-\epsilon_{vpp}}{\epsilon_{slitscan}}\right)$.

-	ϵ_x	ϵ_y	ϵ_{xy}	ϵ_{4D}
Slit scan	0.6227	0.6227	0.6227	-
VPP	0.6320	0.6275	0.6298	0.6296

Table 4.1: Summary of slit scan and VPP results

One can also find the intrinsic emittances by diagonlization of the beam matrix. The eigen matrix that gives the intrinsic emittances is shown below. It can be further proved that Eq. 4.25 also holds, i.e, the product of the apparent emittances ($\epsilon_x\epsilon_y = 0.3966$) cannot be smaller than the product of the intrinsic emittances ($\epsilon_1\epsilon_2 = 0.3963$). Here ϵ_1 was taken as the average of first two diagonal values and ϵ_2 was taken as the average of last two diagonal values.

$$U^T\sigma_{4D}U = \begin{bmatrix} 0.1007 & 0 & 0 & 0 \\ 0 & 0.1017 & 0 & 0 \\ 0 & 0 & 3.904 & 0 \\ 0 & 0 & 0 & 3.928 \end{bmatrix}. \tag{4.31}$$

When the beam is coupled in the transverse phase space, ϵ_{4D} and ϵ_{xy} are different because of non-negligible coupling values. Section 4.3.3 discusses such cases in detail.

4.3.2 Systematic error

To ensure that the VPP can properly diagnose the TPS, the systematic error must be studied. Table 4.1 showed that the emittance is overestimated as compared to the slit scan results. To investigate the reason of this increase, one can dig deeper into the crossing of the horizontal and vertical beamlets. A VPP beamlet formed from the minimum bit method contains not only those particles that emerged from the VPP mask subimage region, but also the ones that diverged from the adjacent slit area. These particles in a VPP beamlet will be referred to as *foreign particles*. To illustrate the presence of *foriegn particles*, a VPP beamlet was compared to a real pepper pot beamlet. A simulated pepper pot beamlet is the one that actually emerged from a VPP mask subimage of area 0.05×0.05 mm^2, and is not formed by the crossing of horizontal and vertical slit scan beamlets. This mask subimage consists of only a few pixels and therefore, has a square-like shape. Figure 4.13 shows some pepper pot beamlets generated by a simulated beam. Figure 4.14 shows an example of a pepper pot mask and the corresponding beamlets. It is interesting to note that the pepper pot mask generated circular beamlets in contrast to the square-like beamlets generated by VPP (compare Fig. 4.14 and Fig. 4.11).

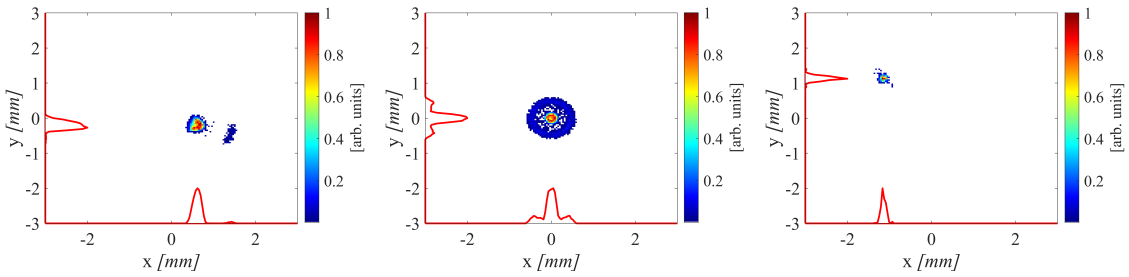

Figure 4.13: Pepper pot beamlets generated by a simulated beam.

Figure 4.15 compares the central beamlet of a virtual pepper pot and real pepper pot. The distribution of particles and their profiles are slightly different for both cases. The density of particles surrounding the core is lower in the case of the pepper pot and therefore a slope in the halo of x and y profiles is observed. In contrast, the slope of the halo appear to be flat in case of the VPP beamlet profile. This causes overestimation of the beamlet sizes, which in turn, is a source of the increase in the observed emittance values by around 2 %.

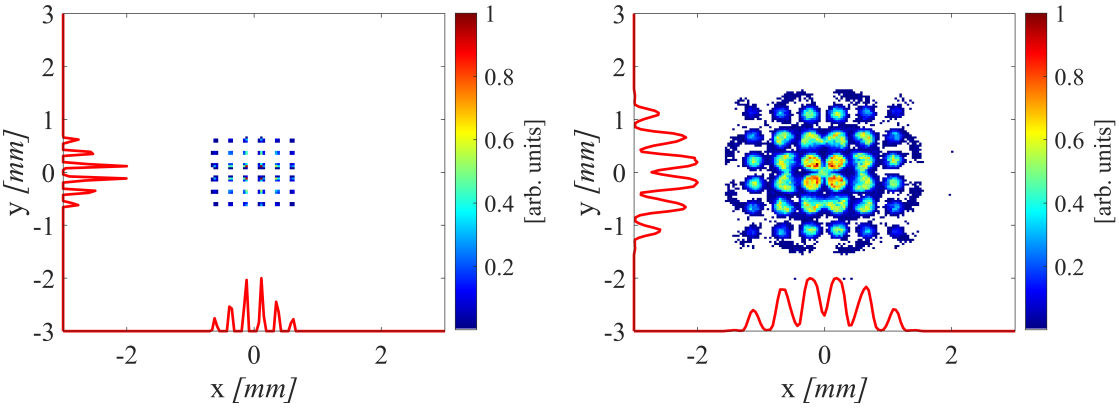

Figure 4.14: (left) Pepper pot mask. (right) Corresponding pepper pot beamlets.

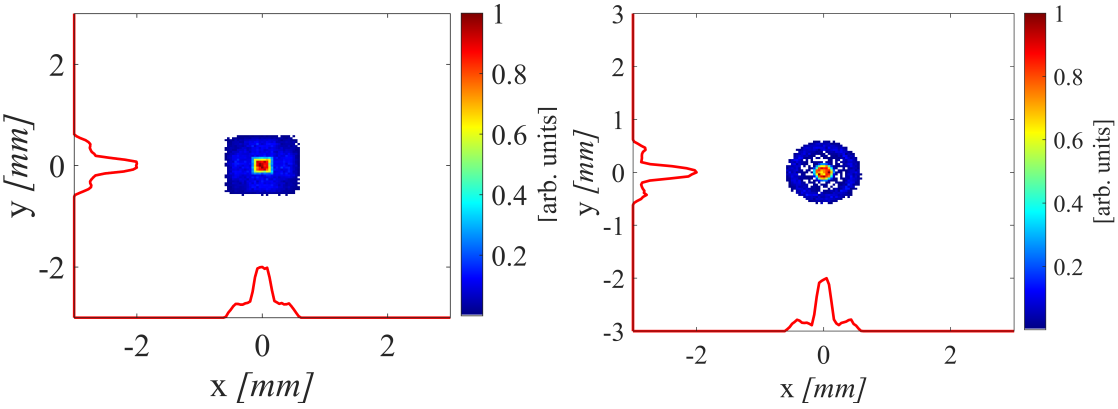

Figure 4.15: (left) Central virtual pepper pot beamlet. (right) Central *real* pepper pot beamlet.

To further cross check that the source of this rise in emittance is indeed due to the presence of *foreign particles*, all the VPP beamlets at a given x or y position were combined to recreate the horizontal and vertical beamlets. Then the conventional 2D phase space analysis was done. Figure 4.16 shows horizontal and vertical beamlet reconstructed from virtual pepper pot beamlet. For the purpose of illustration, every 5^{th} VPP beamlet were used. The emittance values agreed with the VPP results. To quantify the 2D sub phase space difference between the original slit scan and the VPP recreated slit scan, the horizontal and vertical phase spaces were subtracted and their l_2 norms ($\sqrt{\sum_i diff_i^2}$) were calculated.

A practical aspect from implementation point of view is optimization of time vs

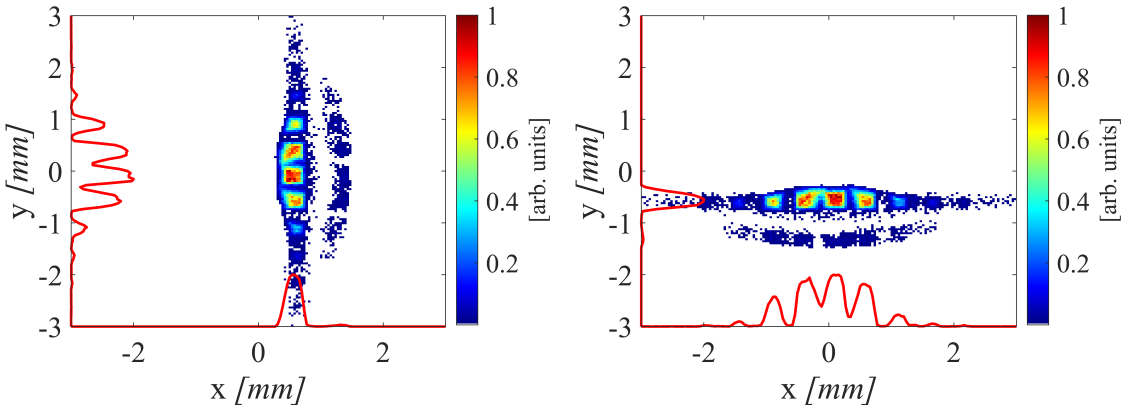

Figure 4.16: Slit scan like beamlets reconstructed from VPP: (left) Horizontal. (right) Vertical. Every 5^{th} beamlet is crossed.

accuracy. Crossing all the horizontal and vertical beamlets takes up quite a bit of processor memory and time. One could cross every 2^{nd} or 3^{rd} beamlet with a little impact on the emittance values but the resolution of the phase space degrades. Also, then it crucial not to miss the central beamlet that has the highest weight. The l_2 norm and ϵ_x values can be compared for all the above mentioned cases, see

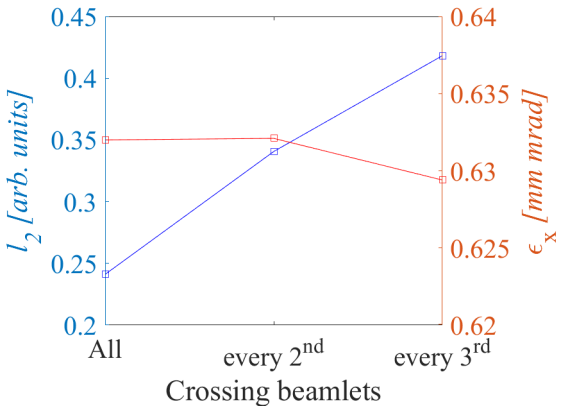

Figure 4.17: Comparison of l_2 norm and ϵ_x values for different cases of crossing of beamlets.

Figure 4.17. The l_2 norm values are normalized to 1 and the minimum is for the case when all the beamlets are crossed. The maximum relative change in ϵ_x value is only around 0.4 %. For different solenoid currents, the beam distribution (core and

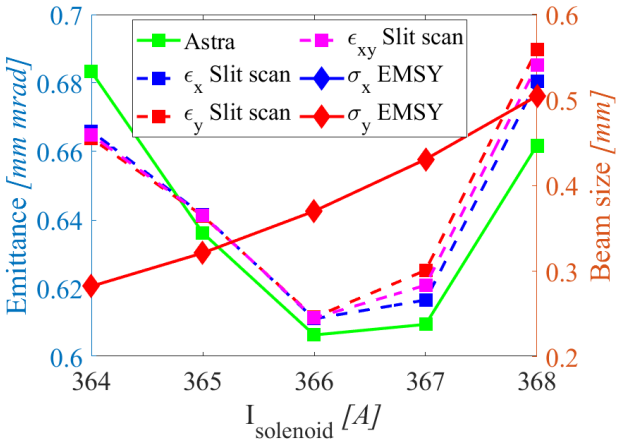

Figure 4.18: For solenoid current scan, ASTRA ($\epsilon_x = \epsilon_y$) and slit scan emittance results as well as beam sizes ($\sigma_x = \sigma_y$).

halo structure) at the slit location changes. When this beam is chopped by the slit to form the horizontal and vertical beamlets, the systematic error in the emittance values between the ASTRA and the slit scan varies, see Figure 4.18. Consequently, the systematic error in the emittance values between the slit scan and VPP also varies, since the VPP beamlets are formed from the slit scan beamlets. Therefore, one can say that the effect of foreign particles also depends on the original beam distribution. Figure 4.19 shows a comparison between the ASTRA, slit scan and VPP results for different solenoid currents. A charge cut is applied on the phase space reconstructed by the slit scan and VPP. Depending upon the contribution of foreign particles, the emittance calculated from VPP is either less or greater than the slit scan emittance. Nevertheless, the systematic error between slit scan and VPP is lowest for the solenoid current which gives the minimum emittance. Figure 4.20 shows the results of crossing every beamlet, every 2^{nd} beamlet and every 3^{rd} beamlet.

For practical beams, there are many sources of uncertainity in the measured data e.g. machine jitter, imperfections of the observation screen and TV system, discussed in detail in [20]. In this section, the motivation was to investigate the systematic error caused purely by the VPP methodology for ideal case.

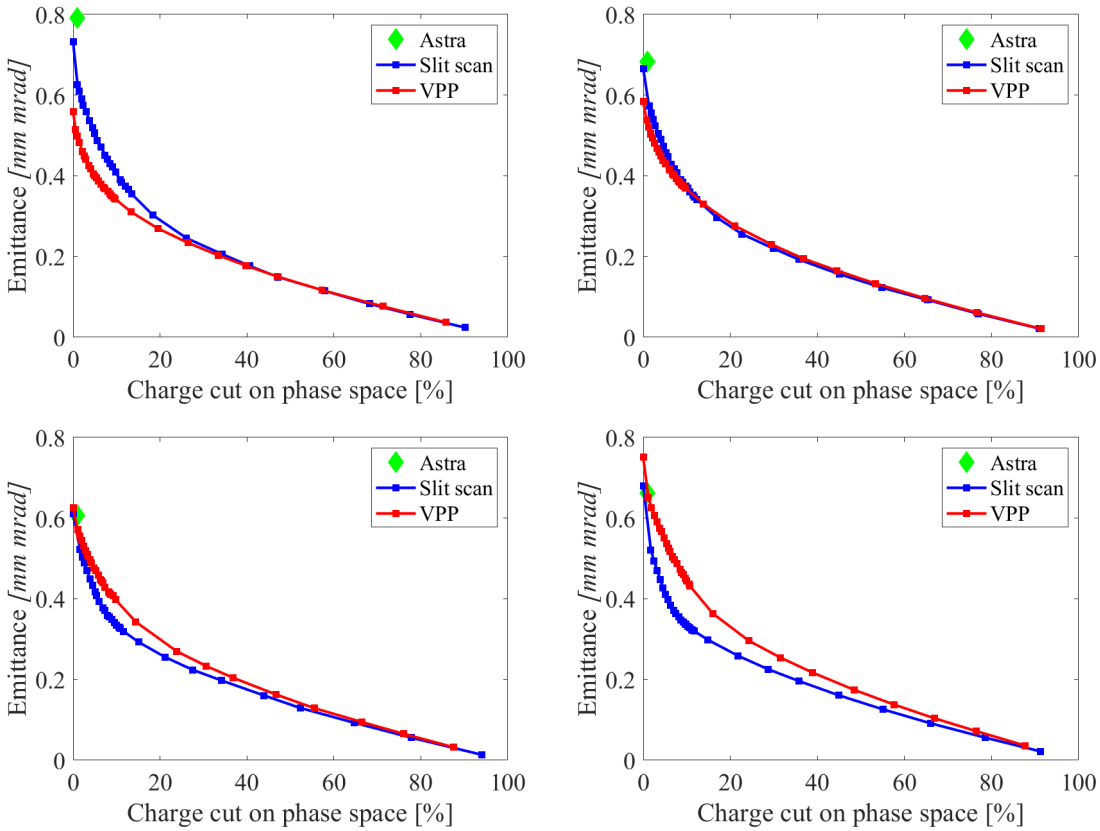

Figure 4.19: Charge cut on phase space for different solenoid currents (left top) 362 A (right top) 364 A (left bottom) 366 A (right bottom) 368 A. As the foreign particles contribution depend also on the initial distribution of particles at the slit location, the emittance values after phase space charge cut are also changing differently for all cases.

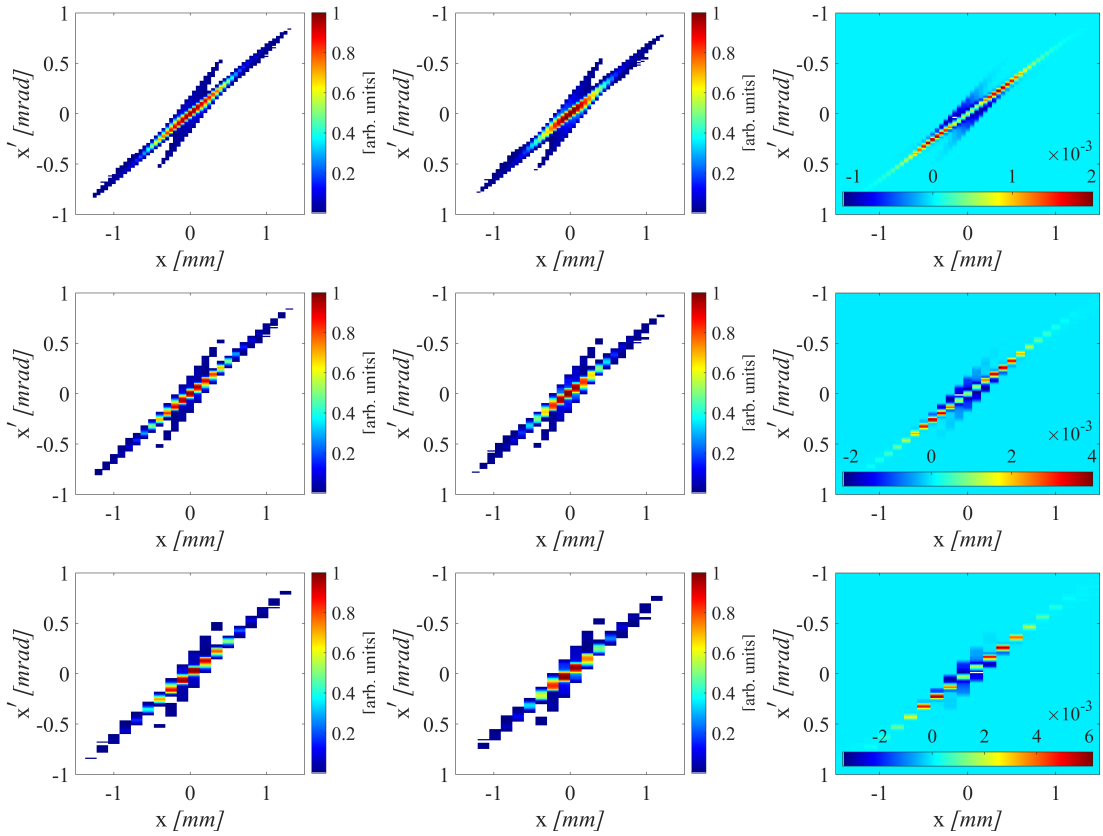

Figure 4.20: First column shows the slit scan results of horizontal phase space reconstructed from : every beamlet (top), every 2^{nd} beamlet (middle), every 3^{rd} beamlet (bottom). Second column shows the results of horizontal phase space reconstructed by crossing 2D beamlets recreated from the VPP beamlets: every horizontal and vertical beamlet (top), every 2^{nd} beamlet (middle), every 3^{rd} beamlet (bottom). The third column displays the pixel-by-pixel difference between the first and second column. The colour scale shows that the difference is of the order of 10^{-3}.

4.3.3 Coupled beam

Typically in the measurements on the beamline, the gun quadrupoles are used to make the beam transverse distributions rotationally symmetric. This is because of the requirements of different programs at PITZ to do round beam transport (e.g, THz and Radiation therapy). The beam is made symmetric in real space which may introduce additional coupling in phase space. Coupled transverse dynamics results when the electrons have azimuthal momenta, and their trajectories are no longer coplanar with the beam axis. The trajectories are *coupled* because the electron's x coordinate depends not just on x and p_x but also on y and p_y , and similarly for the y coordinate. To understand the effect of this coupling on the emittance and 4D transverse phase space [60], the beam was coupled in simulations. The phase space of the ASTRA generated beam can be coupled by rotating its momentum coordinates (p_x, p_y) at the slit location by an angle θ using the rotation matrix.

$$R = \begin{bmatrix} \cos\theta & -\sin\theta \\ \sin\theta & \cos\theta \end{bmatrix}. \tag{4.32}$$

Since the 4D rotation is linear, the 4D emittance does not grow. However there is emittance growth in both (x, p_x) and (y, p_y) phase spaces due to skew trajectories. The coupling between p_x and p_y does not make the beam asymmetric in real space but introduces a tilt within the beamlets. VPP can diagnose this tilt and hence reconstruct the 4D phase space of this coupled beam. Then, with the elements of the computed 4D TBM, one can find the coupling term C_{xy} and the kinematic invariant I in Eq. 4.27. Similarly, the coupling angle φ_{cal} can also be found which, in turn, can be used to compute the correlation angle φ_{ccor}.

To illustrate the 4D diagnostic capability of the VPP technique for the coupled beams, four different cases were considered: 10°, 30° , 60° and 90°. A wide range of rotation angles were tried to test the limits of VPP. Let us first compare the central beamlets for all the four cases since they have the highest intensity. Figure 4.21 shows the central horizontal beamlet, vertical beamlet and the result of crossing these beamlets. The VPP central beamlet spatial distribution is rotating which also changes its x and y projections. The correlations between these projections also changes and this would result in alteration of beam parameters.

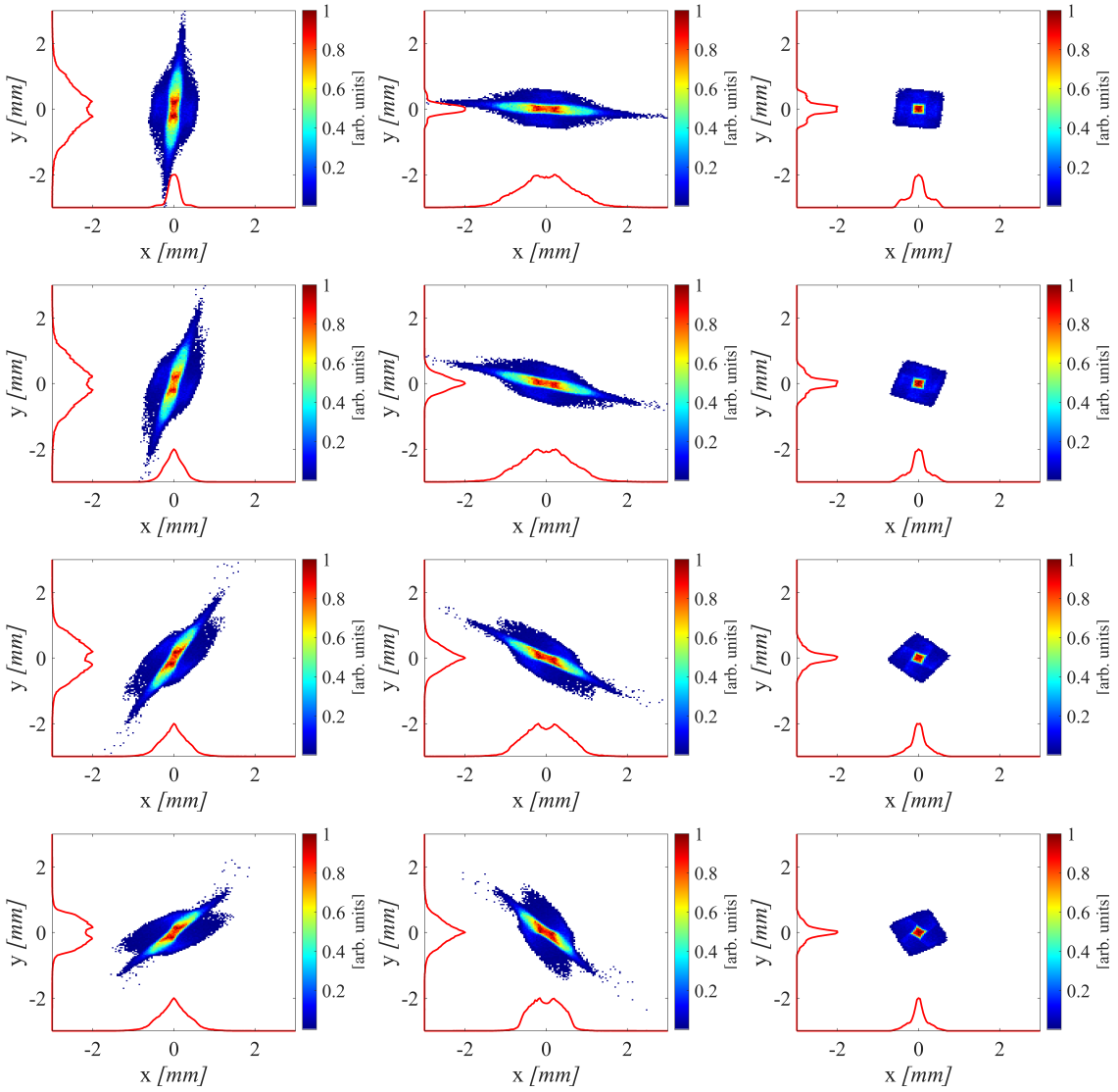

Figure 4.21: First column shows the horizontal beamlet, second column shows the vertical beamlet, third column shows the crossed beamlet. The rows show coupled beam (p_x, p_y) for the cases of 10°, 30°, 60° and 90° from top to bottom.

One can then compare the slit scan and VPP results for ϵ_x, ϵ_y and ϵ_{xy}. The coupling term is also calculated which enables to find ϵ_{4D}. The ϵ_{4D} should remain constant if the coupling term is computed correctly. Figure 4.22 (left) shows the rms beam sizes and the emittance results of the slit scan. As the rotation angle increased, the emittance also increased but the beam size remains constant. This is because only the momentum coordinates of the beam were rotated whereas the spatial distribution was not changed. Figure 4.22 (right) shows the emittance results from VPP, which also increase as the rotation angle increases. If one compares the values, then they agree for the first two cases and for the rest of the three values, VPP underestimates the emittance by almost 20 %. This discrepancy can be understood by comparing the central beamlet of simulated pepper pot and simulated VPP. The pepper pot central beamlet is rotationally symmetric and so remains same for the coupled beams too. In VPP, the central beamlet square-like distribution changes as shown in figure 4.21 last column. Therefore, the VPP results show deviation from the slit scan results for both horizontal and vertical emittance. It is note worthy that the 4D emittance value, which can only be calculated by VPP, remains approximately constant. This means that VPP correctly calculates the coupling term and therefore, is a promising tool for 4D diagnotics.

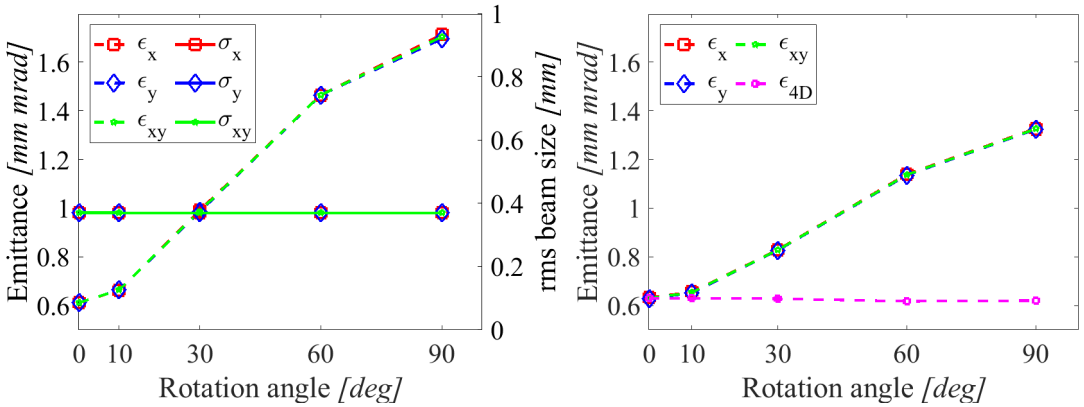

Figure 4.22: (left) Rms beam size and emittance calculated by slit scan (right) Emittance results by VPP, ϵ_{4D} remains almost constant.

Figure 4.23 shows the coupling factor t described in Eq. 4.26. When ϵ_{xy} and ϵ_{4D} are similar, the coupling factor value is around 0. The invariant depends upon the correlation term C_{xy}, therefore, as the correlation increases the invariant also

increases. Another interesting thing is to find coupling angle φ_{cal} using 4D TBM elements, see Eq. 4.28. It was found to be the same as the rotation angle θ, as expected. The correlation angle φ_{cor} found from the φ_{cal} shows that the correlation angle is maximum around 30°. Intuitively, one can say that it will increase till 45° and then start to decrease as the rotation angle approaches 90°.

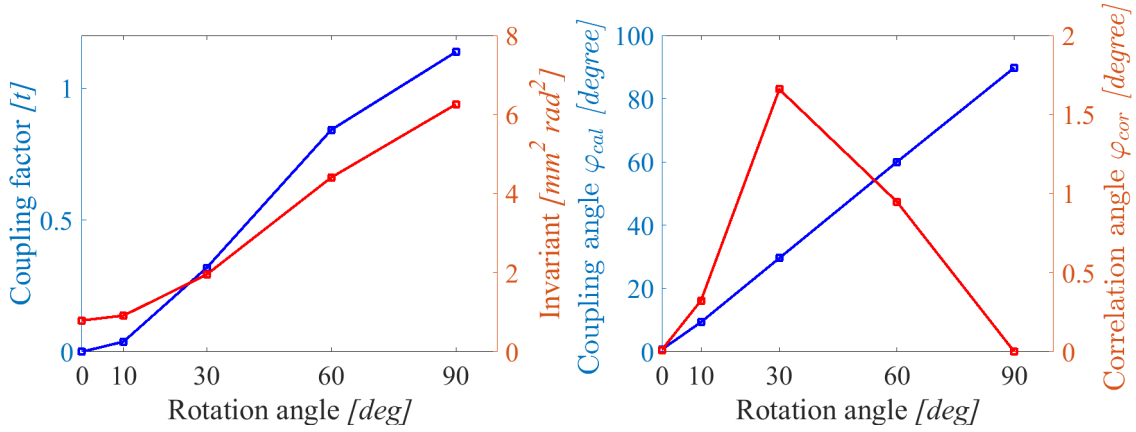

Figure 4.23: Introducing coupling in the beam increases the invariant, since it depends on the correlation between the transverse planes.

The 4D TPS of coupled beams is shown in Figure 4.24 to 4.26. The horizontal and vertical phase space results from the slit scan are compared with the VPP results. The overall phase space shape looks similar but if one compares the intensity distribution of the particles in the core and halo, it appears to be slightly different, because of different weighting of the beamlets. This is the reason for the difference in the emittance values between the slit scan and VPP, which was categorized as part of the systematic error.

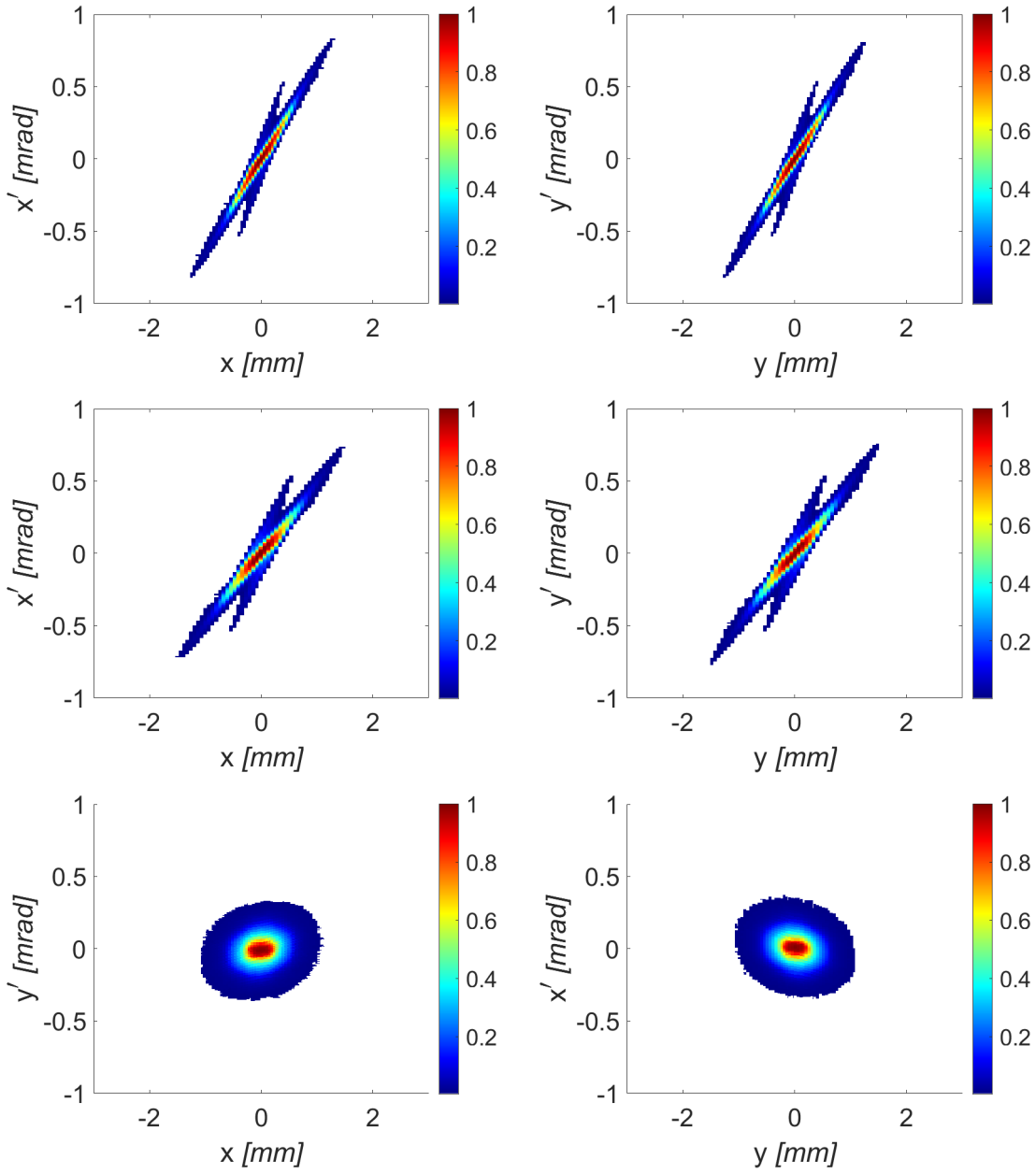

Figure 4.24: TPS of 10° coupled beam; first row shows the 2D slit scan phase space. Second and third rows show the 4D VPP phase space.

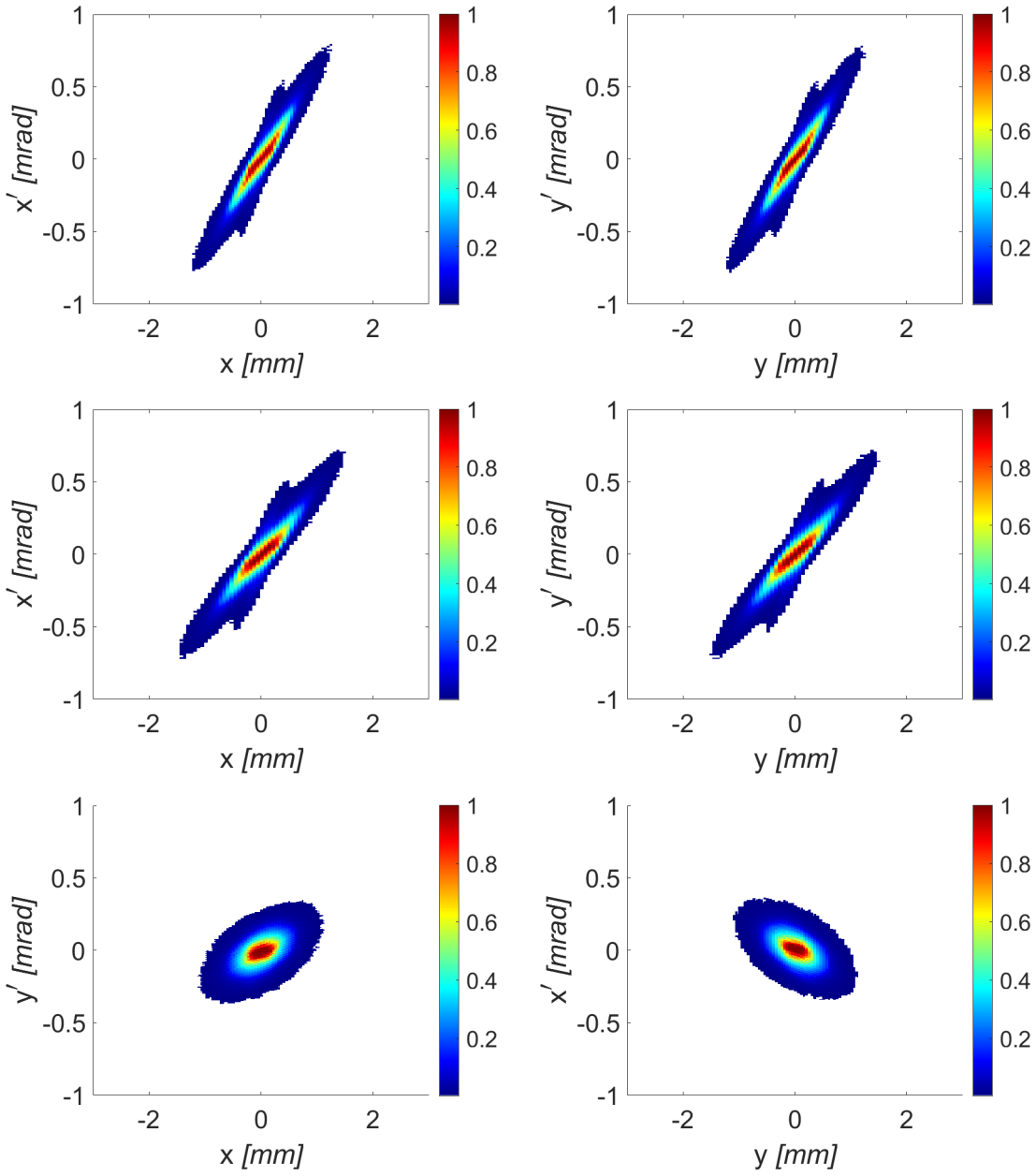

Figure 4.25: 30° coupled beam; first row shows the 2D slit scan phase space. Second and third rows show the 4D VPP phase space.

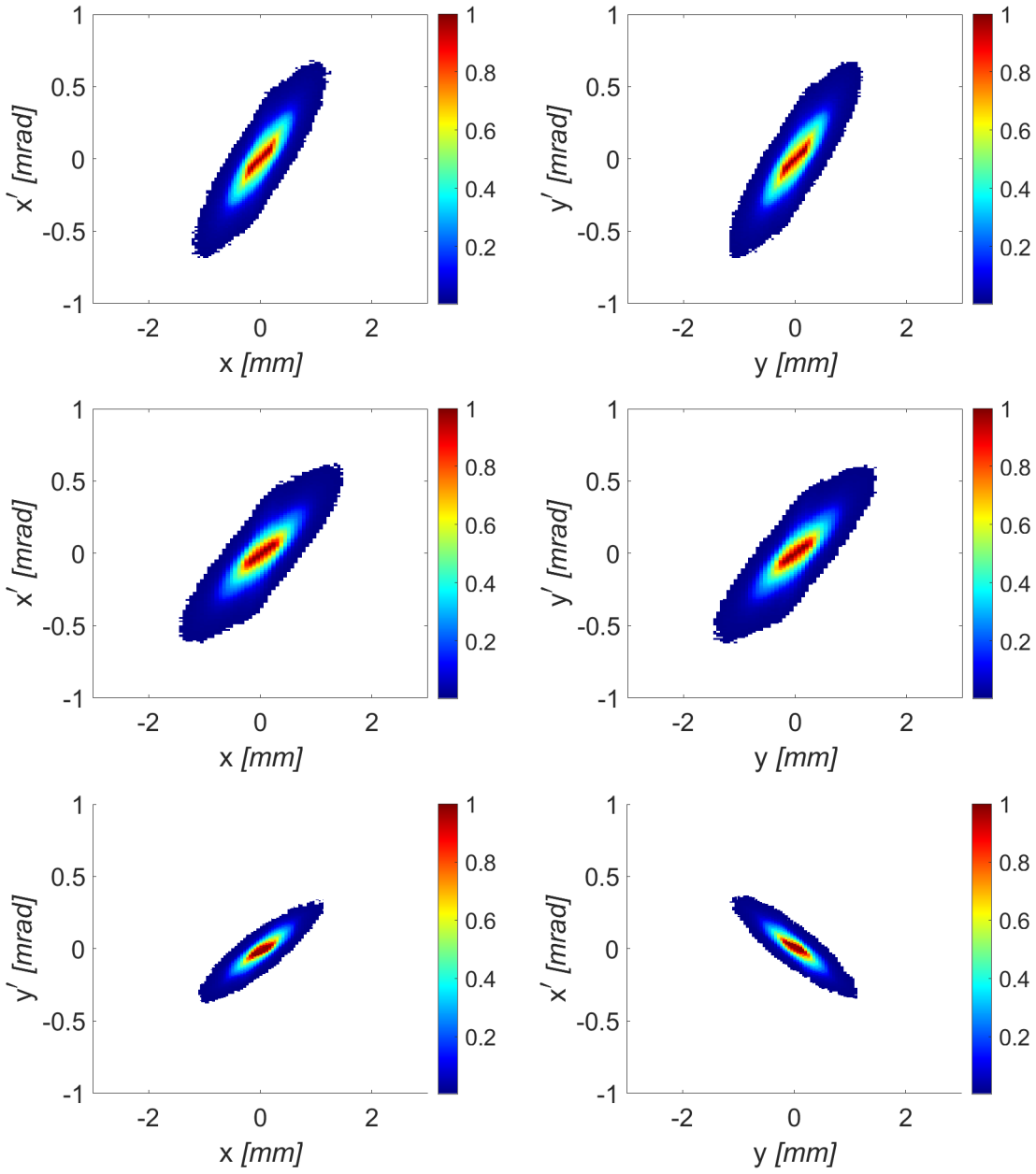

Figure 4.26: 60° coupled beam; first row shows the 2D slit scan phase space. Second and third rows show the 4D VPP phase space.

4.3.4 Slit scan charge cut

During the slit scan measurement, as the slit traverses the beam at the EMSY1 location, the beam halo intensity is comparable with the background noise level, and thus it cannot be correctly measured. This effect is referred as charge loss, as there is loss of information of non measureable particles. It is important to quantify this charge loss in order to know the true emittance values. Generally, when the beam at the EMSY1 screen location is chopped by a slit, the beamlet obtained on the MOI screen is diverged and therefore, has low intensity. To improve the signal strength, first the slit is positioned at the center of the beam and the corresponding beamlet at the MOI screen is observed. Then, to boost the signal, the number of electron bunches for the central beamlet is increased until the core of that beamlet reaches a certain intensity. This intensity threshold is defined by the saturation limit of the camera pixel intensity, which in our case is, 2000 counts per pixel (arbitary units). The slit scan in a particular direction (horizontal or vertical) is performed with this fixed number of bunches resulting in varying signal strength at the beamlet observation screen.

Let us discuss the case of a horizontal scan and the same would apply to the vertical case. Intuitively, one would say that when the slit is at the beginning or end of the beam distribution, generally known as halo part of the beam, the beamlets at MOI are either not visible or have poor strength due to the experimental noise diluting the signal. Although this is true, there is also halo part of the individual beamlets at MOI, that is diluted by the noise. When applying the noise filters, parts of the beamlets that are on the noise scale level, are filtered. Figure 4.27 shows beamlets from horizontal scan in case of no noise (left) and with noise and filter (right). The filter was applied after addition of background noisy frames from the experimental data. It is obvious by comparing these figures that the loss of charge is at the halo part of the beam in the scanning direction as well as also for the individual beamlets. For the purpose of illustrating this, only a few horizontal beamlets are shown.

To quantify this charge loss in the beam distribution, a methodology was defined and incorporated in the VPP algorithm. Basically, the charge loss was calculated by fitting the sum of pixels of beamlets as a function of the slit position to the EMSY1 beam distribution in an iterative manner. The initial values of these parameters

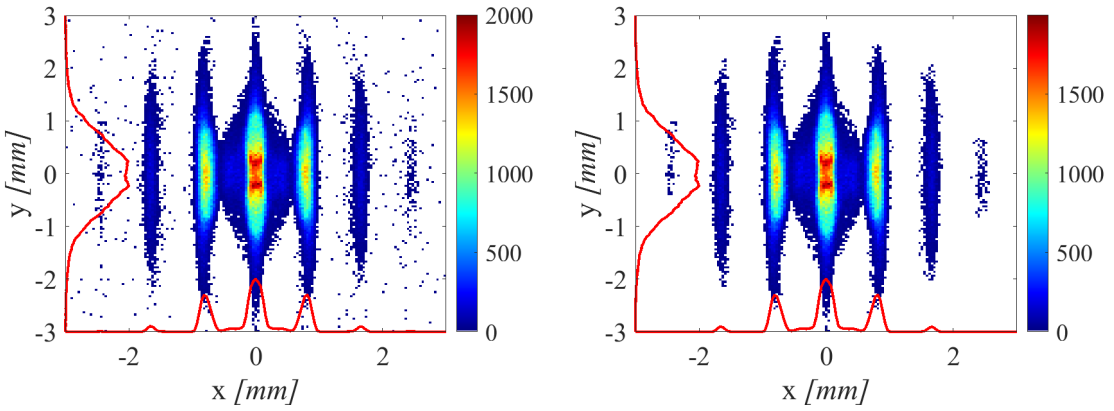

Figure 4.27: Horizontal beamlets; (left) without noise (right) with noise and filtering.

also influence the final charge cut numbers obtained after iterations. The three parameters used for fitting are described below:

- Intensity threshold (μ): EMSY image above a threshold μ is saved as $cutEMSY$ image.

$$cutEmsy = Emsy > \mu.$$

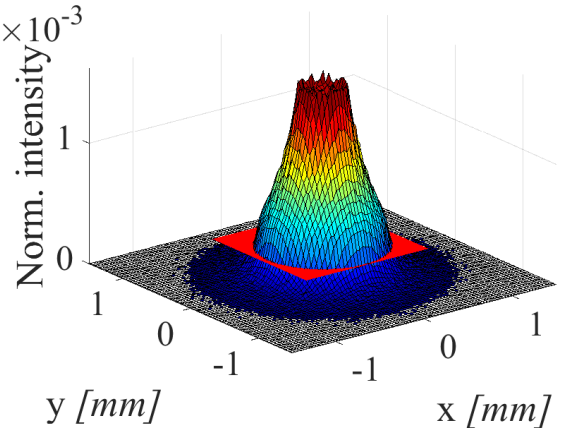

Figure 4.28: Beam distribution at EMSY1. The red plane shows the initial 2D intensity cut applied to the EMSY distribution.

- Position shifting (Δ): Projection of the cut EMSY image $ProjcutEmsy$ is

matched to the SoP of beamlets by shifting its position Δ.

$$SoPnewpos = SoP + \Delta.$$

- Scaling (A): SoP of beamlets is scaled to match $ProjcutEmsy$ such that the least square error η is minimum. The iterations are carried out until the convergence criteria is met, i.e., difference between successive iterations is $< 10^{-4}$. If the initial guess is closer to the solution, the results are achieved in a few iterations.

$$\eta(\mu, \Delta, A) = \sqrt{\sum (|ProjcutEmsy - A \times SoPnewpos|)^2}.$$

Hence, the EMSY beam image intensity was varied and the SoP of beamlets was scaled and shifted until the rms difference between the projection of the EMSY beam image and the soP of beamlets was minimized. The EMSY image above the final threshold μ is called *beam core* and the EMSY image below threshold μ that is lost is called *beam halo*. Charge cut is defined as ratio of SoP of beam halo to the SoP of beam distribution at slit location. After fitting SoP of noisy beamlets to EMSY distribution we obtain the core and halo as shown in Figure 4.29.

$$Charge\ cut = \frac{SoP\ of\ beam\ halo}{SoP\ of\ full\ beam}.$$

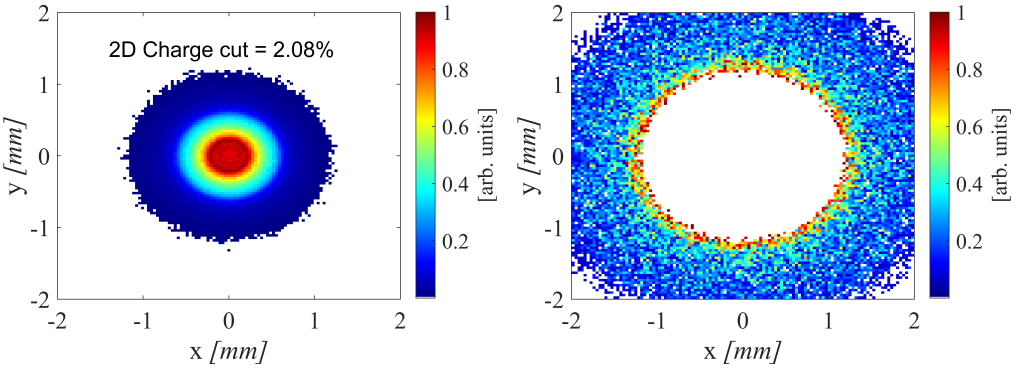

Figure 4.29: After charge cut, beam core (left) beam halo (right).

Basically in the VPP algorithm, before crossing the horizontal and vertical beamlets, they are normalized to the EMSY1 projection only after the charge cut has been applied.

One can again perform the charge cut on the phase space and then find the corresponding emittance values. Figure 4.30 shows the reduction in emittance values as the charge cut on the phase space increases. The results are shown for both slit scan and VPP based reconstructed phase space for four different solenoid current values, 365 A to 368 A, with the addition of noisy data. The noise was cleaned by applying SVD based filtering [63]. The results show that depending upon the beam distribution after noise filtering, the emittance values for the slit scan and VPP vary differently along the phase space charge cut.

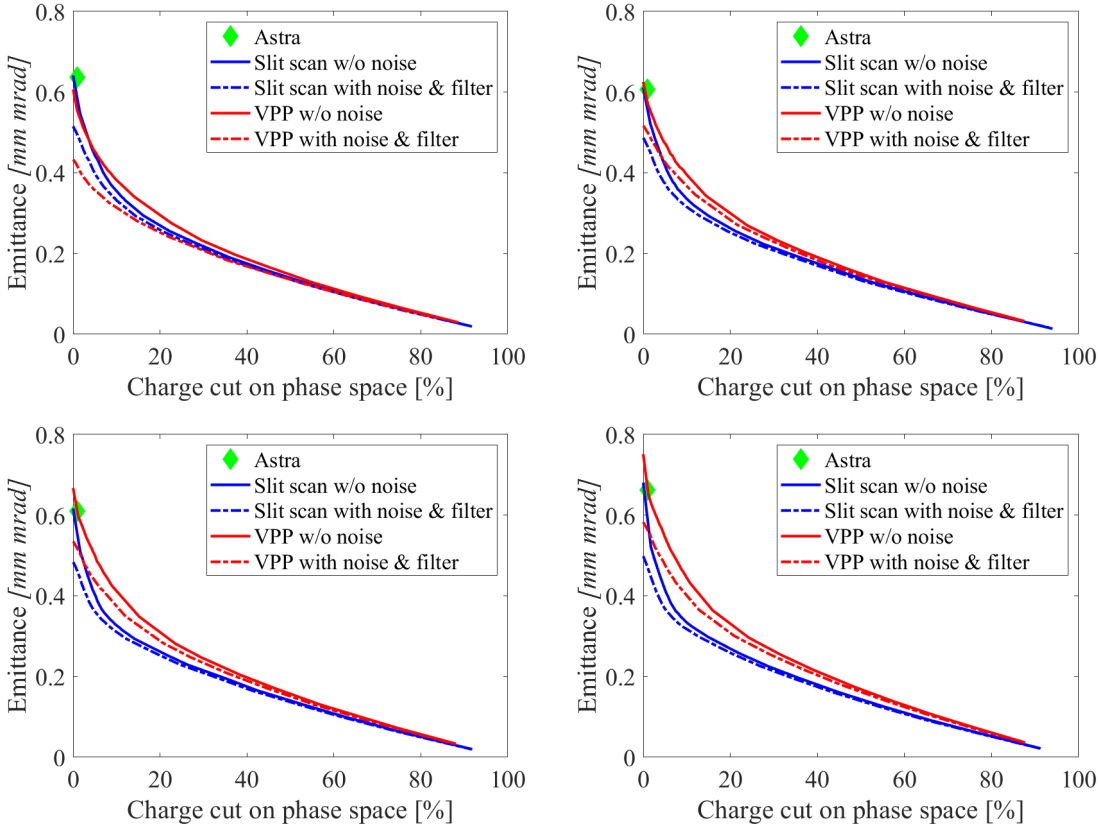

Figure 4.30: Results of the charge cut on phase space for beam distribution with solenoid currents (top left) 365 A (top right) 366 A (bottom left) 367 A (bottom right) 368 A.

4.4 Slit scan measurements for virtual pepper pot

The slit scan measurements are a pre-requisite for the Virtual Pepper Pot (VPP) technique. The machine is tuned to the desired beam parameters and the slit scan measurements are done. Generally, Gaussian laser distributions, both transverse and temporal, are used to generate electron beam at PITZ. The transverse laser profiles are shaped with a Beam Shaping Aperture (BSA) by cutting out the central part of the Gaussian distribution to obtain a quasi-uniform distribution. The transverse laser profile is measured by a CCD camera at a 1:1 imaging plane of the cathode (called the virtual cathode). The BSA is imaged onto the cathode to emit the photoelectrons. Figure 4.31 shows a typical transverse laser profile of 1 mm diameter BSA used to optimise the emittance of a 250 pC beam. The measurement shows an rms sizes of $\sigma_x = 0.249$ mm and $\sigma_y = 0.259$ mm for horizontal and vertical projections, respectively.

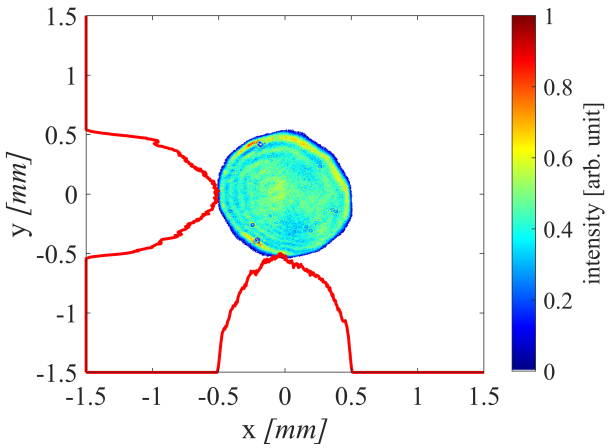

Figure 4.31: Beam on virtual cathode for BSA = 1.0 mm.

For a typical slit scan measurement at PITZ, the power in the gun cavity is set to achieve a beam momentum of 6.3 MeV/c, which is very close to the gun operation point at the Eu-XFEL [11]. The gun cavity is operated at the maximum acceleration phase. The booster cavity is operated at on-crest, yielding a mean momentum of the electron beam around 19.4 MeV/c. The electron beam alignment with the gun cavity, the solenoid magnet, and the booster cavity is optimised using beam-based procedures [64]. This reduces the beam transverse and longitudinal coupling due

to dipole kicks in RF and solenoid magnet, minimising the transverse emittance growth. After the laser and electron beam alignment, the electron beam asymmetry is removed by gun quadrupole magnets inside the solenoid [65] and the electron beam trajectory tuning in the low energy section as well as through the booster. Generally, the gun quadrupole strength settings are iterated by an optimizer until the transverse beam profile after the booster, at the slit location, minimises the xy correlation and the difference in the horizontal and vertical rms beam size. Although the beam is made symmetric at the location of the slit, it is still asymmetric at the other screens after the booster, which is a signature of remaining or newly introduced coupling. This implies that the beam divergence and correlations are different in both transverse planes resulting in asymmetric emittances. Therefore, VPP is required to perform 4D diagnostics to understand the coupling in the transverse planes and improve the emittance.

4.4.1 Solenoid current scan

Once the beam is transported to the slit station, its horizontal and vertical phase space can be measured. In order to find the beam transport that corresponds to the minimum emittance, the main solenoid current is varied around the minimum beam rms size at the slit location. The bucking solenoid current is automatically tuned to compensate the magnetic field at the photocathode. Basically, changing the main solenoid current aligns the phase ellipses within the phase space and results in reduction in emittance [20]. First, the horizontal slit scan is done to find the horizontal emittance for a set of different solenoid current values. This is followed by a vertical slit scan. Finally, the solenoid current is set to the value that yields minimum of $\epsilon_{xy} = \sqrt{\epsilon_x \cdot \epsilon_y}$. In order to estimate the statistical error of the minimum emittance point, the measurement is repeated three times.
In this case, the solenoid current was varied from 366 A to 371 A with a step of 1 A and the horizontal and vertical slit scans were performed for each case. The number of pulses were adjusted for each scan in order to have the peak pixel intensity around 2000 for the central beamlet. The start and end position of the slit for each scan was set by the visual inspection of the beamlet at the beamlet collector screen. The beam distribution for different solenoid currents is shown in Figure 4.32.

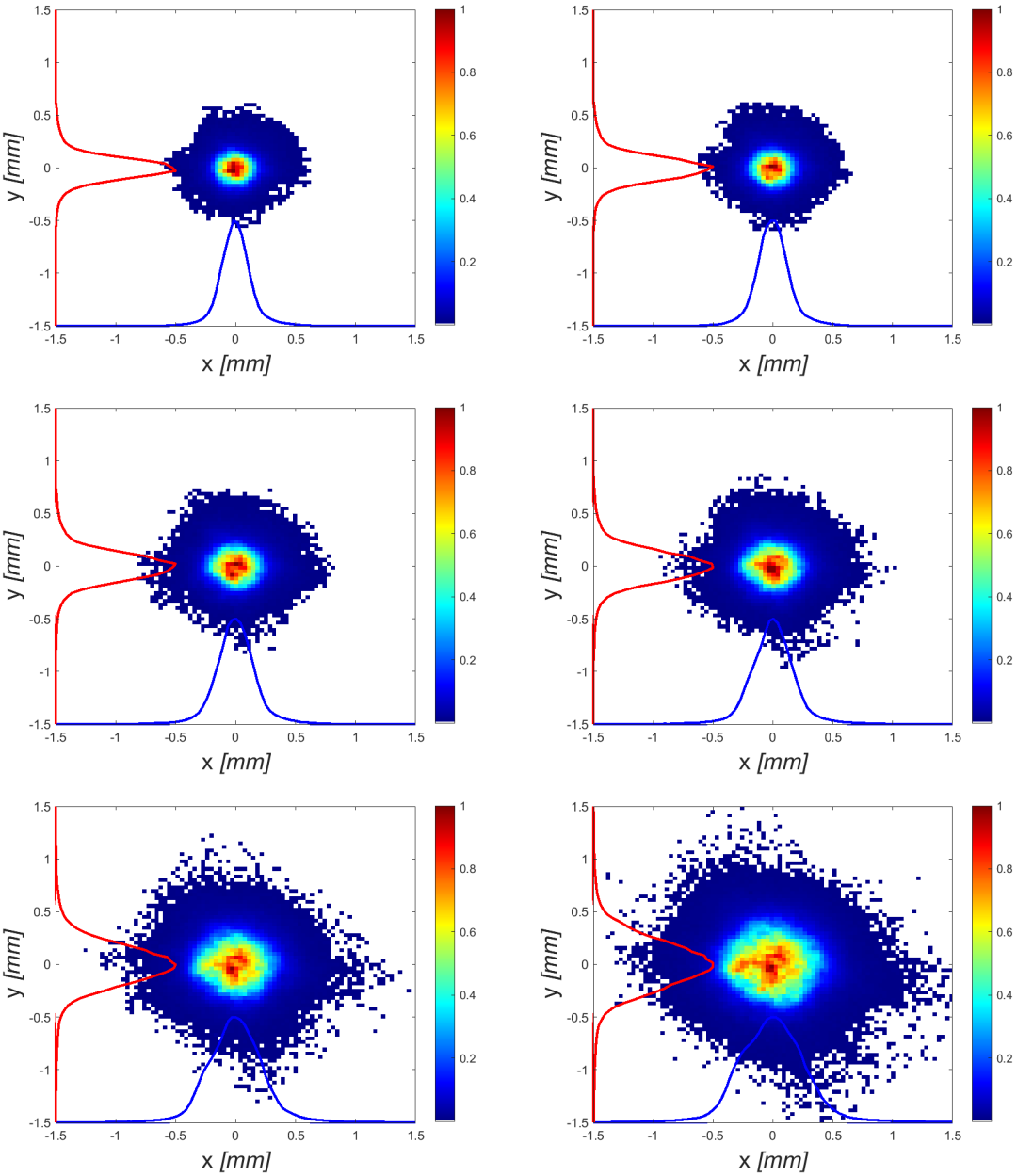

Figure 4.32: Beam distribution at YAG screen on EMSY1 station for various solenoid currents; (top left) 366 A (top right) 367 A (middle left) 368 A (middle right) 369 A (bottom left) 370 A (bottom right) 371 A.

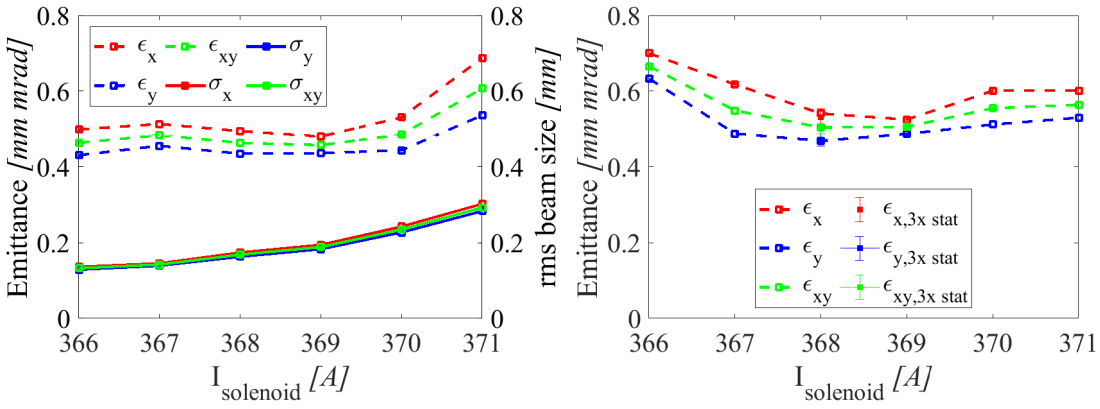

Figure 4.33: Results obtained with slit scan for solenoid current scan (left) Unscaled emittance and rms beam sizes (right) Scaled emittance.

Figure 4.33 (left) shows the rms beam size and the emittance results obtained from the slit scan methodology. It was observed that as the rms beam size increases, the emittance values also increases, but these are unscaled emittance numbers. Figure 4.33 (right) shows the scaled emittance values where the scaling factor is calculated from the Eq. 4.3. Here the emittance values are higher at the start, decrease in the center and then start to increase again. This is because the scaling factor was high (implying more charge cut) for a strongly focused beam that has a small beam core and a relatively large halo. Figure 4.34 (left) shows the results of VPP for the solenoid scan. The trend of the emittance curve for the unscaled slit scan and the virtual pepper pot is the same but the values are different. This is because of the 2D charge cut applied in the VPP methodology. Also, it is worth noting that the ϵ_{4D} and ϵ_{xy} estimated by VPP are almost equivalent. This implies that there is no significant coupling in the beam introduced by varying the solenoid current. Figure 4.34 (right) shows the charge loss estimated for the VPP beamlets corresponding to the different beam distributions during the solenoid scan. When the beam is more focused, there is higher charge cut. This is because the density of the beam distribution in the halo of the whole beam as well as in the halo of the individual beamlets is lower and is therefore, diluted by noise and consequently filtered. As the beam size increases and the distribution transients smoothly from core to halo, the charge cut also decreases.

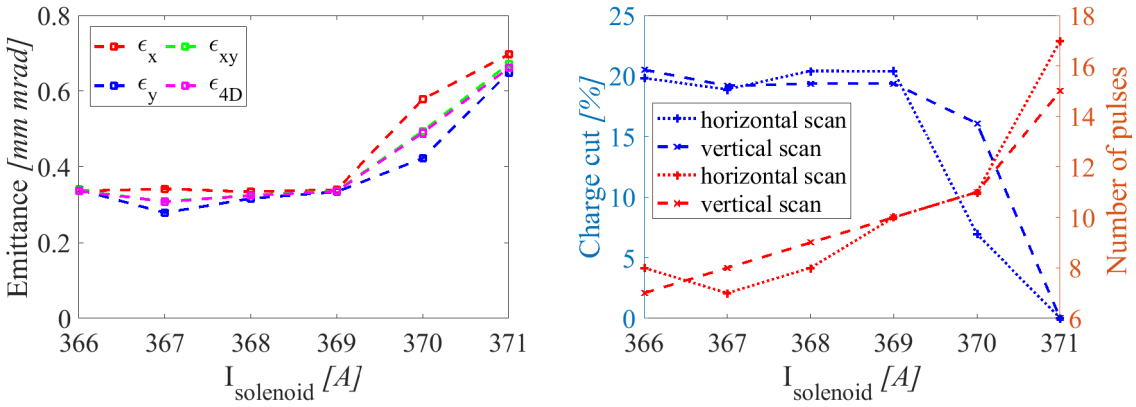

Figure 4.34: (left) Emittance results using VPP (right) Charge cut after fitting sum of pixels of beamlets to the beam distribution as a function of the slit location.

The VPP technique was used to reconstruct the 4D phase space for the beam corresponding to the different solenoid currents. Figure 4.36, 4.37, 4.38 and 4.39 show the reconstructed 4D phase space for 366 A, 368 A, 369 A and 371 A respectively. For each case, the first row corresponds to the phase space reconstructed using the slit scan. The horizontal phase space (x, x') is reconstructed by plotting the x projections of the beamlets against the slit positions, where the y scale is calibrated in terms of divergence according to equation 4.2. The vertical phase space (y, y') is reconstructed by plotting the y projections of the beamlets in a similar fashion. The second row corresponds to the phase space reconstructed from the horizontal and vertical beamlets generated by adding up of VPP beamlets. It is evident that the halo part of the beam is reduced since the VPP beamlets are only constructed from the common portion between the horizontal and the vertical beamlets obtained from the slit scan. The overall structure of the core part remains the same but the intensity is higher as seen from the colormap. This is because of the foreign particles that emerged from the slit area adjacent to pepper-pot-like hole in the VPP mask and is part of the VPP beamlets. From the simulations we know that the foreign particles cause a systematic error of almost 2 % for the minimum emittance case.
The third and fourth row show the 4D TPS reconstructed from the VPP technique. As the VPP beamlets are reconstructed after applying the 2D charge cut, one can see the halo missing in the reconstructed phase space. The iterative procedure of the charge cut is also dependent on the initial values and therefore, may underestimate

or overestimate the charge cut by $\leq 4\,\%$. Figure 4.36 shows the case where part of the beam core is removed during 2D charge cut (strongly focused beam case) where as, figure 4.39 shows no charge cut and the whole beam contributes to the 4D phase space reconstruction (relaxed focusing case). The VPP beamlets correspond not only to each slit position but also the intermediate points obtained by calculating the center of mass of individual beamlets. Therefore, the phase space is interpolated at those points to give a smooth continuous profile. The cross plane coupling can be investigated by the transverse plane phase space. The reconstruction results show that the (x, y') phase space ellipse remains upright for all the solenoid currents and the halo part of the beam is increased as the solenoid current is varied and the beam distribution becomes larger. The (y, x') phase space shows positive correlation, and as the solenoid current is increased and the beam becomes larger, the correlation also increases. Since the correlation in transverse plane is detected by 4D diagnostics, one can remove it to optimize the emittance.
Figure 4.35 shows the trend of the coupling factor and the Invariant. Both of them remain almost constant from 366 A to 369 A and then increase by a factor of two for 370 A and by a factor of four for 371 A. The 4D phase space reconstruction shows that the coupling in (y, x') increases which causes increase in ϵ_{xy} and ϵ_{4D}.

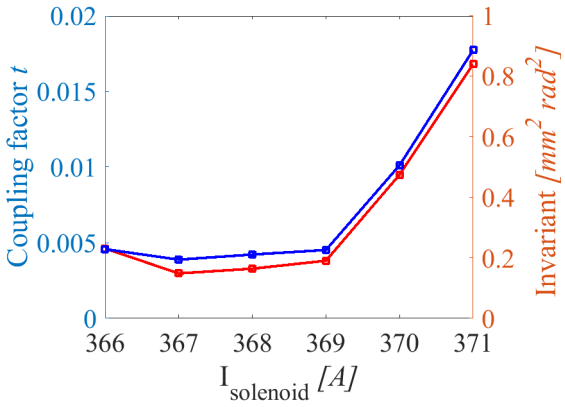

Figure 4.35: Coupling factor and invariant.

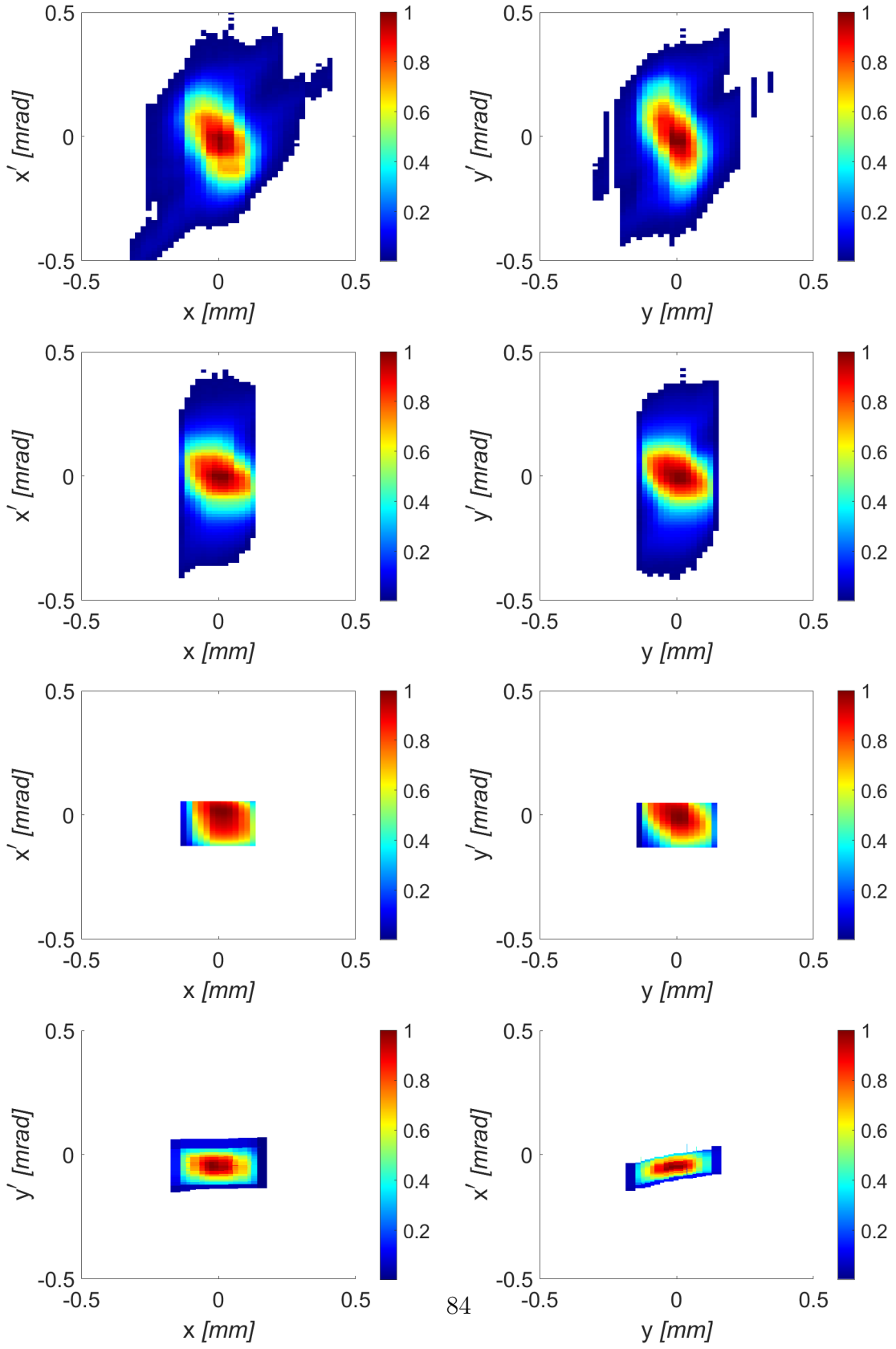

Figure 4.36: Phase space reconstructed for $I_{solenoid}$ =366 A from: Slit scan (1^{st} row); Slit scan generated by VPP (2^{nd} row); 4D TPS by VPP (3^{rd} and 4^{th} row).

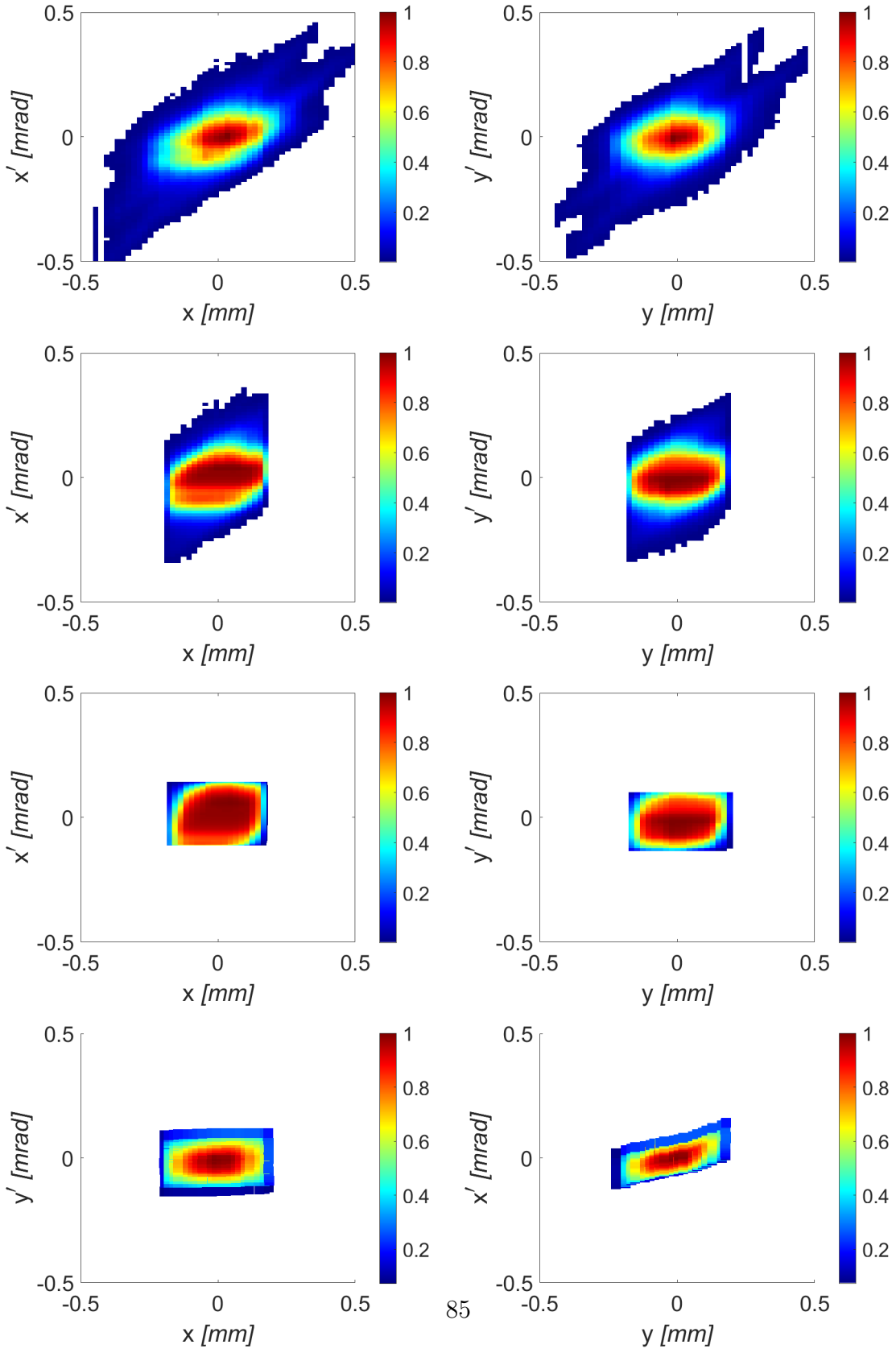

Figure 4.37: Phase space reconstructed for $I_{solenoid}$ =368 A from : Slit scan (1^{st} row); Slit scan generated by VPP (2^{nd} row); 4D TPS by VPP (3^{rd} and 4^{th} row).

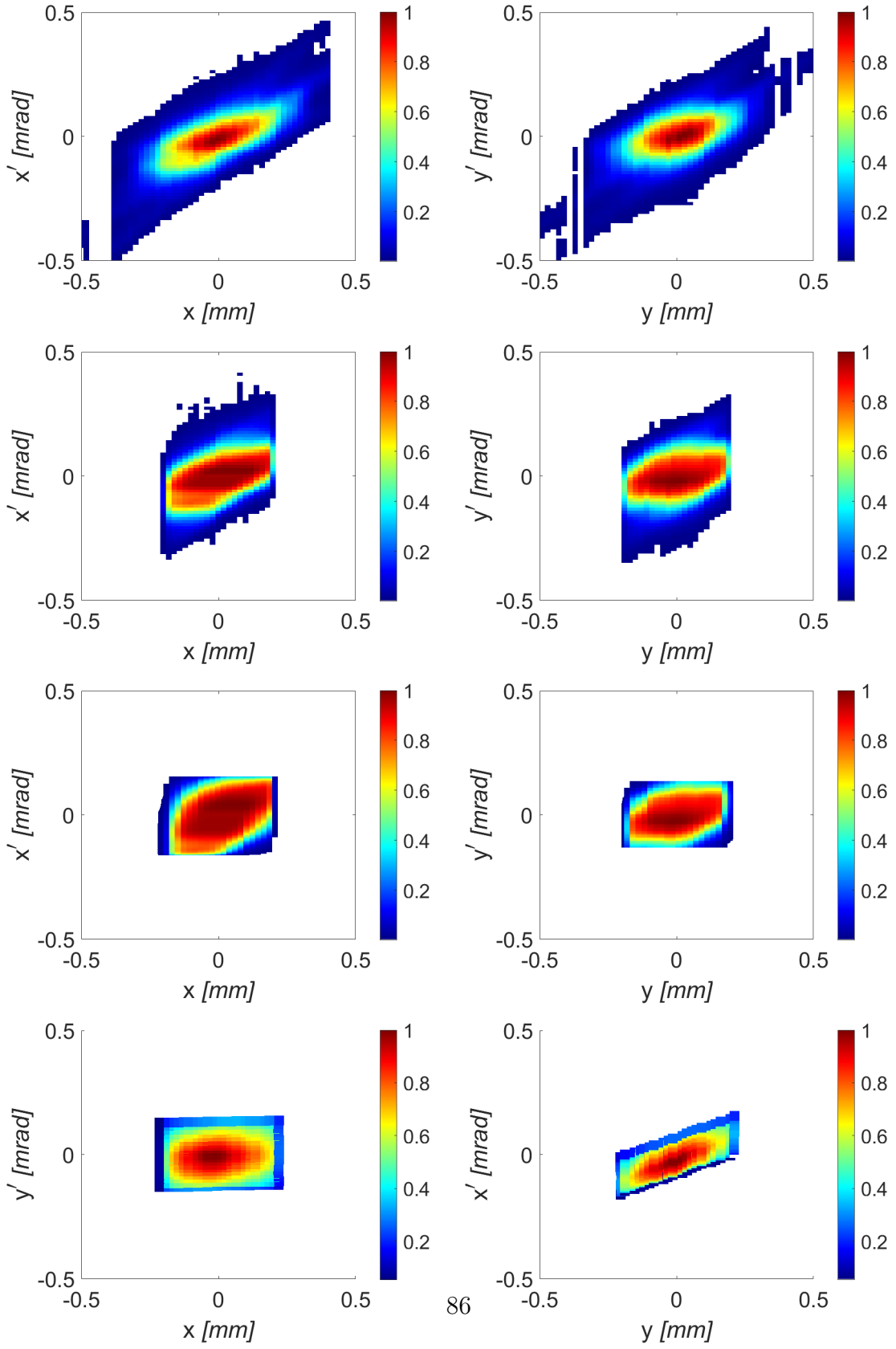

Figure 4.38: Phase space reconstructed for $I_{solenoid}$ =369 A from : Slit scan (1^{st} row); Slit scan generated by VPP (2^{nd} row); 4D TPS by VPP (3^{rd} and 4^{th} row).

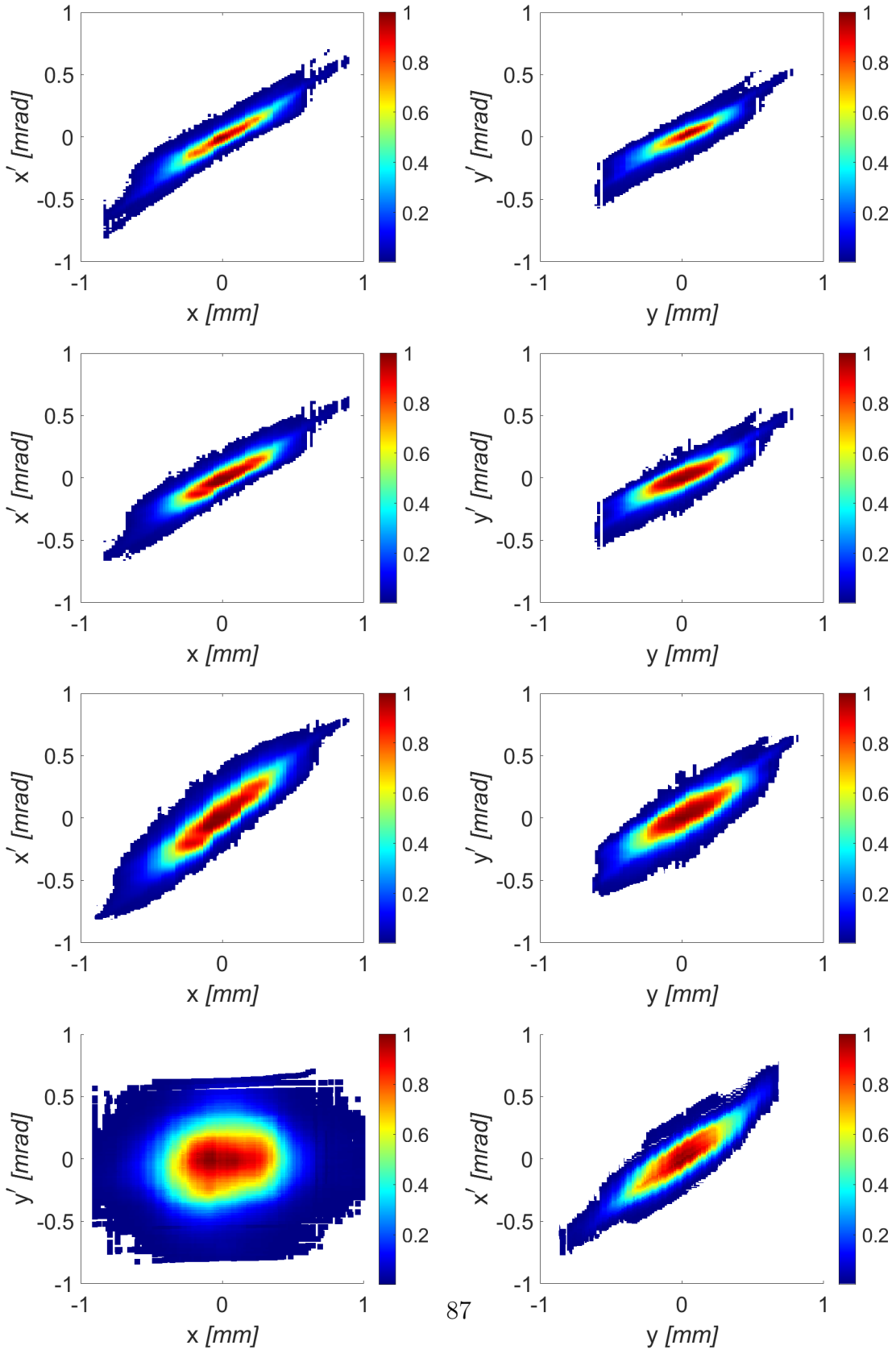

Figure 4.39: Phase space reconstructed for $I_{solenoid}$ =371 A from : Slit scan (1^{st} row); Slit scan generated by VPP (2^{nd} row); 4D TPS by VPP (3^{rd} and 4^{th} row).

4.4.2 Asymmetric and coupled beams

If the gun quadrupoles are not used, the beam distribution is naturally asymmetric with spike-type structure at two opposite ends. A typical electron beam distribution measured at the slit location with YAG screen is shown in Figure 4.40. The origin of this electron beam asymmetry was traced back to multipole kicks in the gun section, namely around the location of the coaxial power coupler and the main solenoid [52]. Additional studies were performed in order to characterize this source considering RF gun power coupler [66] and main solenoid abberations due to anomalous quadrupole fields [67].

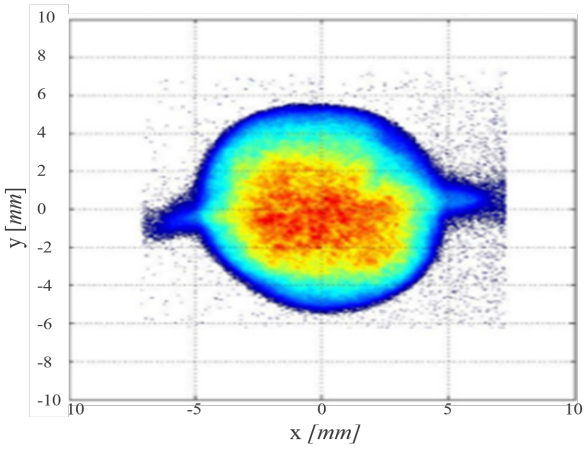

Figure 4.40: Beam distribution at the slit location for solenoid current 360 A [67].

In order to compensate the assumed kick integrally by a static quadrupole field, a pair of quadrupoles were designed, a normal and a skew, on the same frame but connected to two independent power supplies, see Figure 4.41. Such a combination enables virtual rotation of the quadrupole field.
This feature of the gun quadrupoles was exploited to test the virtual pepper pot technique. The solenoid current (368 A) corresponding to the minimum emittance value was set, and slit scan data was generated with coupling intentionally introduced in the beam in the transverse plane. A combination of normal and skew quadrupole currents was kept such that the amplitude I_o was constant but the angle Φ was varied. Eq. 4.33 shows the relation between the current and the angle of

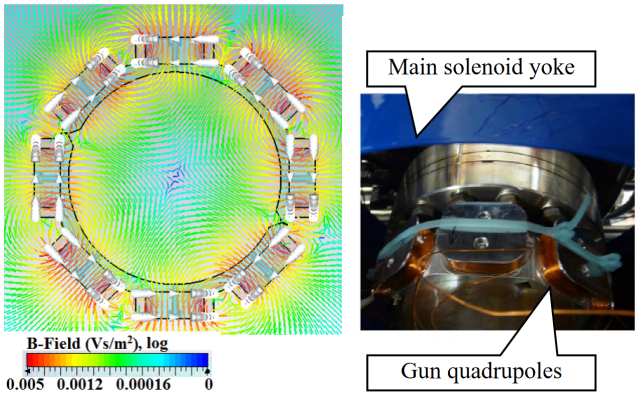

Figure 4.41: Gun quadrupoles consisting of two air quadrupole coils; normal and skew. (left) magnetic field simulated with CST EM Studio for $I_{q,norm} = -0.5\,\mathrm{A}$ and $I_{q,skew} = -0.6\,\mathrm{A}$; (right) photo of the quadrupole installed in the PITZ injector [65].

the normal and skew quadrupole.

$$\begin{aligned} I_{q,norm} &= I_o \cos\Phi, \\ I_{q,skew} &= I_o \sin\Phi. \end{aligned} \tag{4.33}$$

The rotation angle Φ of the gun quadrupoles was varied from 0° to 90° with a step size of 10°. Figure 4.42 shows the coupled beam distribution at the location of the slit. The beam's spatial distribution becomes larger and asymmetric as the quadrupole rotation angle Φ is increased. The rms size increases more in y as compared to x as the beam forms a diamond-like shape. The core of the beam shifts towards the left where as the hallow part moves clockwise until 50°. From 60° to 90°, the beam halo starts to move counter clockwise and the core becomes upright but with nonsymmetric intensity distribution. The horizontal and vertical slit scan data was generated for each of these 10 cases three times for the statistics.

The beam rotation by the variation of the gun quadrupoles' angle Φ results in the effective rotation of the 4D transverse phase space. The exact numbers of emittance and other beam parameters are very sensitive to the beam distribution. The charge cut due to the background noise causes $\leq 20\,\%$ loss of signal and hence phase space points to be reconstructed. The foreign particles influence the weighting of VPP beamlets by $\leq 20\,\%$, depending upon the coupling angle . All these factors pose

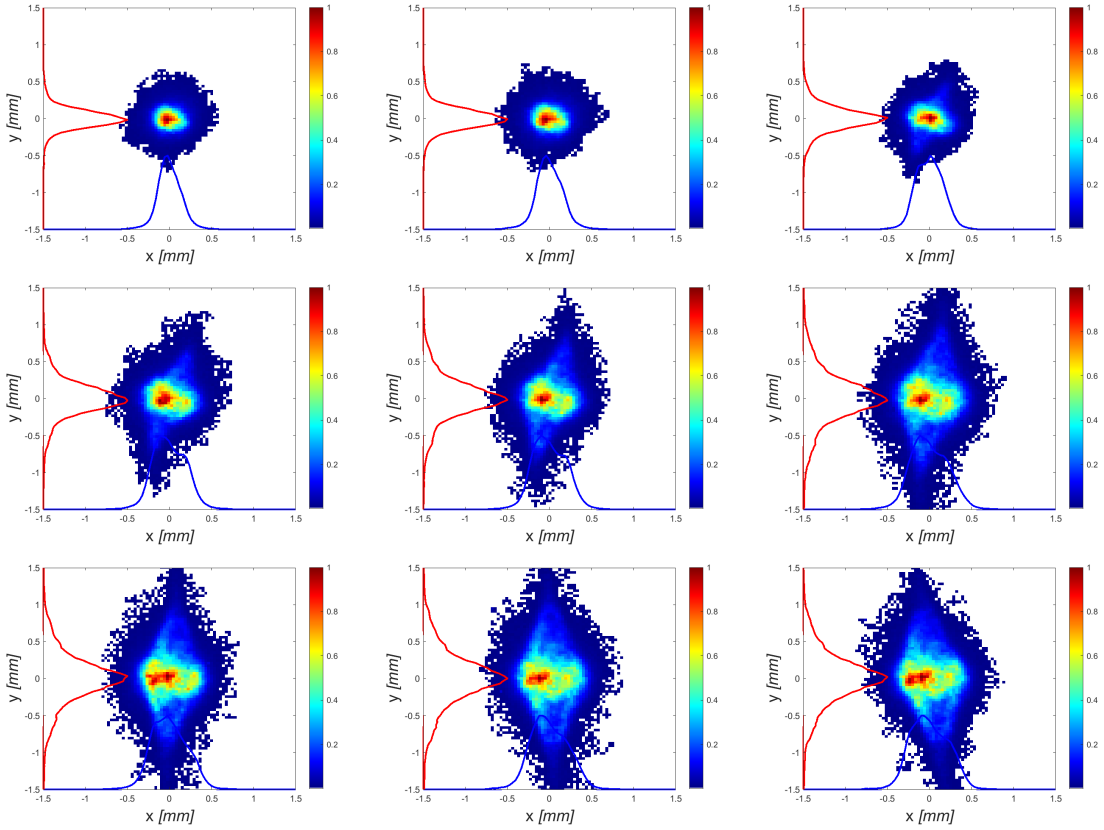

Figure 4.42: Beam distribution as a result of varying the quadrupole rotation angle, (top row, left to right) 10°, 20°, 30° (middle row, left to right) 40°, 50°, 60° (bottom row, left to right) 70°, 80°, 90°.

a challenge to characterize the 4D phase space. Figure 4.43 (left) shows the rms beam size and the emittance results for VPP. The overall trend is increasing as the quadrupole rotation angle is increased, but the minimum ϵ_{xy} and ϵ_{4D} is obtained for Φ =10°. Between 30° and 60°, ϵ_{4D} is less than ϵ_{xy}, indicating more coupling for this range. Afterwards, their emittance curves again coincide and show an increasing trend. Hence, it was found that fine tuning the quadrupole rotation angle gave minimum emittance at 10°. Figure 4.43 (right) shows the charge cut and number of pulses for both horizontal and vertical scan. The charge cut decreases from around 20 % to 10 % as the beam size increases. Also, the number of pulses during the horizontal scan increase from 30° rotation angle as the y rms beam size starts to increase.

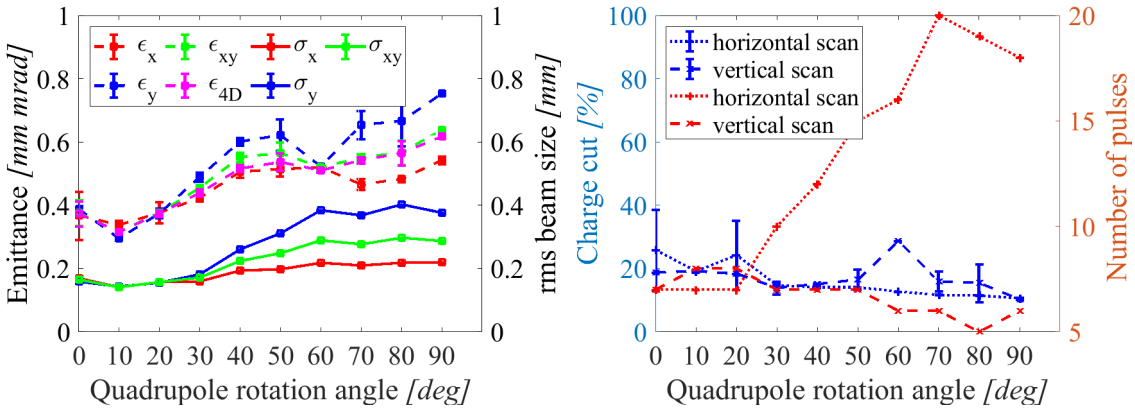

Figure 4.43: (left) Emittance results from VPP for the quadrupole rotation angle scan (right) Charge cut calculated and number of pulses used for each case.

Figure 4.44 (left) shows the coupling factor and the beam invariant. The coupling factor is maximum for the quadrupole rotation angle 40°, since the difference between ϵ_{xy} and ϵ_{4D} was maximum for this case. It is minimum for two rotation angles, 10° and 80° since the difference between ϵ_{xy} and ϵ_{4D} was around 0 for these two case. The invariant depends upon ϵ_x, ϵ_y and C_{xy} and shows overall an increasing trend but it is minimum for 10° rotation angle. Figure 4.44 (right) shows the coupling angle and the correlation angle. The coupling angle φ_{cal} that depends on the correlation terms is around 0 for both 10° and 80°. But the correlation angle φ_{cor} that depends upon φ_{cal} as well as divergence is only around 0 near $\Phi = 10°$. At $\Phi = 80°$, $\varphi_{cal} = -30°$. Thus for quadrupole rotation angle 10° corresponding to the minimum emittance point, the coupling angle and correlation angle both are around 0.

4D phase space reconstruction using VPP is shown for 10°, 30°, 40°, 60° and 90° in Figure 4.45, 4.46, 4.47, 4.48 and 4.49, respectively. It was observed from the investigation of the 4D phase space that for the case of 10° quadrupole rotation angle, the horizontal and vertical phase spaces have small beam size and low divergence and the cross plane phase spaces show that the (y, x') phase space is upright and the (x, y') phase space has a slight positive correlation.

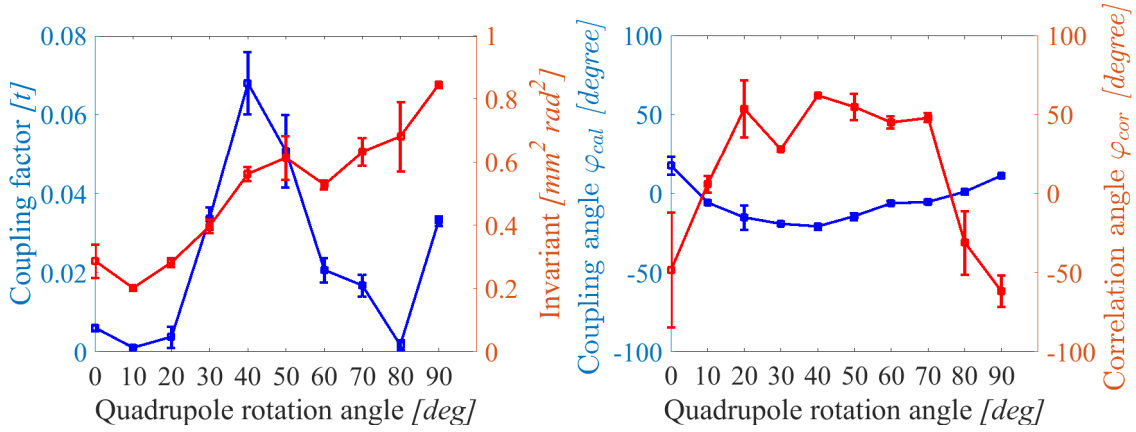

Figure 4.44: (left) Coupling factor and invariant (right) Coupling angle and correlation angle, both are around 0 for quarupole rotation angle 10°

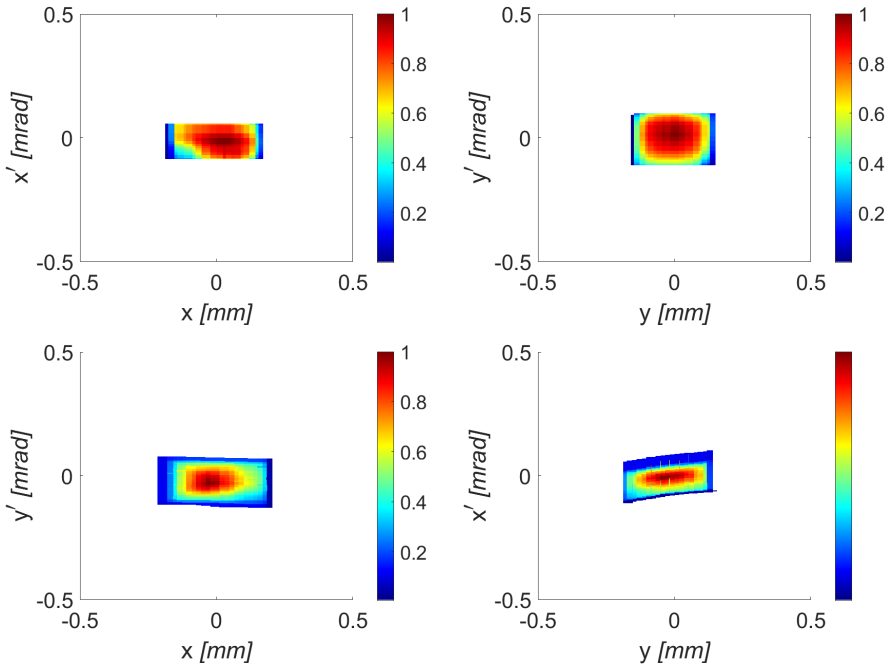

Figure 4.45: 4D TPS reconstructed using VPP for quadrupole rotation angle 10°.

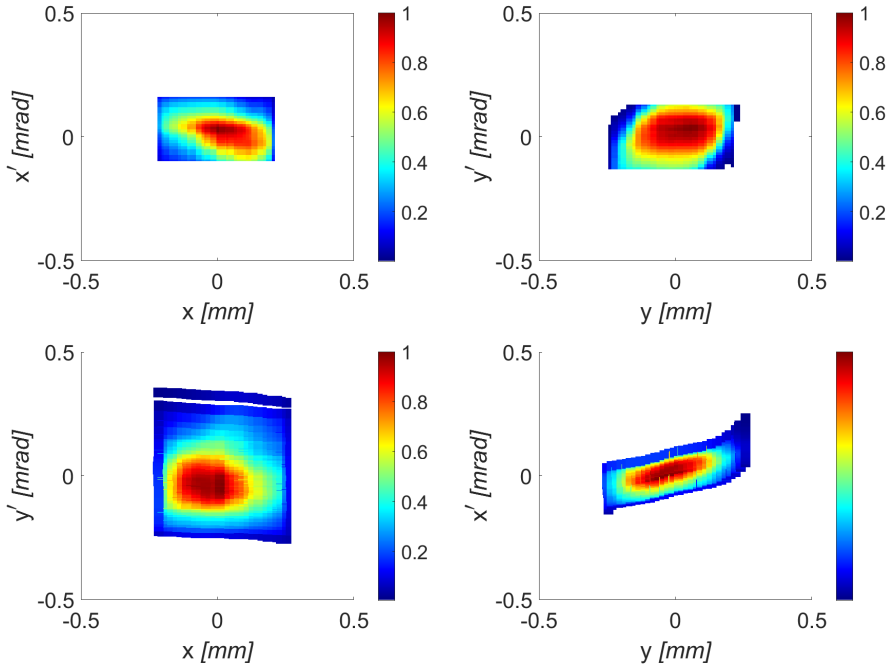

Figure 4.46: 4D TPS reconstructed using VPP for quadrupole rotation angle 30°.

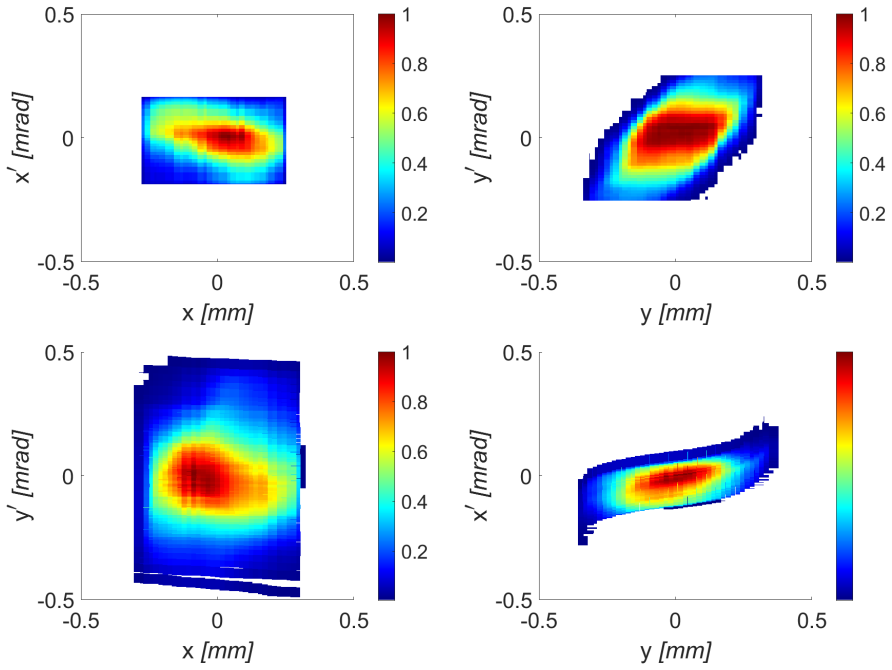

Figure 4.47: 4D TPS reconstructed using VPP for quadrupole rotation angle 40°.

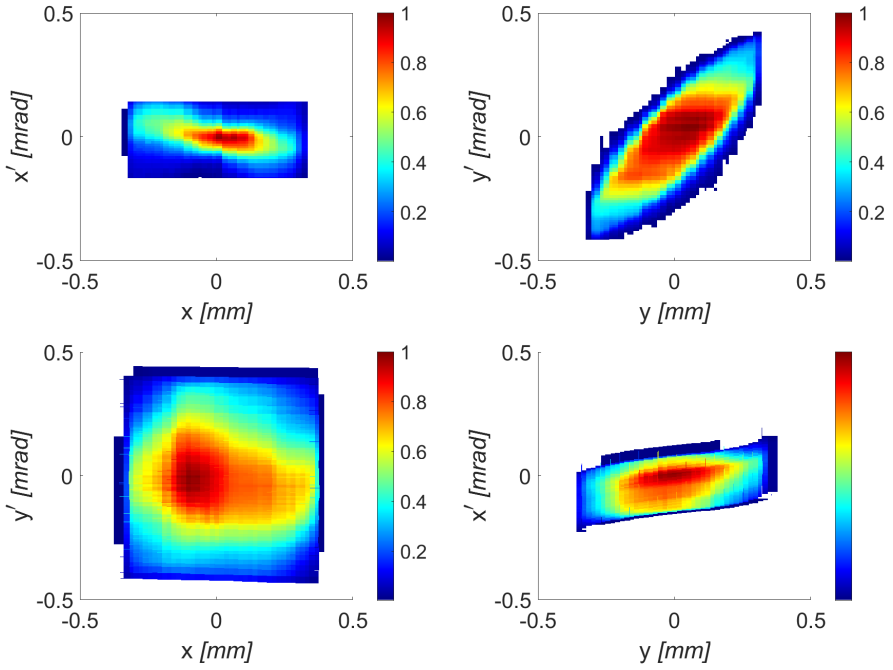

Figure 4.48: 4D TPS reconstructed using VPP for quadrupole rotation angle 60°.

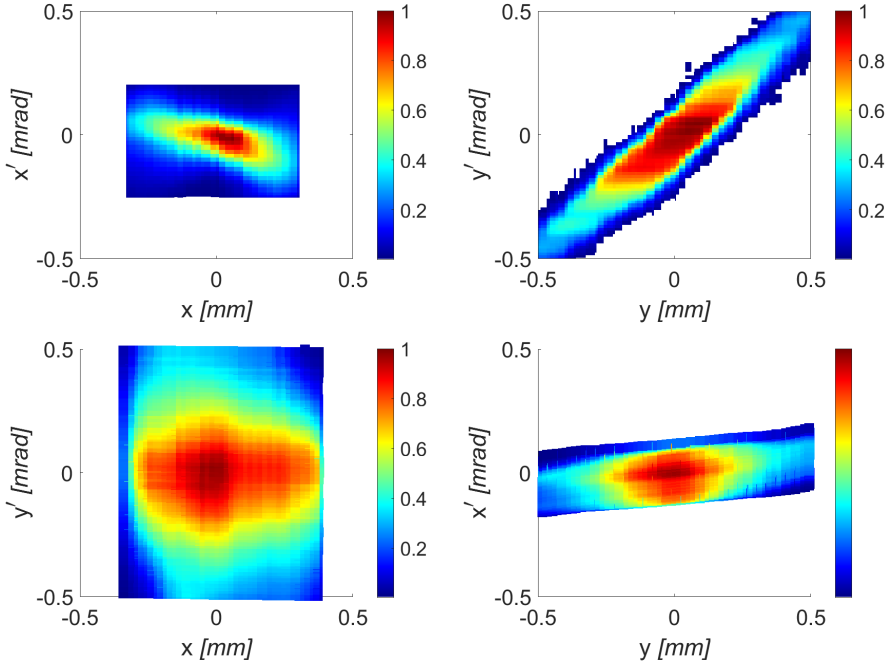

Figure 4.49: 4D TPS reconstructed using VPP for quadrupole rotation angle 90°.

4.5 Summary

PITZ utilizes slit scan technique as a standard tool for reconstruction of the horizontal and vertical phase spaces of space charge dominated electron beams. A novel method for 4-dimensional transverse phase space characterization, known as Virtual Pepper Pot, is proposed at PITZ, that can give insight to transverse beam phase space coupling. It utilizes the horizontal and vertical single slit scans to form pepper pot-like beamlets by careful crossing and post-processing of the slit scan data. All the elements of the 4D transverse beam matrix are calculated and used to obtain the 4D transverse emittance and coupling factor.

In this chapter, first an analytical model was developed to construct the elements of the 4D beam matrix. Then the proof-of-principle simulations were carried out to demonstrate the diagnostic capability of the VPP for both uncoupled and coupled beams. The systematic error was quantified to explore the effect of *foreign particles*. The number of horizontal and vertical slits to be crossed were discussed to optimize the results and computation effort. Then the proposed technique was applied to the experimental slit scan data. The loss of the charge in the beamlets due to low signal to-noise (SNR) ratio was considered in the algorithm as a signal cut, since it is important to consider the signal that actually contributed to the beamlets. The results gave 4D emittance, coupling factor and insight to cross planar coupling with its 4D phase space reconstruction.

Hence, VPP enabled 4D transverse phase space characterization of 250 pC beam with typical XFEL parameters. The minimum emittance estimated by the slit scan during the solenoid current scan can be further reduced if one can quantify the cross planar coupling using VPP. By fine tuning the quadrupoles' current amplitude and angle, one can remove or minimize the correlations in 4D transverse phase space.

Chapter 5

Longitudinal phase space characterization via tomography

Longitudinal phase space $(z, \delta p_z)$ characterization of an electron beam in accelerators is possible by deflecting the beam using a transverse deflecting structure to resolve the temporal profile and then using a dipole to resolve the beam momentum. Alternatively, it can be characterized without this specialized setup using the well-known method of tomography. This chapter gives a brief overview of tomography and highlights key challenges for Longitudinal Phase Space (LPS) tomography at PITZ, posed by low energy as well as high charge beams. An analytical model of LPS will be developed without taking the space charge effects into consideration. The proof of principle simulation for LPS tomography will be shown for a 250pC beam without SC and with SC (special settings needed for SC). The reconstruction method used and the improvement in the method will also be discussed. The experimental results for different cases of charge and temporal laser profiles will be shown to demonstrate the diagnostic capability.

5.1 Introduction to tomography

A variety of techniques have been developed to reconstruct higher dimensional distributions from lower dimensional projections, commonly known as tomography [68]. It involves an image (object representation) reconstruction technique that utilizes projections of the object from different viewing angles and then uses iterative equation

solving methods to reconstruct the object. Figure 5.1 shows a schematic example of taking a one-dimensional projection from a two-dimensional unknown object. Tomography is used in medicine [69], archaeology, biology, geophysics, oceanography, materials science, astrophysics, and other sciences.

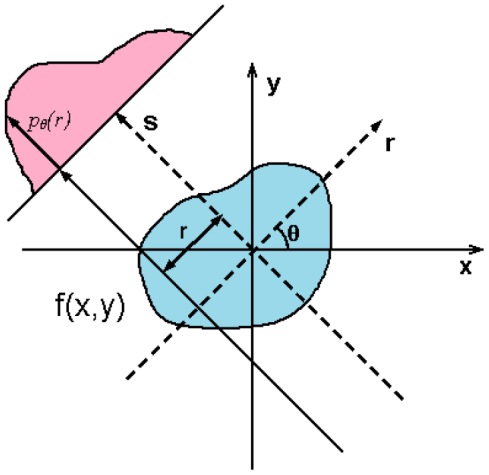

Figure 5.1: Tomographic transformation illustration. $f(x, y)$ is an unknown 2D object shown with the blue area, $p_\theta(r)$ is a measured 1D projection of the object taken at an observation angle θ [19].

Generally, we can think of the available and unknown data in terms of matrices and vectors and then try to compute the solution. If we have a measured data vector $\vec{m}(m \times 1)$ and we represent the model of a system by a matrix $\vec{A}(m \times n)$, then the input data vector $\vec{x}(n \times 1)$ can be calculated. Naively, we say that $\vec{m} = \vec{A}\vec{x}$ and the back projected image $\vec{x} = (\vec{A}^T\vec{A})^{-1}\vec{A}^T\vec{m}$. However, in reality the experimental measured data $\vec{m}$ is noisy, the system model imparted by a measurement procedure $\vec{A}$ is imperfect and the number of elements in $\vec{m}$ may not match $\vec{x}$. The approach to solve such problems is to resort to an iterative reconstruction technique such that $\|\vec{m} - \vec{A}\vec{x}\|^2 = \|\delta\|^2$. There is always an objective function corresponding to an iterative reconstruction technique e.g. least squares or maximum-likelihood expectation maximization. The task is then to find $\vec{x}$ such that $\vec{x} = argmin_{\vec{x}}\|\vec{m} - \vec{A}\vec{x}\|^2$. The algorithm of tomography is shown in the form of a flow chart in Fig. 5.2.

In terms of algebraic methods, tomography consists of assuming that the object consists of an array of unknowns, and then setting up algebraic equations for the unknowns in terms of the measured projection data. Basically, a square grid is superimposed over the unknown image and the image values are assumed to be constant within each cell of the grid. If the number of equations are greater than the number of unknowns, we have the case of an *overdetermined system* and the solution oscillates in the neighborhood of the true solution. If the number of equations are less than the number of unknowns,we have the case of an *underdetermined system* and an infinite number of solutions are possible. In this case, the solution obtained corresponds to that point which is closest to the initial guess. Another attractive feature of an iterative approach is that it is possible to incorporate into the solution some type of a priori information about the image being reconstructed. For example, if it is known a priori that the image is nonnegative, then in each of the solution successively obtained, one may set the negative components equal to 0. One may similarly incorporate the information that image is 0 outside a certain area, if this is known.

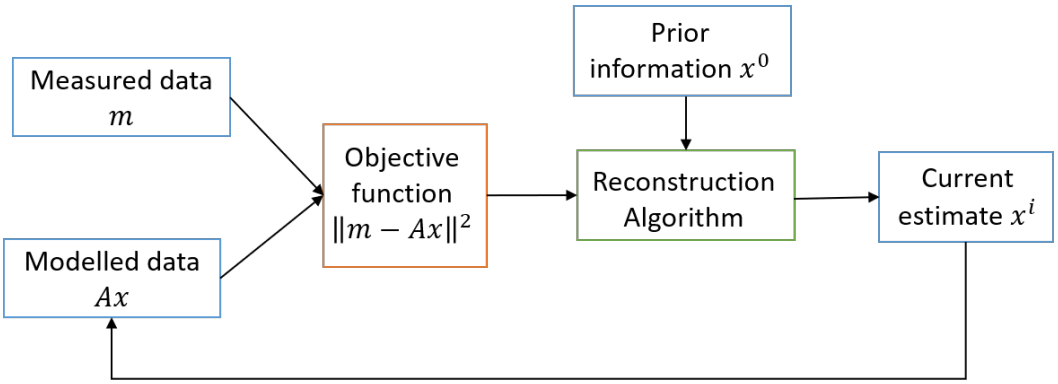

Figure 5.2: Flow chart of an iterative reconstruction method.

5.2 LPS tomography at PITZ

Longitudinal phase space tomography consists of a LPS rotating element and a diagnostics setup to measure the projections of the object to be reconstructed. In our case, the object to be reconstructed does not have spatial co-ordinates rather phase space co-ordinates in terms of electron bunch longitudinal temporal profile and momentum or energy spread distribution. LPS tomography utilizes an accelerating structure to rotate the LPS and the corresponding momentum projections are measured by a downstream dispersive arm. These projections are fed to an iterative algorithm to reconstruct LPS and the iterations are carried out until the results converge.

LPS reconstructions using tomography has been done in the past at different facilities including PITZ [19, 70, 71]. The main set up at PITZ for LPS tomography is shown in Fig. 5.3. Electron beam produced from the photocathode is accelerated by the RF gun. The phase of the gun is varied and the corresponding mean momentum and momentum spread can be measured as a function of the gun phase at the low energy dispersive arm (LEDA). Then, generally, at the maximum mean momentum gain phase of the gun, the beam is further accelerated by the booster. The booster is utilized to rotate the electron beam LPS by varying its phase. A set of quadrupoles and a steerer is used to focus and center the beam at a reference screen for the momentum measurements. Once the beam is optimized for the momentum measurement, the dipole (HEDA1) is switched ON and the beam is deflected 180° i.e. the beam observed on the screen is now in $x - p_z$ plane. The momentum projections corresponding to these phases are measured on a momentum calibrated screen *yscale*. The data is saved and fed offline to a reconstruction tool. The tool is run on a gpu-based system to obtain results within five to ten minutes, depending on the number of projections, without running into memory-based issues.

Owing to the unqiue setup and parameter space for different types of accelerators, the method is not straight forward. For low energy and high brightness electron beams like the ones at PITZ, there are some issues that have to be addressed. It is important to know what should be the range and step size of the booster phase and what algorithm should be chosen that gives artefact-free reconstruction results. The experimental conditions should be optimized to have better momentum resolution

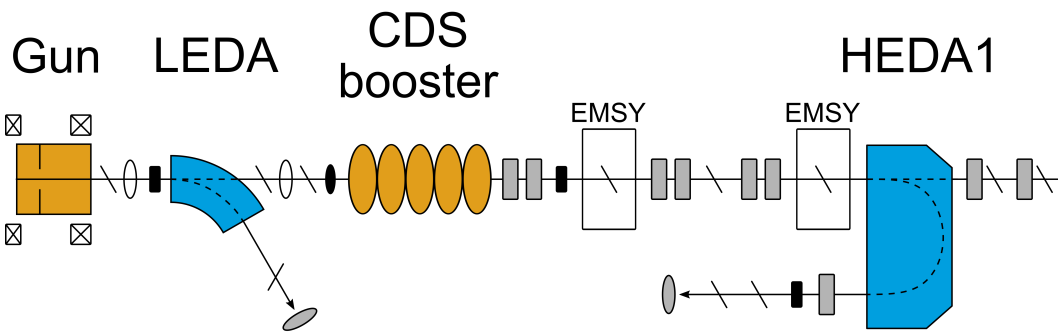

Figure 5.3: Experimental setup for LPS Tomography at PITZ

and SNR. These concerns for LPS tomography, that were previously not addressed at PITZ, have been catered in this thesis work. First, an LPS model is derived to understand the phase advance of LPS, which in turn, enables to determine the correct booster phase range. After that, the proof-of-principle simulations are done on ASTRA simulated beams. Then, the method is applied to the experimental beams that are similar to the simulated beams and their results are compared. This chapter ends with a summary of the LPS tomography and in particular, the improvements made recently in the methodology.

5.3 LPS modelling

To derive an analytical model for the longitudinal phase space of a beam, the beam dynamics can be described in terms of an equivalent ellipse model as shown in Fig. 5.4. This modelling of the LPS properties is done purely from a statistical point of view, without taking LPS nonlinearities and space charge effects into account.
If we consider a particle with an initial momentum from the electron gun p_z^{gun} is being accelerated by the booster, then the final momentum of the particle p_z^{boo} can be calculated by Eq. 5.1:

$$p_z^{boo} = p_z^{gun} + S\delta\varphi + \delta p + V\cos(\varphi + \delta\varphi), \tag{5.1}$$

where S is the LPS linear chirp that defines the LPS correlation, V is the momentum gain by the booster, φ is the phase of the booster w.r.t. maximum mean momentum

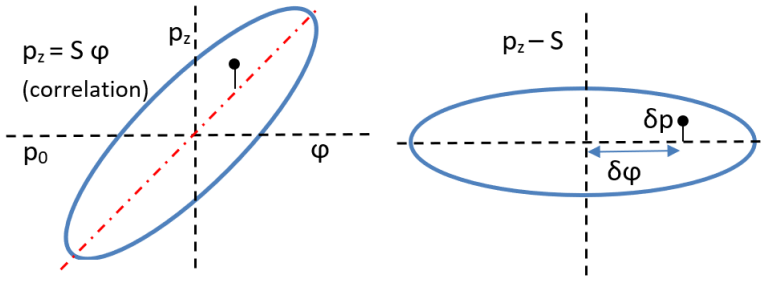

Figure 5.4: LPS (left) with correlation (right) w/o correlation.

gain phase and the $(\delta\varphi, \delta\mathrm{p})$ are the coordinates of the particle in the phase space. The average beam momentum after the booster can be found by integrating all the particles in the phase space ellipse.

$$\langle p_{\mathrm{z}}^{\mathrm{boo}} \rangle = \int p_{\mathrm{z}}^{\mathrm{boo}} dp d\varphi. \tag{5.2}$$

After a few mathematical steps, we derive Eq. 5.3:

$$\langle p_{\mathrm{z}}^{\mathrm{boo}} \rangle = p_{\mathrm{z}}^{\mathrm{gun}} + V \cdot \cos\varphi \cdot (1 - \sigma_{\varphi}^2/2), \tag{5.3}$$

where σ_{φ} is the electron beam bunch rms phase duration. The momentum deviation can be found by subtracting the mean momentum from the momentum distribution.

$$\Delta p_{\mathrm{z}}^{\mathrm{boo}} = p_{\mathrm{z}}^{\mathrm{boo}} - \langle p_{\mathrm{z}}^{\mathrm{boo}} \rangle \,. \tag{5.4}$$

After plugging in the values of beam momentum and its average and solving them, we get the expression:

$$\Delta p_{\mathrm{z}}^{\mathrm{boo}} = S\delta\varphi + \delta p - V sin\varphi\delta\varphi + V cos\varphi(\frac{\sigma_{\varphi}^2}{2} - \frac{(\delta\varphi)^2}{2}). \tag{5.5}$$

Squaring the above equation and neglecting higher order terms, we find the expression:

$$\langle \Delta p_{\mathrm{z}}^{\mathrm{boo}^2} \rangle = \sigma_{p0}^2 + (S\sigma_{\varphi} - V sin\varphi\sigma_{\varphi})^2, \tag{5.6}$$

where $\langle \Delta p_z^{\mathrm{boo}^2} \rangle = \sigma_p^2$ is the rms momentum spread squared. The chirp S can be found at the minimum energy spread phase by taking the derivative of the above equation.

$$2\sigma_p \sigma_p' = 2\sigma_\varphi^2 (S - V \sin\varphi) V cos\varphi = 0, \tag{5.7}$$

where, $S = V \sin\varphi_{\sigma_{p(min)}}$. Hence, after plugging in S, the final squared rms energy spread is:

$$\sigma_p^2 = \sigma_{p(min)}^2 + V(\sin\varphi - \sin\varphi_{\sigma_{p(min)}} \sigma_\varphi)^2. \tag{5.8}$$

The approximate bunch length can be found from the expression:

$$\sigma_\varphi = \sqrt{\langle (\delta_\varphi)^2 \rangle} = \frac{\sigma_\varphi}{|dp_z/d\varphi|} = \frac{\sigma_p}{|V \sin\varphi|}. \tag{5.9}$$

The phase advance Φ of the phase space ellipse can be calculated by using the bunch length σ_ϕ and the minimum rms energy spread. The formula is shown in Eq. 5.10:

$$\Phi = \tan^{-1}(S\sigma_\varphi/\sigma_{p_{min}}). \tag{5.10}$$

In the experiment, we can use the modelled energy spread as the LPS chirp and find the beam phase advance. As the booster phase varies, the beam phase advance is significant around the minimum energy spread phase and decreases gradually as the energy spread increases.

5.4 Proof-of-principle simulations

Methodical studies were done first on the simulated beams as the field of accelerator physics relies heavily on particle tracking simulations for the study of beam dynamics in an accelerator. An ASTRA generated beam with 200,000 macro particles was utilized for doing the booster phase scan. The particles were produced by a 6.6 ps FWHM temporal gaussian laser and a charge of 250 pC was extracted from the cathode. The space charge forces in the booster were not considered here as the analytic LPS model is derived without taking space charge effects into account. The beam size aperture was 1.0 mm and the solenoid current value was kept constant.

Figure 5.5 shows the LPS of the beam after the gun at the MMMG phase. This beam is then rotated in phase space during the booster phase scan.

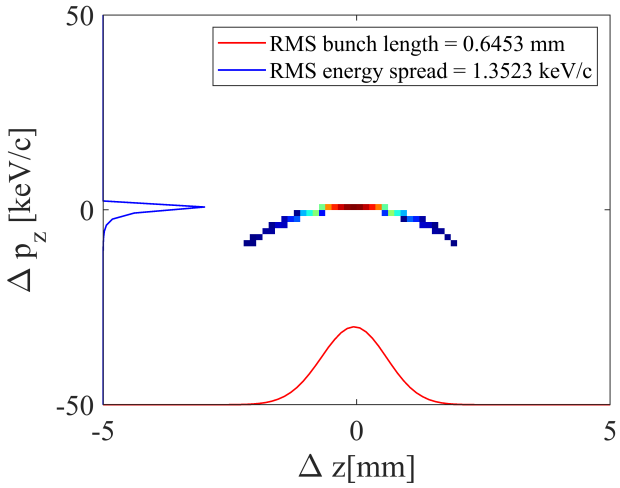

Figure 5.5: LPS for 250 pC beam without space charge after the gun.

5.4.1 Gun and booster phase scan

The power in the gun was set such that the electron beam momentum was around 6.3 MeV/c, close to the experimental conditions. To find the phase corresponding to the maximum mean momentum gain p_z^{gun}, the gun phase was varied from $-10°$ to $10°$ around the approximated MMMG phase. The momentum of the particles corresponding to each gun phase was simulated upto a distance of 1.7 m from the cathode, the location of LEDA in the beamline. The mean momentum and the momentum spread of these particles were calculated. After the scan, the gun phase was set to MMMG phase. Figure 5.6 (left) shows the results of the gun phase scan. Then the beam was sent to the booster. The power in the booster was set such that the maximum beam momentum after the booster was close to 17 MeV/c. The booster phase was varied from $-10°$ to $10°$ w.r.t. the MMMG phase and the momentum of the particles at the reference screen position of HEDA1 dipole was simulated i.e. at 8.92 m from the cathode. The mean momentum and the momentum spread of these particles were calculated for each phase. The momentum gain V of the beam in the booster was calculated by subtracting the mean momentum of the beam ex-

iting the booster from the maximum p_z^{gun}. The values required for the analytically modelled equations of the mean momentum and the momentum spread were calculated from the simulated data and then plotted against the simulated momentum and momentum spread scans. Figure 5.6 (right) shows that both the first and second order of moments calculated from the model fit to the simulated data with less than 1 % rms error around the MMMG and the minimum energy spread phase.

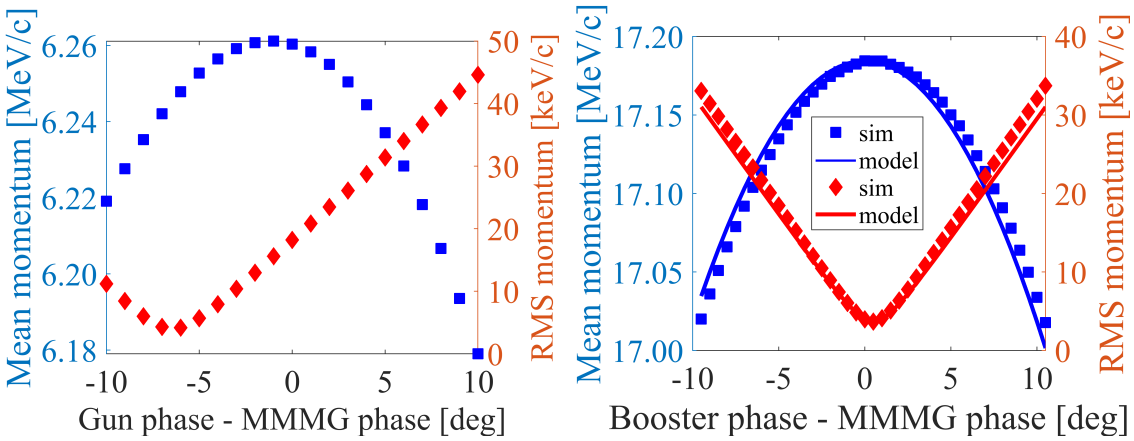

Figure 5.6: (left) Gun phase scan, (right) Booster phase scan.

Phase advance analysis

For the calculation of the phase advance, equation 5.10 shows that the bunch length, the minimum energy spread and the LPS chirp at each phase must be known. In the simulation, the slope is found from the first order polynomial fit to the LPS. But since in the experiment, we don't have that information, S values can be substituted by the energy spread model values.

Figure 5.7 (left) shows the phase advance corresponding to each booster phase. The phase advance varies significantly around the minimum energy spread phase but at the off-crest phases, its change is gradual. This provides the key information to consider the booster phase range and step size for tomography. One can also correlate phase advance with the energy spread as shown in Fig. 5.7 (right). As the booster phase varies, the beam phase advance is significant around the minimum energy spread phase and then decreases gradually as the energy spread increases. The momentum projections for tomography should correspond to the booster phase

range which covers the whole LPS phase advance and the step size should be optimized in order to produce a smooth curve. Hence, this significantly reduces the booster phase scan range and the data taking time during the experiment.
Previously at PITZ, the booster phase range was defined according to the visible beam position on the screen for a particular dipole current. The goal was to have as many momentum projections as possible. Also, to have reasonable number of projection to reduce the computation time of the reconstruction, the booster phase step size was kept approximately 2°. This caused missing information regarding the rapidly varying energy spread around the minimum energy spread phase. Thus, the phase advance analysis provided significant improvement in terms of determination of booster phase, step size, data taking and reconstruction time.

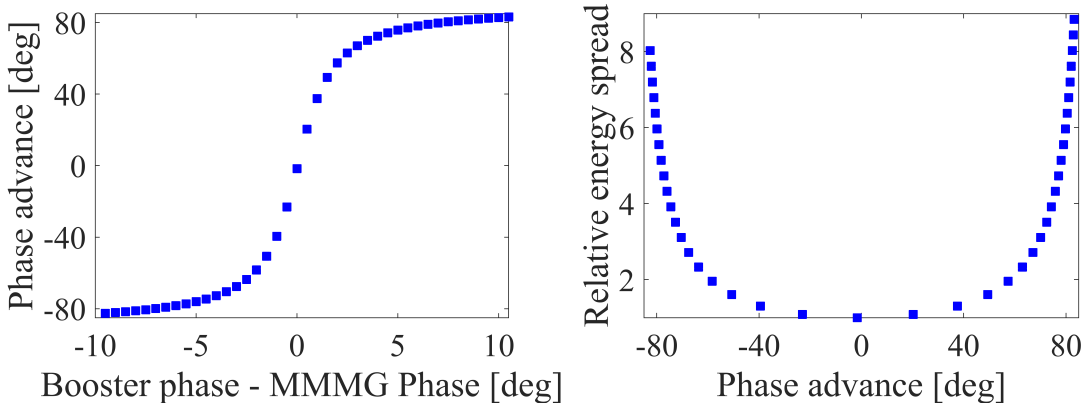

Figure 5.7: (left) Phase advance w.r.t. booster phase scan (right) Relative energy spread variation w.r.t. the phase advance.

5.4.2 Reconstruction algorithm

There are different computer implementations of the algebraic algorithms represented by the acronyms ART, SIRT, SART, and ISRA [68, 72]. They vary in terms of the convergence speed and the accuracy of results. Algebraic Reconstruction Technique (ART) gives good convergence speed but shows noise-like artefacts in the reconstruction results, where as Simultaneous Iterative Reconstruction Technique (SIRT) leads to better looking images at the expense of slower convergence. Simultaneous Algebraic Reconstruction Technique (SART) combines the best of ART

and SIRT. It yields reconstructions of good quality and numerical accuracy in a few iterations [68]. SART subtracts the measured momentum projections from the back projected modelled momentum projections, forward projects the difference and normalizes the results. This result is added to the current estimate to yield the next update.

Another algorithm that is derivable from a least squares objective function is Image Space Reconstruction Algorithm (ISRA) [72]. ISRA has the added advantage that it is inherently a non-negative multiplicative algorithm and therefore, has no negative pixels. ISRA takes a current estimate and forward projects it to form a vector $\vec{A}\vec{x}^k$. This vector is back projected to form a predicted back projected vector $\vec{A}^T\vec{A}\vec{x}^k$. Similarly, the measured projections $\vec{m}$ are also back projected using the system matrix $\vec{A}$. The ratio of these back projections provides a correction factor to update the current estimate. The initial estimate x^1 vector can be taken as a vector of uniform values e.g. 1.

$$\vec{x}^{k+1} = \vec{x}^k + \frac{1}{\vec{A}^T 1}\frac{\vec{A}^T(\vec{m} - \vec{A}^T\vec{x}^k)}{\vec{A}^T 1}. \tag{5.11}$$

$$\vec{x}^{k+1} = \vec{x}^k \frac{\vec{A}^T\vec{m}}{\vec{A}^T\vec{A}\vec{x}^k}. \tag{5.12}$$

The equations for SART and ISRA are expressed in Eq. 5.11 and Eq. 5.12, respectively. In both the equations, $\vec{x}^k$ is a vector containing the current estimate of reconstructed phase space and $\vec{x}^{k+1}$ is the next update, $\vec{m}$ is a vector that contains projections corresponding to all booster phases also known as *sinogram* and $\vec{A}$ is a weight matrix built from the LPS model. Generally, the iterations are carried out until the root mean square error (RMSE) between measured sinogram and predicted sinogram falls below the tolerence level, e.g. 0.5 %. The number of iterations can also be set beforehand based on the expected convergence.

Data representation

For the case of simulations, once we have the momentum projections corresponding to each booster phase from ASTRA, they were plotted in the form of a bivariate histogram with equally spaced bins, where the height of the bin indicates the in-

tensity. Additionally, the edges of the bins in each dimension were also fixed for the booster phase scan. This is done to replicate the experimental set-up where the screen edges define the momentum range, the pixels define the momentum resolution and the counts per pixel define the signal intensity of the electron beam. Thus, the simulation parameters were kept similar to the experimental set-up. The momentum projections corresponding to the booster phase scan and its alternative representation in the form of a sinogram is shown in Fig. 5.8.

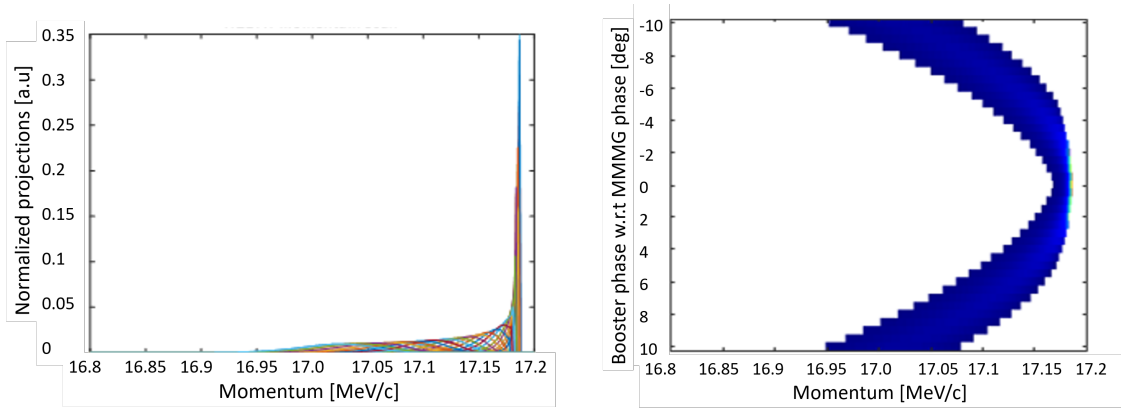

Figure 5.8: (left) Normalized momentum projections acquired during the booster phase scan (right) Sinogram of projections.

Measurement system representation

Weight matrix $\vec{W}$ or the system matrix $\vec{A}$ is built from the mean of the modelled momentum data and with an iterative model there is sufficient flexibility regarding how it is parameterized. The bins of this weight matrix are filled by taking the ratio of the difference between the calculated momentum and the minimum momentum, and the momentum resolution. Any j^{th} bin number is only equal to 1 if this ratio is positive and less than the total number of elements. The number of rows of the weight matrix are N_sxN_φ and number of columns are N_txN_s. A schematics showing the dimensions of weight matrix is shown in Fig. 5.9 and the algorithm for building the weight matrix is shown in the form of a pseudo code in Algorithm 1.

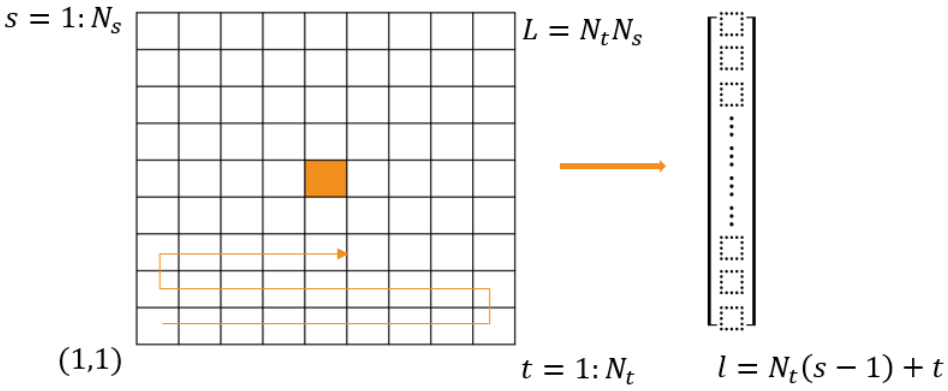

Figure 5.9: Construction of a weight matrix.

Algorithm 1: Weight matrix for LPS Reconstruction

input : φ, p_z^{gun}, V, z

output: $WeightMatrix$ (consists of 1s and 0s)

Function `Loop(`A`)`
  $N_\varphi \leftarrow$ length(booster phases)
  $N_s \leftarrow$ length(momentum bins)
  $N_t \leftarrow$ length(longitudinal bins)
  for $i \leftarrow 1$ *to* φ_{max} **do**
    for $s \leftarrow 1$ *to* N_s **do**
      for $t \leftarrow 1$ *to* N_t **do**
        $p_{cal}^{boo} \leftarrow p_z^{gun}(s) + Vcos(\varphi(i) + z(t))$
        $j \leftarrow \frac{p_{cal}^{boo} - p_{min}^{boo}}{\Delta p_{boo}}$
        $W(j + N_s(i-1), t + N_t(s-1)) \leftarrow 1$
  return $WeightMatrix$

Since in the simulations, we know the true LPS, the initial vector $\vec{x}^1$ was taken as the true LPS and was forward projected using the weight matrix $\vec{A}$ to build vector $\vec{A}\vec{x}^k$. The overall structure of the resultant sinogram was similar to the actual one, but there were gaps in it, see Figure 5.11 (left). The empty pixels were present as a result of the signal's analogue to discretization conversion effects. To address this

issue, the weight **1** of the j^{th} pixel was distributed in the size $(3, 3)$ surrounding neighboring pixels by bilinear interpolation.

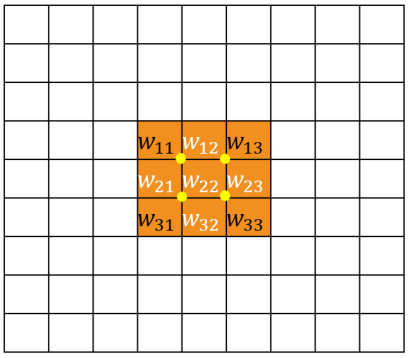

Figure 5.10: Weight matrix with bilinear interpolation.

Let's denote the weight of the central pixel w_{22}, one can find the weight of the corner pixels $w_{11}, w_{31}, w_{13}, w_{33}$ by considering the solution as a weighted mean, where the weights sum to 1 and satisfy the transposed linear system.

$$\begin{bmatrix} w_{11} \\ w_{31} \\ w_{13} \\ w_{33} \end{bmatrix} = \frac{1}{(t_2 - t_1)(s_2 - s_1)} \begin{bmatrix} t_2 s_2 & -s_2 & -t_2 & 1 \\ t_2 s_1 & s_1 & t_2 & 1 \\ t_1 s_2 & s_2 & t_1 & 1 \\ t_1 s_1 & -s_1 & -t_1 & 1 \end{bmatrix} \begin{bmatrix} 1 \\ t \\ s \\ ts \end{bmatrix}. \tag{5.13}$$

Here, $t_2 - t = t - t_1 = \Delta t$ is the step size of the longitudinal bins and $s_2 - s = s - s_1 = \Delta s$ is the step size of the momentum bins. It is also worthy to note that once the calculated maximum mean momentum value is reached, the signs of s_2 and s_1 have to be swapped in order to keep Δs positive.
Once the four corner values are known, one can find the other five weight values by using the same matrix equation and just replacing the co-ordinates (t, s), see Figure 5.10. Thus, the weight matrix changes to the following form:

$$W((j : j + 8) + N_s(i - 1), t + N_t(s - 1)) = \vec{W}, \tag{5.14}$$

where $\vec{W}$ is a (9×1) vector filling the columns of the weight matrix.
Figure 5.11 (right) shows the sinogram built from the updated weight matrix. It is

obvious that the empty bins in the sinogram have significantly reduced. Looking closely at the edges of the sinogram, one finds some pixels missing at the edges. There might still be some systematic error resulting from the rounding off of the bin number j. This can be further improved by increasing the resolution of the reconstructed phase space but at the expense of the increase in the computational time. Note that in order to achieve the best results and reduced pixel noise, the resolution of the bivariate histogram and the resolution of the reconstructed phase space should be kept the same.

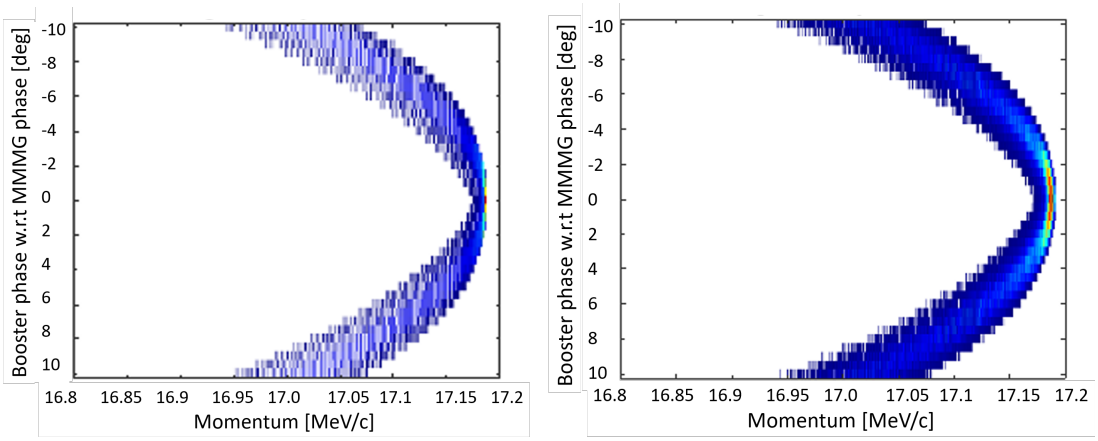

Figure 5.11: (left) Sinogram from the true LPS and weight matrix (right) Sinogram from true the LPS and the modified weight matrix.

5.4.3 Reconstruction results

The true LPS after the gun, shown in Figure 5.5, was very thin consisting of only a few pixels since it was a cold beam with filamet-like phase space. Note that it is very challenging to reconstruct such a narrow phase space as it requires great precision. As a first step, to check the reconstruction results of the algorithm and also its convergence, the initial estimate was taken as the true LPS. The simulated sinogram was fed to the algorithm and the iterations were carried out with the improved weight matrix. It was observed that even after almost 50 iterations, the results were converging. The calculated bunch length and the energy spread values were very close to the true values. The bunch length profile was not smooth because

of the pixelization effect but fitting a gaussian to the profile gives a smooth result. Only a few noise-like pixels on the right of the reconstructed LPS were emerging that had very low intensity and so negligible effect on the calculated bunch length and the energy spread. Figure 5.12 shows the reconstructed results.

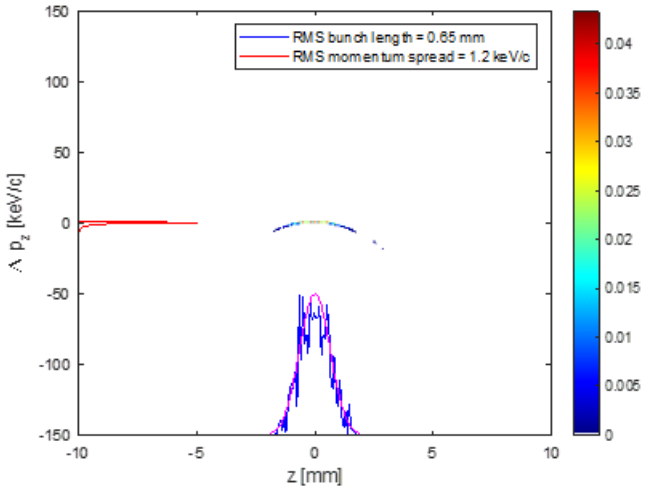

Figure 5.12: Reconstructed LPS where $\vec{x}^1$ = True LPS.

In the next step, the initial estimate was taken as a uniform vector consisting of 1. The reconstructed LPS after 50 iterations had many artefacts resulting in the overestimation of the bunch length and the energy spread, see Figure 5.13. One can see from the gaussian fit on the bunch length that the artefacts corrupt the results. Reasonable values can only be obtained after application of a charge cut. The charge cut forces all the values below a defined threshold to be 0. This not only removes the noise but also cuts away the intensity pixels that belong to the actual LPS. Previously, a charge cut of 15-20% was applied at PITZ to give reasonable values of energy spread and bunch length.

Initial LPS guess

To further improve the reconstruction results, an initial educated guess of LPS from the low energy section, i.e. the section after the gun, was established. Basically, the momentum profile at an off-crest booster phase $\rho_n(p_z)$ was used to select the range

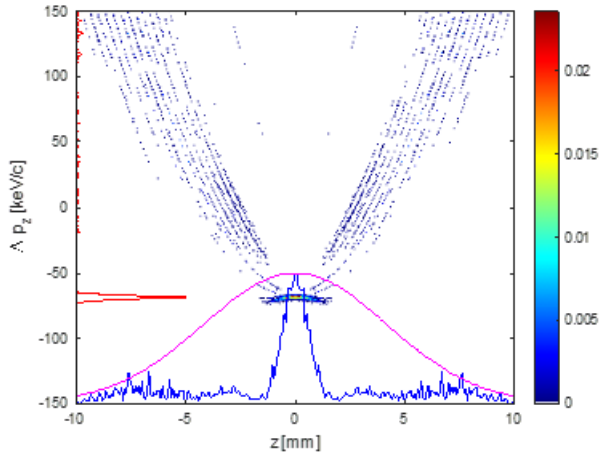

Figure 5.13: Reconstructed LPS where $\vec{x}^1 = 1$.

of the gun phase from the LEDA scan to be used as an initial matrix.

$$\rho(p_z) = \rho\left(\frac{p_z^{gun} - p_{z_{mean}}^{gun}}{(dp_z^{boo}/d\varphi_{off-crest})} = \varphi\right) = \rho(\varphi). \tag{5.15}$$

Equation 5.15 shows the the formula to find the proper phase range, where φ represents the booster phase. Figure 5.14 (left) shows a red box around the MMMG values to give an idea of the phase range selected. Once we had the range, the mean momentum points were interpolated and a gaussian was fit on each of the mean momentum points as shown in Fig. 5.14 (right). The amplitude of the gaussians was taken from the weights of the off-crest phase ($-10°$) momentum profile normalized to 1. The energy spread of the gaussians was assumed roughly from the minimum energy spread value. The expression of the initial guess for the LPS can be written mathematically as:

$$LPS(z, p_z) = \sum_{n=1}^{N} G_n(p_z)\Delta_n(z), \tag{5.16}$$

where $G_n(p_z)$ is the p_z- distribution for the n^{th} longitudinal slice within the bunch scanned by the step function $\Delta_n(z)$.

$$G_n(p_z, \sigma_p) = \rho_n/(\sqrt{2\pi}\sigma_{pn}) \exp^{[-(p_z - p_{z_n})^2/(2\sigma_{p_n}^2)]}. \tag{5.17}$$

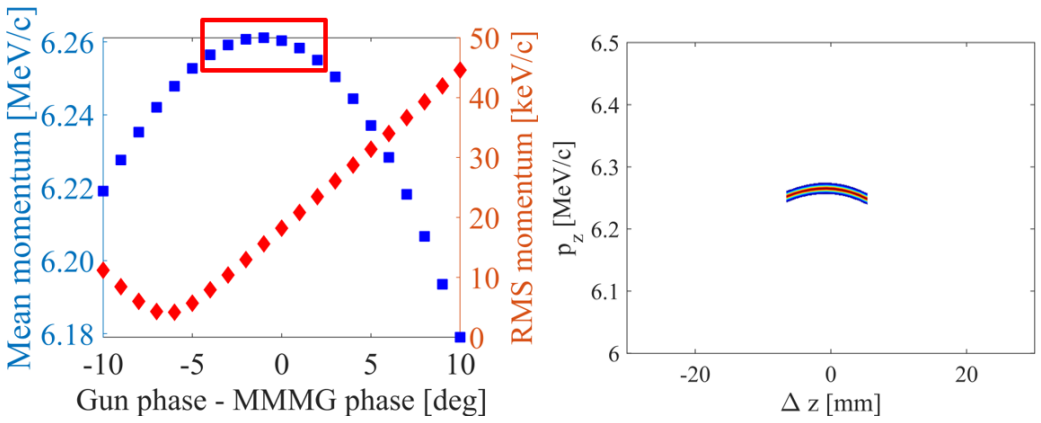

Figure 5.14: (left) Initial matrix selection from gun phase scan (right) Initial matrix.

$$\Delta_n(z) = 1/\Delta z, |z - z_n| \leq \Delta z/2. \tag{5.18}$$

Equations 5.17 and 5.18 show the formulas of the n^{th} Gaussian and the delta function in terms of the bunch length and momentum spread coordinates. The reconstructed LPS after 50 iterations starting from a well-defined initial estimate is shown in Fig. 5.15. The initial estimate from the LEDA removes the noise-like artefacts scattered in the reconstructed LPS. Additionally, it also impacts the overall distribution of particles in the phase space. Being an underdetermined system, the initial guess from LEDA assists the algorithm to achieve a unique result out of infinite many solutions. Therefore, the rms bunch length and energy spread of reconstructed LPS shown in Fig. 5.15 are much closer to the true values. Thus, the initial estimate from the LEDA not only removes the noise but also impacts the overall distribution of the particles in the phase space. As mentioned earlier, it is very challenging to reconstruct a filament-like phase space due to the high demand on the accuracy of placement of weights in the proper bin, therefore, there are a few noisy pixels on top of the LPS. The rms was calculated between the simulated sinogram and the predicted forward projection. Figure 5.16 shows that the results already start to converge after 30 iterations and then until 50, the RMSE remains the same, i.e., $< 0.2\,\%$. The expression for RMSE can be expressed as:

$$RMSE = \sqrt{\sum_i \left(\vec{A}\vec{x}^k - \vec{m}\right)^2}. \tag{5.19}$$

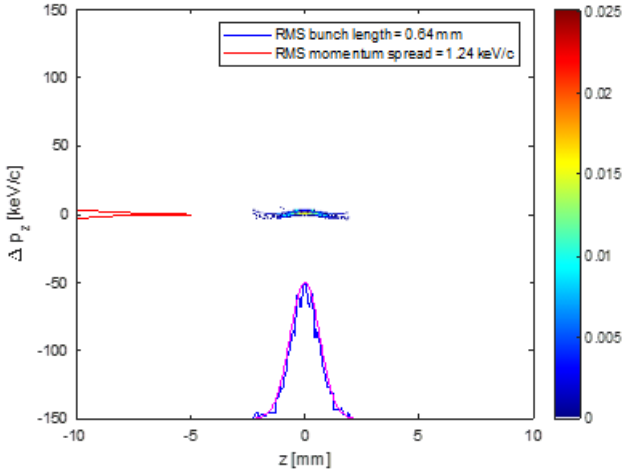

Figure 5.15: Reconstructed LPS with initial matrix established from LEDA.

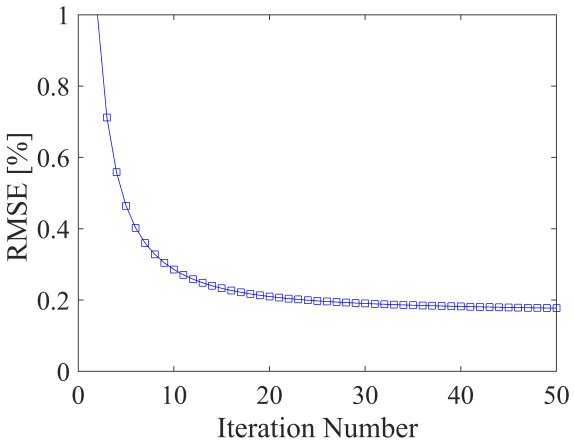

Figure 5.16: RMSE between the simulated sinogram and the predicted forward projection.

5.4.4 Space-charge dominated beam

Methodical studies were also carried out on an ASTRA-generated beam *including* space charge effect. A 6.0 ps FWHM temporal Gaussian laser beam was used to produce a 250 pC beam charge with 200,000 particles. The transverse rms size of the beam was kept 0.25 mm in both x and y axes. As the LPS analytical model derived in section 5.3 does not include the space charge forces, a procedure was devised to strongly reduce the space-charge effects of the simulated beam. Basically, the idea was to introduce a slit in the beam path to truncate it in the non-dispersive plane before it enters the booster cavity, reducing the particle density and hence the space charge effect. Additionally, an attempt was made to study the slice energy spread since it is of critical importance for FELs [18].

Study on slit effect

Initially, ASTRA was used to track the beam including space charge until a distance of 0.8 m from the cathode, since this is the location in the beamline which has a slit installed (Low.Scr1). Then, the particles at this location were imported in Matlab and a corresponding filter was introduced to understand the effect of the slit on the LPS of the beam. It was further explored how varying the width of the slit changes the rms bunch length and the energy spread.
Basically, the slit width was varied from 50 µm to 10 mm with a variable step size at the location of Low.Scr1. Figure 5.17 and 5.18 display the beam distribution in the spatial co-ordinates as well as the LPS for both the cases; without the slit and with a 200 µm-wide slit, respectively. The slit chops the beam in y and therefore, only the central beamlet is visible in $x-y$ and $z-y$ co-ordinates, whereas in $z-x$ co-ordinates, the whole beam is visible but the particle density is reduced, see Figure 5.18. A comparison of the LPS of the beam with and without the slit was also made. It was observed that the overall shape of the LPS is preserved after inserting the slit but the calculated rms bunch length and the energy spread values are slightly increased. This is because the introduction of the slit reduces the particle density, which in turn, makes the profiles of the projections more of a flat-top instead of a Gaussian and hence the effective rms sizes change. There are also tiny modulations riding on top of the flat top. This is the noise from the finite pixel size. If the bin

size is made larger, the modulations would be averaged out and the profiles will become more smooth.

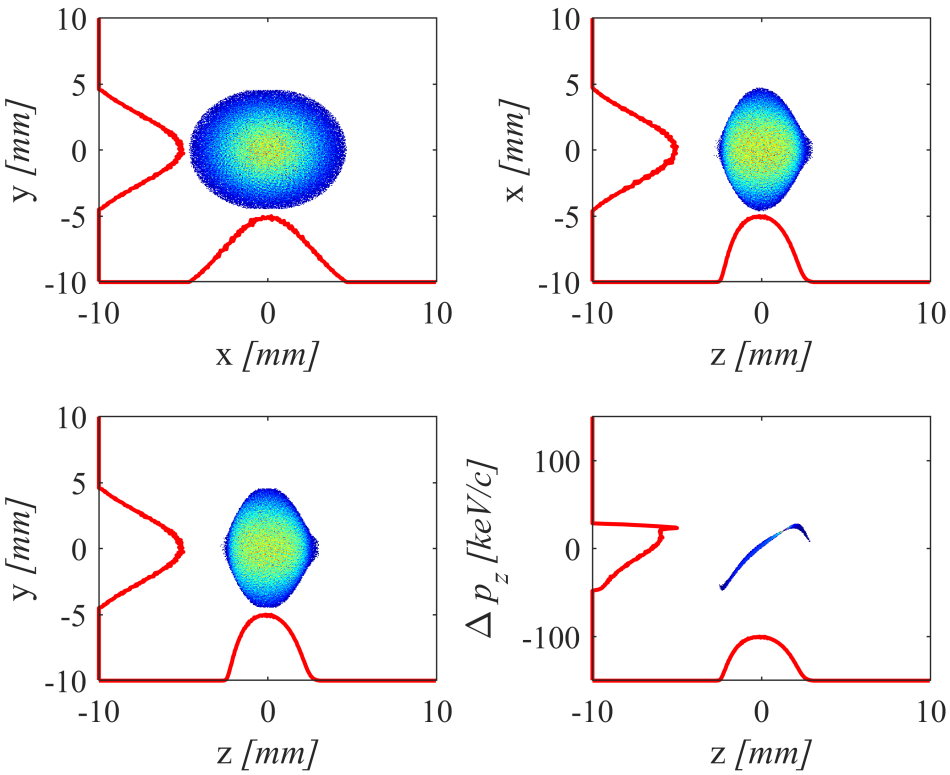

Figure 5.17: Astra beam distribution before inserting the slit.

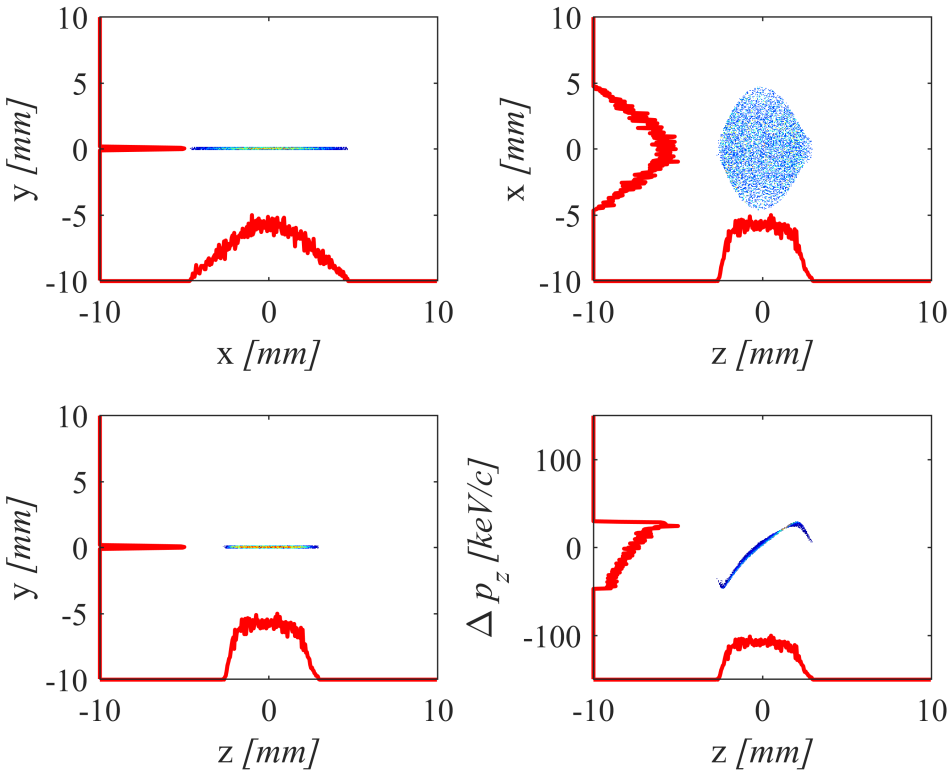

Figure 5.18: Beam distribution after inserting the 200 µm-wide slit. Charge reduced from 250 pC to 10 pC.

Figure 5.19 shows the results of the slit width scan at the location of Low.Scr1. The rms bunch length is approximately 1.33 mm around 200 µm slit width and then as the width increases, the bunch length was reduced. The rms bunch length for the whole beam was calculated to be 1.15 mm. Similarly, the rms value of the projected energy spread was slightly less than 21 keV for 200 µm slit width and then it gradually decreased. The rms energy spread of the whole beam was calculated to be 18.2 keV.

Since the central slice is of critical importance for applications like lasing, a sub-picosecond central slice energy spread was also calculated to estimate the change in the slice energy spread as the slit width increases. For a 200 µm-wide slit, the slice energy spread was approximately 1.6 keV but for the whole beam, the slice energy spread was 1.7 keV, see Figure 5.20. A relative error of almost 6 % is introduced by the insertion of the slit.

The charge of the beam is also reduced after passing through the slit. Figure 5.21 shows the charge after the slit for different slit widths. For the case of 200 µm slit, the charge was reduced to 10 pC. Note that although the charge is reduced to 10 pC, the beam still imprints LPS of a 250 pC beam and *not* 10 pC beam.

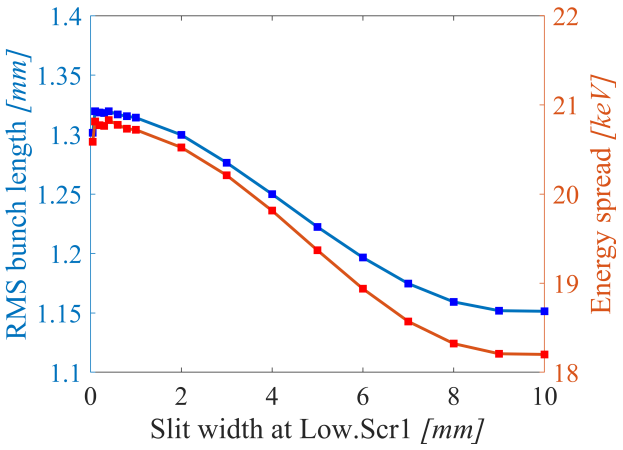

Figure 5.19: Increase in the rms bunch length and the projected energy spread as the slit width increases.

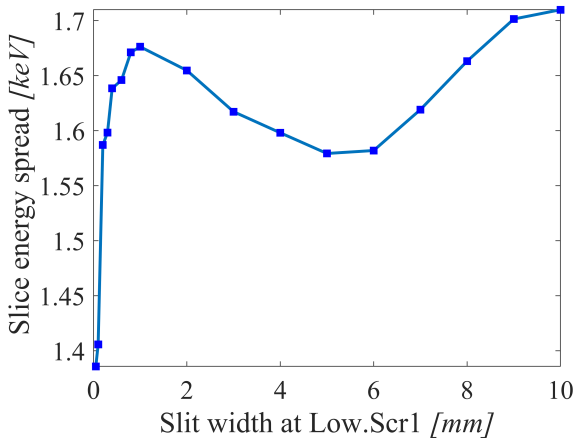

Figure 5.20: Slice energy spread of the central slice of sub-picosecond range for different slit widths.

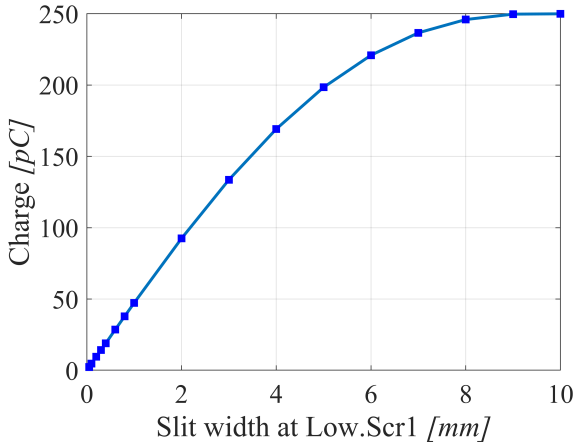

Figure 5.21: Charge obtained after the beam passes through different slit widths.

Booster phase scan with slit

After quantifying the increase in the rms bunch length and the energy spread of a 250 pC beam because of the slit, ASTRA simulations were carried out with a 200 µm-wide slit at a distance of 0.8 m from the cathode. Now the beam was tracked all the way to 8.92 m, which is the location of the reference screen for the momentum measurements, similar to the experimental setup. The booster phase was scanned for this truncated beam from $-10°$ to $10°$ w.r.t the MMMG phase. The LPS of the beam before and after truncation, near 0.8 m in the beamline, is shown in Fig. 5.22 along with their bunch and energy spread profiles. As previously simulated in Matlab, the overall shape of the LPS was preserved and the rms values of the bunch length and the energy spread were increased. Apart from the tiny modulations on top of both the projections, there were some additional kinks at the edges. They appear because of the density modulations at the head and the tail of the LPS. Therefore, for 200 µm-wide slit, the calculated rms bunch length and the energy spread is 1.44 mm and 21.4 keV, respectively.

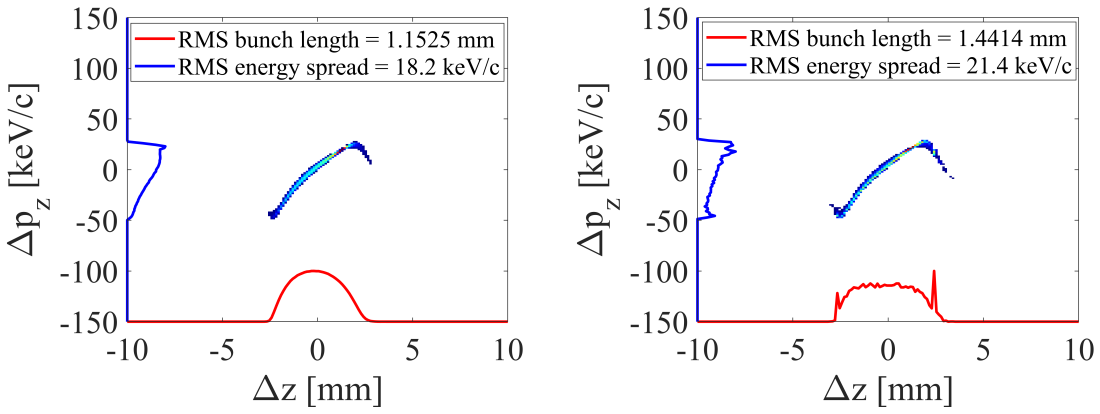

Figure 5.22: LPS before booster (left) without slit, (right) with slit.

The normalized projections corresponding to all the booster phases before and after beam truncation are shown in Figure 5.23. The profiles for the truncated beam are flat in the central part with ripples on the top and kinks at the edges. For both the cases, first the mean momentum and the momentum spread were calculated from the momentum projections and then, the mean momentum and the momentum spread were estimated from the analytical model. Figure 5.24 shows their values

plotted against the booster phases.

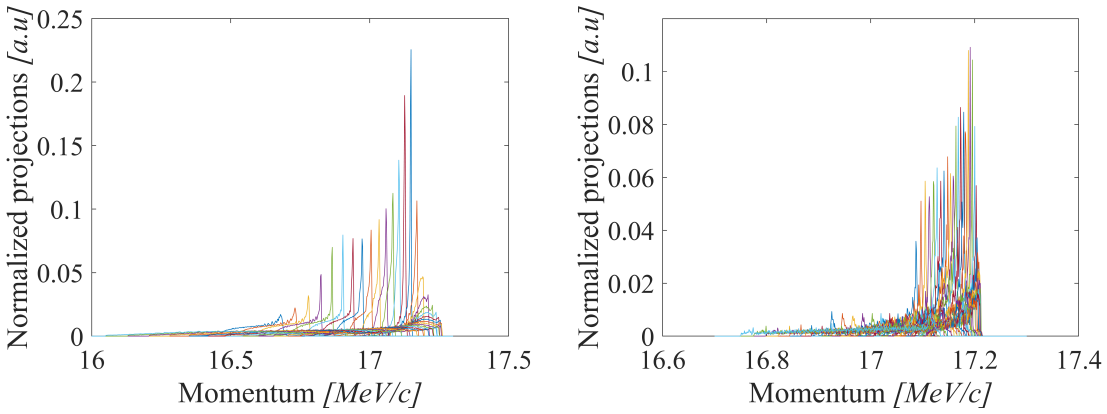

Figure 5.23: (left) Momentum projections corresponding to booster phase scan for 250 pC beam (right) Momentum projections corresponding to booster phase scan for 250 pC beam truncated by 200 µm-wide slit.

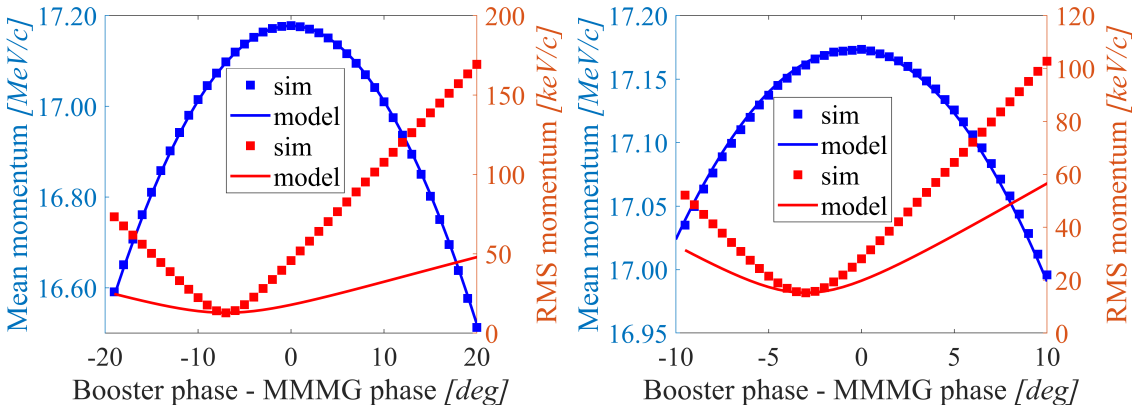

Figure 5.24: (left) Mean momentum and momentum spread during booster phase scan for 250 pC beam (left) Mean momentum and momentum spread during booster phase scan for 250 pC beam truncated by 200 µm-wide slit.

The mean momentum of the projections agrees with the model for the whole phase scan range but the momentum spread model only fits well around the minimum momentum spread phase. At the off-crest phases, it is underestimated, unlike the 250 pC case without the space charge forces, shown in Figure 5.6 (right). The reduction in the space charge force is evident by the shift in the minimum momentum

phase from −7° to around −3°. Basically, the energy spread model is used to estimate the bunch length and the slope of the phase space. This, in turn, is used to estimate the phase advance and hence, the booster phase range. The booster phase range is taken such that the change in relative energy spread (energy spread w.r.t the minimum energy spread) corresponding to the phase advance is negligible. Figure 5.25 (left) shows that until 1.5, the phase advance varies from −60° to 60°, and then till 2, the increase is only 10°. From 2 to 3, the increase is almost negligible. Figure 5.25 (right) shows that between −5° to 5° booster phase, the phase advance varies significantly and outside this range, the variation is gradual.

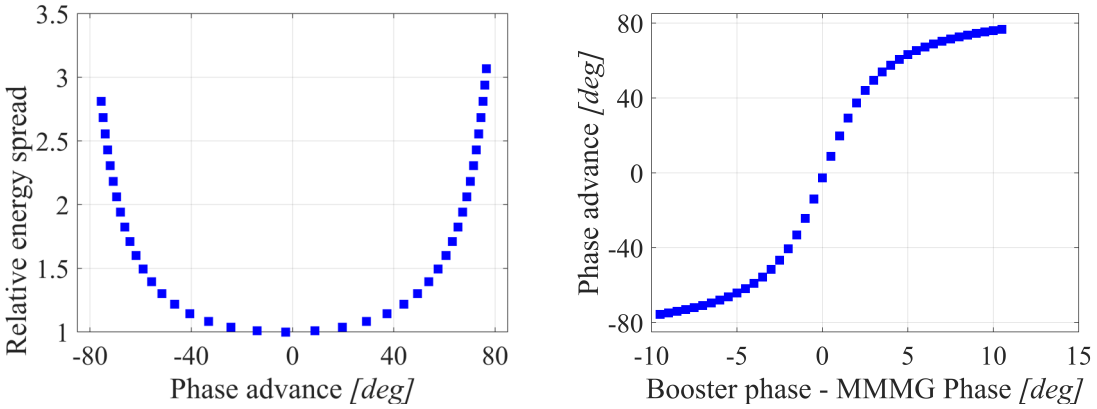

Figure 5.25: For the case of 250 pC beam truncated by 200 µm-wide slit (left) Phase advance corresponding to booster phase scan (right) Relative energy spread corresponding to phase advance.

Reconstruction results

There are three inputs to the reconstruction algorithm: sinogram, initial matrix and the number of iterations/convergence criterion. The weight matrix $\vec{W}$ in the reconstruction technique is calculated from the model. Since for the weight matrix, we make use of the mean momentum model which agrees well with the simulated mean momentum, it is expected that we get reasonably accurate results.
Initially, the LPS reconstruction was done using the SART algorithm in order to compare it with the results of the ISRA algorithm. The initial matrix was taken 0 because of the additive nature of the algorithm and at every step, the negative pixels during iterations were forced to be 0. The iterations were carried out until the results started to converge. Figure 5.26 shows the results after 50 iterations where the RMSE is approximately 0.2 %. The reconstructed LPS looks similar to the LPS after the slit shown in Figure 5.22 (right) but there are a lot of noise like artefacts scattered in the reconstructed area. Also, there is a layer of low intensity pixels surrounding the true LPS region. This is a source of overestimation in the rms energy spread and bunch length.

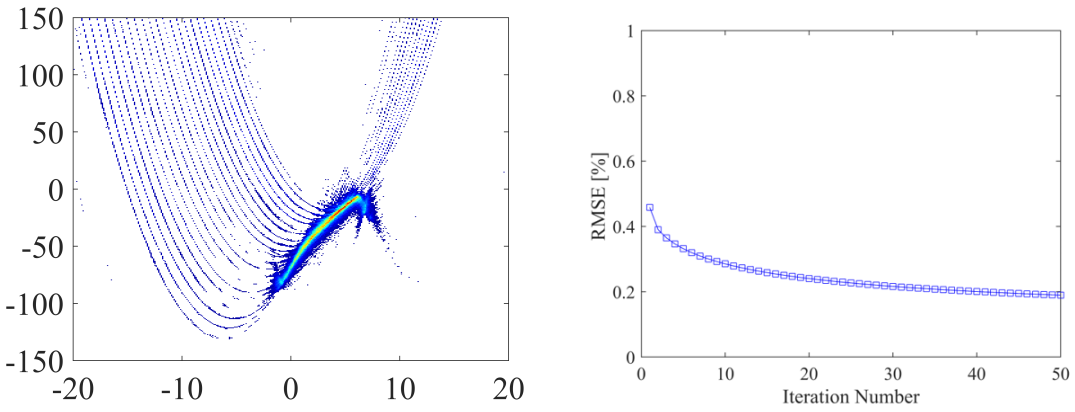

Figure 5.26: (left) Reconstructed LPS from SART (right) RMSE between simulated projections and predicted forward projections after 50 iterations.

Next, ISRA was used to reconstruct the LPS. A positive uniform matrix was taken as the initial matrix and iterations were done until the results started to converge. Figure 5.27 shows the results after 50 iterations where the RMSE is about 0.1 %. The noisy artfacts scattered in the reconstruction region are significantly reduced.

Also, the LPS structure does not have surrounding low intensity values.

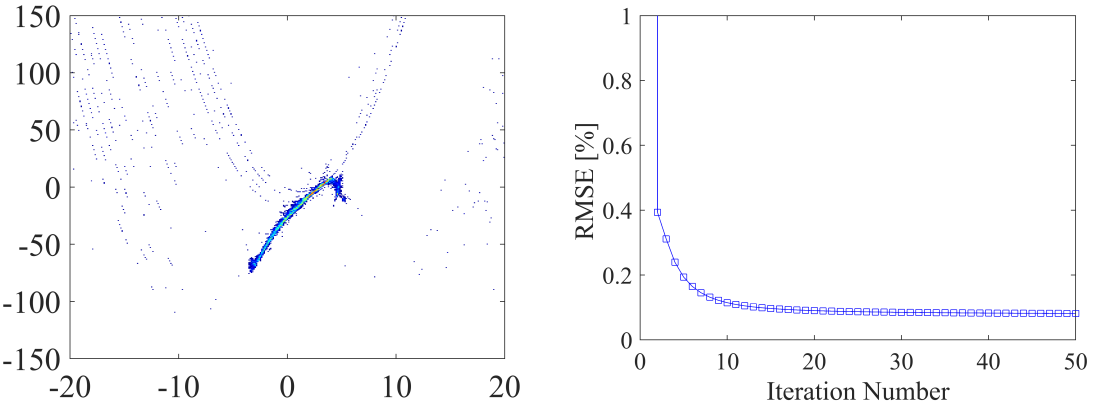

Figure 5.27: (left) Reconstructed LPS from ISRA (right) RMSE between simulated projections and predicted forward projections after 50 iterations.

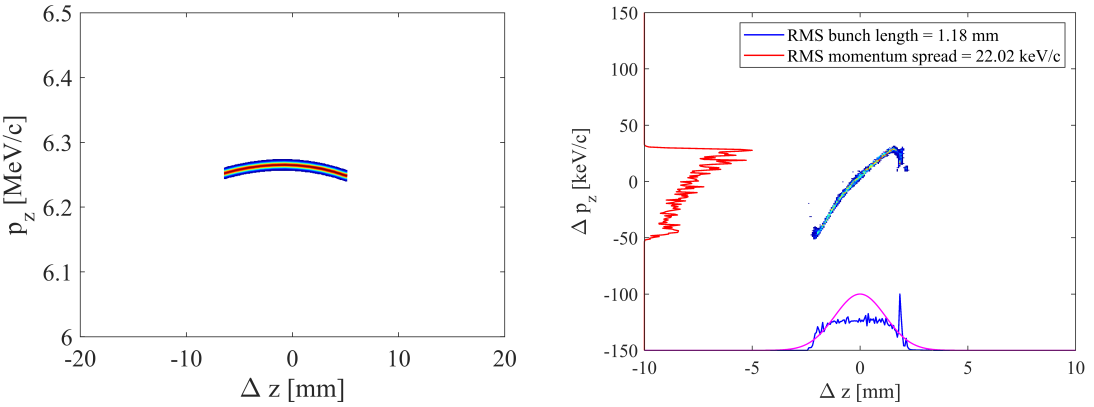

Figure 5.28: (left) Initial LPS form LEDA (right) Reconstructed LPS starting with initial LPS from LEDA.

Finally, the initial matrix was established from LEDA. The noise-like artefacts surrounding the reconstructed LPS were forced to 0. The initial matrix evolves after each iteration, until after 20 iterations, the LPS shape is already formed and then we continue iterations until the changes in LPS become very insignificant. Figure 5.28 shows the results after 50 iterations. The noisy artefacts are removed and even the kink on the right is reproducible. On the left, the kink is not resolvable because of the resolution limitation. The rms bunch length obtained is 1.18 mm which has

only 2.6 % relative difference from simulated bunch length. The rms projected momentum projected spread is 22.02 keV which is only about 4 keV higher than the rms energy spread of the original phase space. If the number of iterations are increased to 200, the LPS becomes more thin but the bunch length and the energy spread values obtained remain similar, see Figure 5.29. Some additional low intensity noise-like pixels start appearing around the reconstructed LPS within the initial matrix region. Also, more ripples start appearing on the flat-top profiles. Generally, 50 iterations are enough to produce noise free and accurate results.

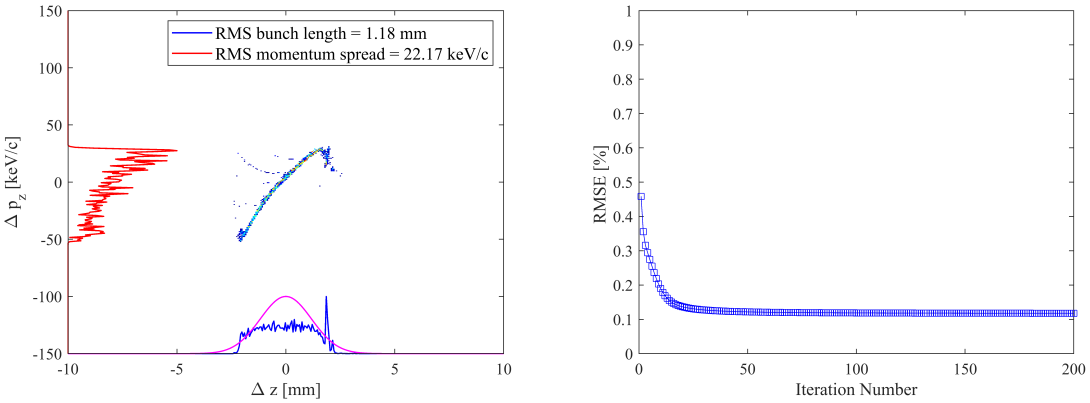

Figure 5.29: Reconstructed LPS (left) starting with uniform positive initial matrix after 200 iterations (b) RMSE after 200 iterations is approx. 0.1 %.

To further prove that the reconstructed LPS of the 250 pC beam, still dominated by space charge effects, cannot be represented by an analytical model without space charge, ISRA algorithm was used to reconstruct the LPS of the beam without slit. Figure 5.30 shows the reconstructed results. It appears that the algorithm placed the weights of the momentum projections in the wrong bins due to inaccurate model. The overall LPS structure does not resemble the true LPS of a 250 pC beam, the rms bunch length is overestimated and the rms momentum spread is almost two times higher.

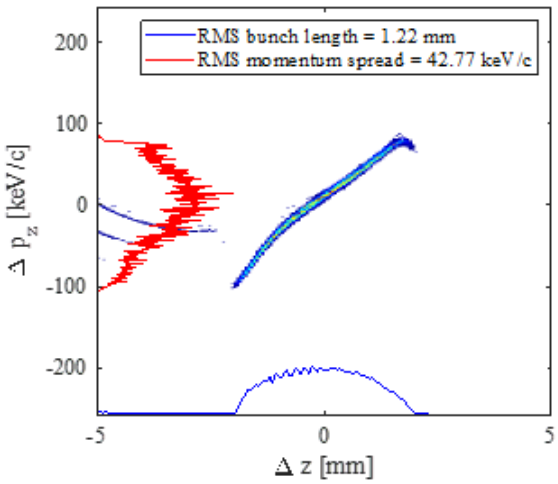

Figure 5.30: LPS reconstructed for 250 pC beam without inserting slit. The weights of the momentum projections are placed in the wrong bins distorting the results.

Additionally, an attempt was made to investigate the slice energy spread of the beam with the slit. The LPS was partitioned into sub-picosecond slices, in this particular case 150 slices. Figure 5.31 shows the slice energy spread in case of 50 and 200 iterations, respectively. The central slice energy spread was about 2 keV/c after 200 iterations, as compared to 1.7 keV/c, found from ASTRA.

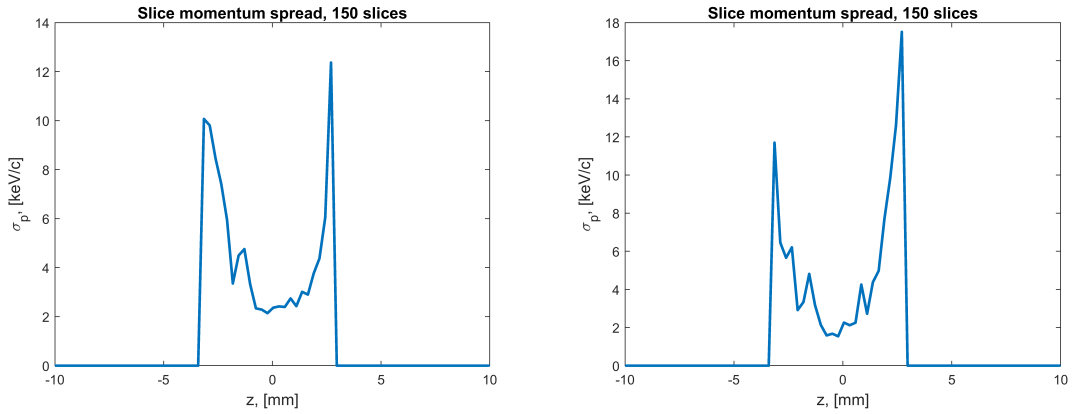

Figure 5.31: Slice energy spread of the 250 pC beam after (left) 50 iterations (right) 200 iterations.

5.5 Momentum measurements for tomography

The momentum p_0 of a reference particle, travelling on a design trajectory and impinging on the vertical center of the observation screen Disp2.Scr1 after the dipole Disp2.D1 (see, Fig. 3.10), can be calculated as [19]:

$$p_0 = eB\rho, \tag{5.20}$$

where e is the electron charge, B is the magnetic field inside the dipole and ρ is the bending radius of the dipole. The vertical coordinates of the other particles in the bunch on the observation screen can be calculated using the following equation [19]:

$$y = y_0 + y_0' L - \delta p \cdot D. \tag{5.21}$$

where y is the particle vertical coordinate on the observation screen, y_0 and y_0' are the particle vertical coordinate and the particle vertical divergence at the dipole entrance, L is the drift length between the dipole exit and the observation screen, $\delta p = (p - p_0)/p_0$ is the particle relative momentum with respect to the ideal reference particle p_0, and $D = 2\rho$ is the dispersion for the 180° dipole magnet, where $\rho = 0.3\,\mathrm{m}$ is the bending radius of this dipole at PITZ. The sign was flipped compared to Eq. 2.31 to keep the same direction of the y axis. The horizontal coordinates of the particles on the observation screen can be calculated from the beam transport through a drift space with length equal to $\pi\rho + L$, see Eq. 2.22.
The first two terms in the right part of the Eq. 5.21 describe the transformation of particle's coordinate after the drift space with length L and define the beam size there. The last term shows a linear dependence of the particles vertical coordinate on the observation screen Disp2.Scr1 on its momentum. The best momentum resolution is achieved if the sum of two first terms is the smallest for all particles, or, in other words, the vertical beam size after a drift with a length L is the smallest. To adjust the momentum resolution, a reference screen High1.Scr5 is installed in the straight section at the same distance L downstream the dipole entrance as the screen Disp2.Scr1 is downstream the dipole exit [47]. The vertical beam size σ_y can be measured there and adjusted by tuning the quadrupole magnets upstream the dipole magnet to have the vertical beam size as small as possible. As a result, the

relative resolution of the momentum measurements can be estimated as:

$$\delta p = \frac{\Delta p}{p} = \frac{\sigma_y}{D}. \tag{5.22}$$

Hence, once the momentum projections of the beam are measured on the y axis of the screen, their mean and rms values are calculated. The booster phase is scanned to find the maximum mean momentum value and the corresponding phase. Typically the beam matching is kept constant for all phases.

This section presents results of longitudinal phase space measurements using the tomographic technique for different temporal laser profiles and electron bunch charges. Tomographic reconstructions were done with the ISRA algorithm that yields the result of the longitudinal phase space upstream the booster cavity. Transverse truncated Gaussian laser with different temporal profiles was used to produce electron bunches. Beam Shape Aperture (BSA) was set depending on to the bunch charge to be extracted. The bunch charge was measured using a faraday cup after the gun. The gun was set to the MMMG phase and the solenoid current was kept corresponding to the minimum projected transverse emittance. Then, the beam was sent through the dipole and the dipole current was adjusted in order to bring the beam to the center of the screen.

5.5.1 Low charge: 10pC beam

Electron beams were generated from the MBI photocathode laser system [35] with a truncated Gaussian transverse distribution. Two different cases of the temporal distributions were considered for the LPS tomography; Gaussian and modulated Gaussian profile. For the case of 10 pC beam charge, the BSA was set to 0.5 mm. Figure 5.32 shows the transverse distribution of the laser at the virtual cathode camera.

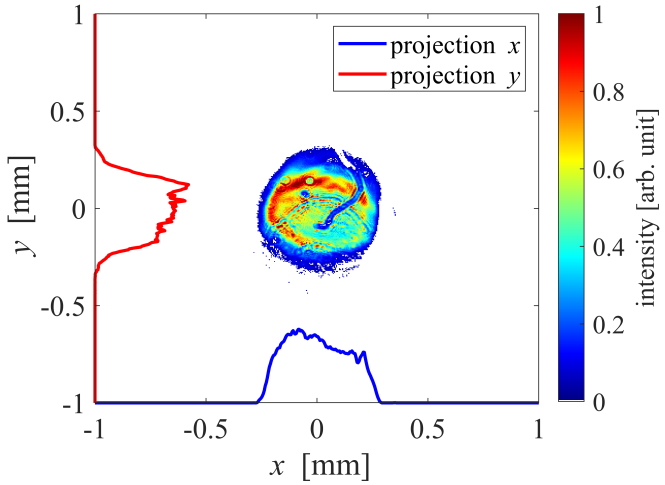

Figure 5.32: Transverse laser profile on the virtual cathode. The iris was set to 0.5 mm, yielding $\sigma_x = 0.136$ mm and $\sigma_y = 0.136$ mm.

Gaussian temporal laser profile

An electron beam of 10 pC charge was generated from the temporal Gaussian distribution by tuning the laser attenuater. The beam was accelerated by the RF gun with the nominal input power settings. Using the dipole in the low energy section, the beam momentum was measured for different gun phases. Beam momentum at the MMMG phase after the LEDA scan was 6.32 MeV/c and the minimum rms momentum spread was 2.40 keV/c. After setting the gun phase to the MMMG phase, the beam was further accelerated downstream using the booster accelerating structure. Then, the beam was focused on High1.Scr5 using two quadrupoles, namely High1.Q5 and High1.Q6, to have minimum vertical rms size as well as good SNR.

After that, the high energy dipole was used to bend the beam and the momentum projections on the Disp2.Scr1 were measured. Figure 5.33 shows the normalized momentum projections corresponding to each booster phase. The area of interest for the beam distribution on the Disp2.Scr1 was set manually in order to fix the momentum range for the tomographic reconstruction.

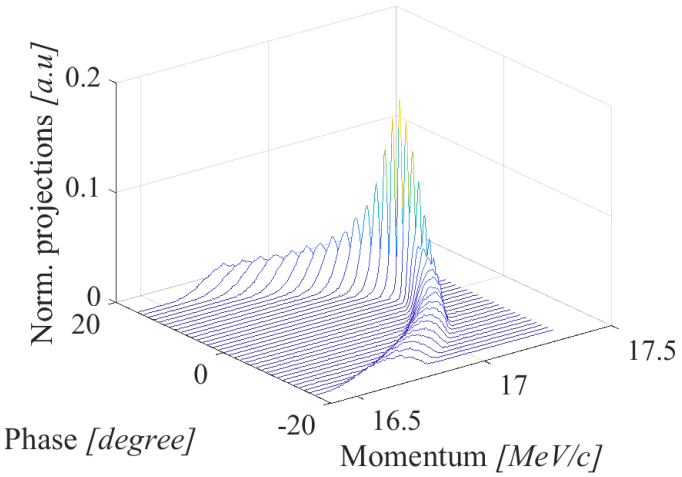

Figure 5.33: Measured projections for 10 pC beam corresponding to booster phase scan for temporal Gaussian profile.

Since in LPS tomography, the initial matrix is estimated from the LEDA scan, the mean momentum and the rms momentum spread measurements corresponding to the various gun phases is also considered, see Figure 5.34 (left). To have a beam with a good resolution and SNR on the low momentum measurement screen, Disp1.Scr1, it was focused using a solenoid and the number of bunches in a pulse train were kept 19. Figure 5.34 (right) shows the mean momentum and the rms momentum spread measurements corresponding to the various booster phases. The MMMG was 17.14 MeV/c at booster phase 119° and the minimum energy spread was 9.28 keV/c at booster phase 121°. The model fits are also shown in the plots. The mean momentum model agrees very well to the measured values. The momentum spread shows good agreement around minimum energy spread. At the off-crest phases, the rms momentum spread appears to be high because of back ground noise in case of 10 pC beam. Figure 5.35 (left) shows the phase advance curve which is smooth indicating that the entire range of energy spread information is covered. This shows

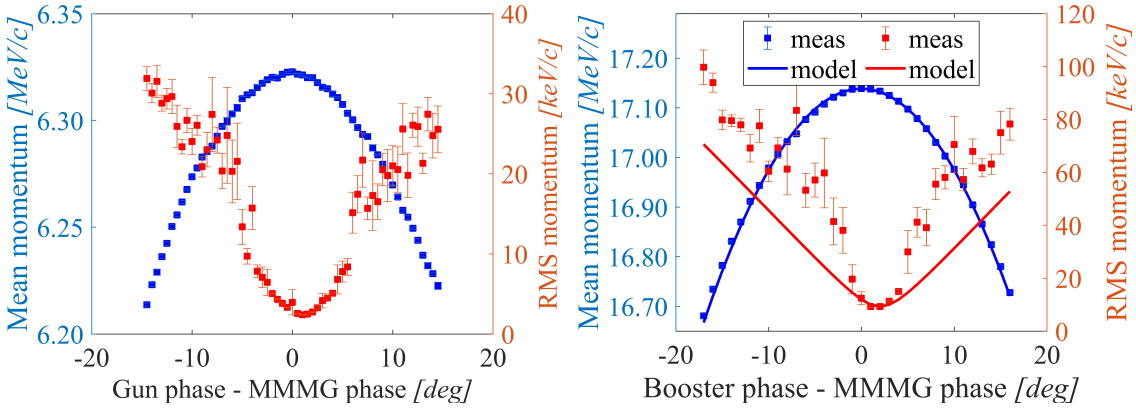

Figure 5.34: (left) Gun phase scan for 10 pC temporal Gaussian laser profile (right) Booster phase scan for 10 pC temporal Gaussian laser with fitted model.

the booster phase range suitable for the LPS tomography. Figure 5.35 (right) shows the sinogram that is fed to the tomography tool for the LPS reconstruction. It shows the intensity map (red being the highest and blue being the lowest) of the momentum values corresponding to the booster phase values. The width of the 90°-rotated cos-like curve is more at the bottom of the plot (approximately between 16.4 MeV and 16.8 MeV), decreases around the MMMG phase (120°) and then again increases towards the off-crest phase at the top of the plot. There are some pixels scattered in the sinogram due to the presence of noise in the measurements. The ratio of this measured sinogram with the predicted forward projection gives the correction factor in the successive iterations.

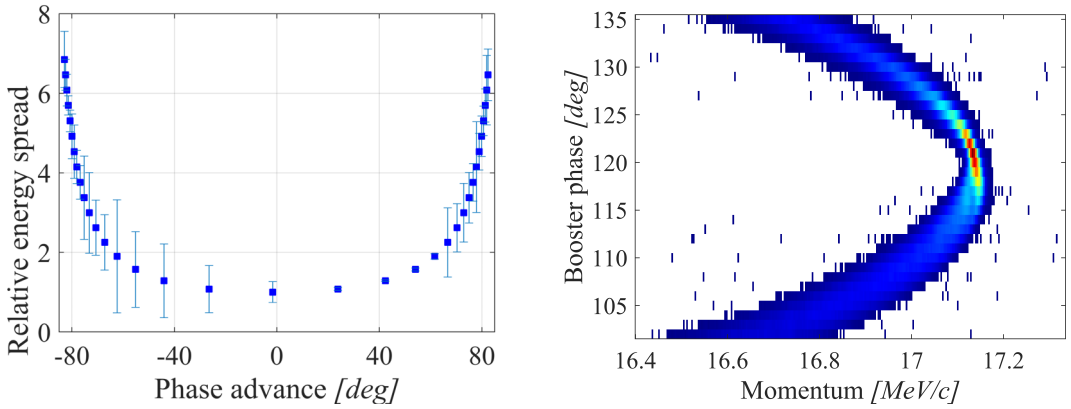

Figure 5.35: (left) Relative energy spread corresponding to the phase advance (right) Sinogram of the 10 pC beam.

The initial matrix for the iterations was obtained from the gun phase scan as already explained in the section on proof-of-principle simulations. The iterations were carried out until the results started to converge and the RMSE was <0.2 %. Figure 5.36 shows the results after 50 iterations using ISRA. The results obtained were noise-free and the bunch length and the energy spread values gave reasonable results. The rms bunch length the energy spread were found to be 0.84 mm and 8.87 keV/c, respectively.

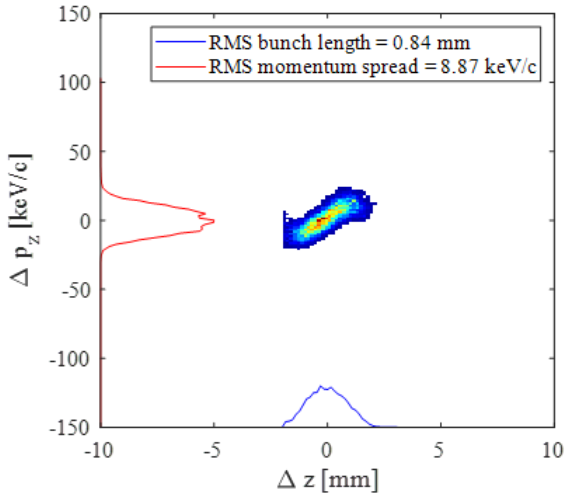

Figure 5.36: Reconstructed LPS of 10 pC beam with temporal Gaussian laser profile.

Modulated gaussian temporal laser profile

Next, a more challenging case of modulated temporal gaussian laser was taken for the LPS tomography. MBI laser was used to generate modulated profile with the help of Lyot filter in the regeneration amplifier. BSA was set to 0.5 mm and a charge of 10 pC was extracted. The gun was set to the MMMG phase after the LEDA scan and transported to the booster. The booster phase was varied after focusing the beam on High1.Scr5 and the momentum projections downstream the dipoles were measured. Figure 5.37 shows all the projections corresponding to the booster phases with clearly visible modulations.

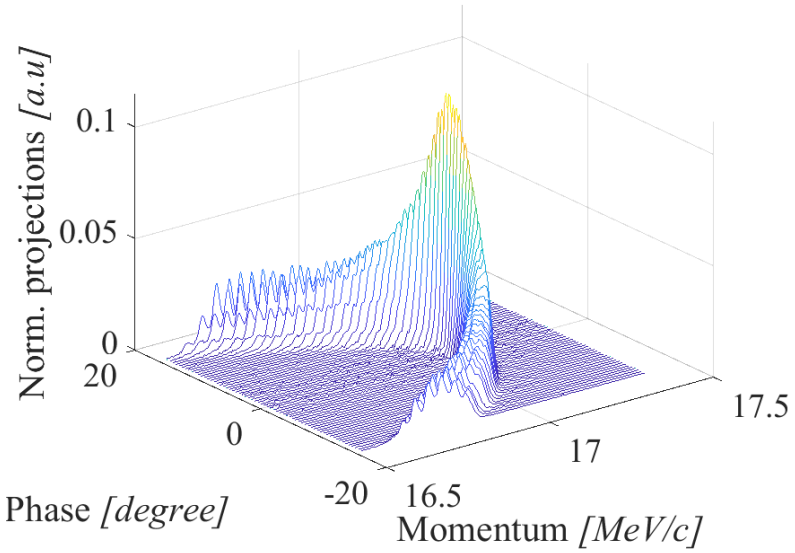

Figure 5.37: Measured projections for 10 pC beam corresponding to booster phase scan for modulated temporal Gaussian profile.

Beam momentum from the LEDA scan is shown in Figure 5.38 (left). The MMMG was found to be 6.35 MeV/c and the minimum rms momentum spread was 2.51 keV/c. Figure 5.38 (right) shows the results of the mean momentum and the momentum spread along with the fitted model. After the booster phase scan, the MMMG and the minimum energy spread phase were found to be 17.1 MeV/c at 119° and 24 keV/c at 121°, respectively. The mean momentum model, like the previous case, fits very well to the measured data, while in the case of the momentum spread model, the measured values oscillate around the modelled curve, giving a reasonable fit. The

energy spread in the data is high with more statistical error as compared to the case of temporal Gaussian laser because of modulations in the beam.

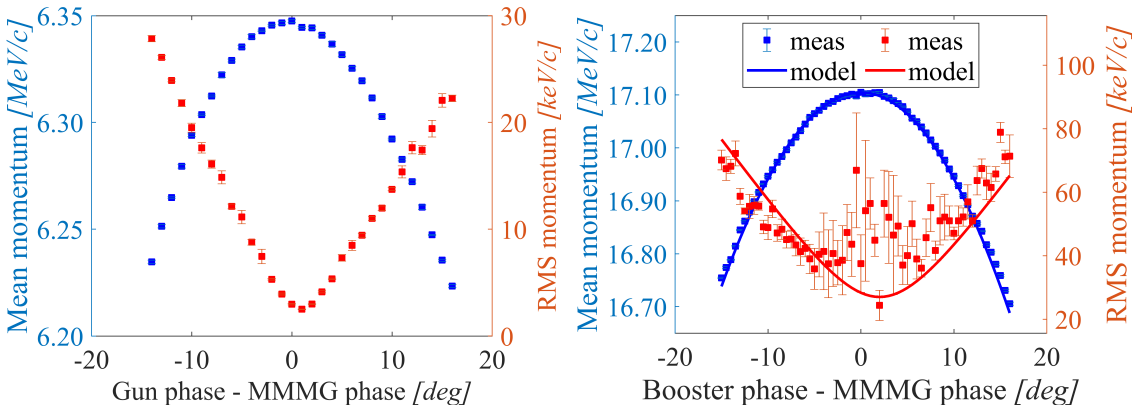

Figure 5.38: (left) Gun phase scan for 10 pC modulated temporal Gaussian laser (right) Booster phase scan for 10 pC modulated temporal Gaussian laser with fitted model.

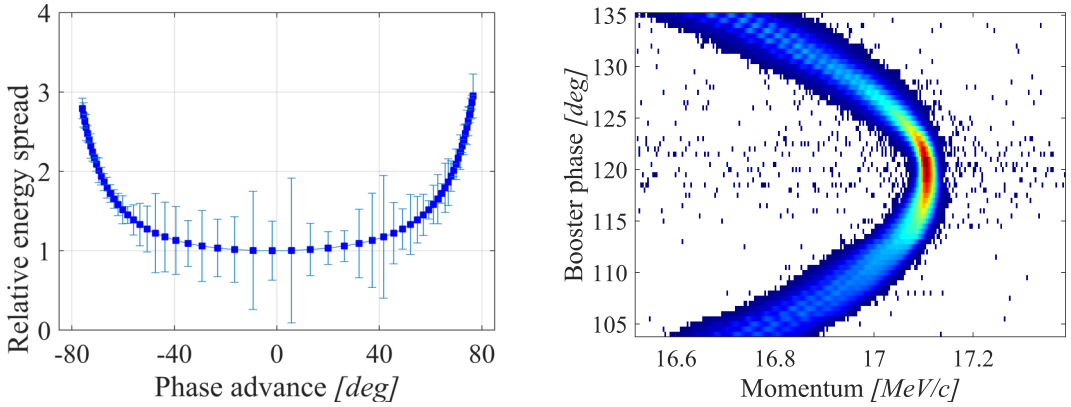

Figure 5.39: (left) Relative energy spread corresponding to the phase advance (right) Sinogram of the 10 pC modulated beam.

Figure 5.39 (left) shows the relative energy spread w.r.t the phase advance. The plot shows a smooth curve with a small step size indicating that the entire range of energy spread information is covered. The booster phase step size was kept approximately 0.5°, in order to retain the information of modulations in the beam. Additinally, the number of pulses were adjusted to have better SNR. Figure 5.39

(right) shows the sinogram that is fed to the tomography tool for the LPS reconstruction of modulated beam. The overall structure of the sinogram is similar to the temporal Gaussian case but the energy spread is comparatively higher owing to the modulated beam.
Again, the initial matrix for the iterations was obtained from the gun phase scan. The iterations were carried out until the results started to converge. Figure 5.40 shows the results obtained from ISRA after 50 iterations. The results obtained were noise-free and the bunch length and the energy spread values gave reasonable results. The bunch length profile shows unambiguous modulations demonstrating the diagnostic capability of the method.

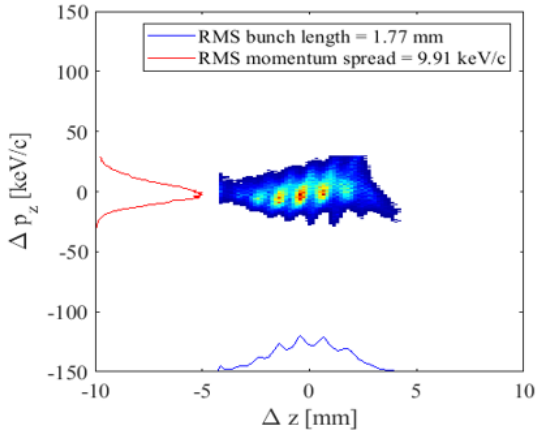

Figure 5.40: Reconstructed LPS of 10 pC beam with modulated temporal Gaussian laser profile.

Additionally, the bunch length was measured using a TDS installed downstream the booster cavity. Since the beam becomes already relativistic after exiting the gun, the bunch length remains the same before and after the booster. This provides an alternate way to find the bunch length and hence check the reliability of the reconstructed LPS. For the TDS installed in the PITZ beamline, the number of pulses can be varied between 1 to 3 because it operates at 3 µs RF pulse length and the laser pulse repetition rate is 1 MHz. The screen used is LYSO [43], since it outputs more light. Usually, the number of pulses used is 3 (maximum) for streaked beam, to have good SNR. Also, the beam is focused before the TDS using a pair of quadrupoles to improve the signal resolution as well as further increase the signal

strength. The TDS phase is adjusted such that the beam remains at the center of the LYSO screen even when the TDS is powered off. This is called the zero crossing phase since it causes no deflection in the beam. Then, the TDS phase is scanned from 3° to 5° in both directions of the zero crossing phase, depending upon the beam position movement on the screen (TDS deflecting voltage). The bunch length is measured across both zero crossing phases [43].
Figure 5.41 (left) shows the bunch length profile of the electron beam generated by the smooth temporal Gaussian laser. The rms bunch length calculated at one zero crossing phase is 0.82 mm and at the other zero crossing phase is 0.81 mm, respectively. Figure 5.41 (right) shows the bunch length profile of the electron beam generated by the modulated temporal Gaussian laser pulses. When the number of bunches in a pulse train was kept 3, the modulations in the bunch profile were less pronounced. Therefore, for this case, the number of pulses was fixed to 1 in order to avoid the saturation of the screen. One can compare the modulations in the bunch length profile obtained from the TDS to the ones obtained from LPS tomography results. The results look promising as they agree quite well.

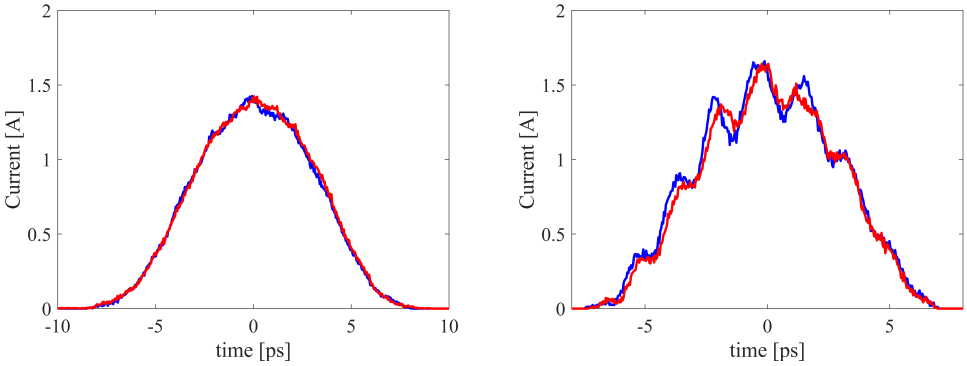

Figure 5.41: Bunch length profile measured using TDS for (left) temporal Gaussian laser (right) temporal modulated Gaussian laser.

From these experimental results, one can conclude that it is possible to reconstruct LPS of low charge beam by LPS tomography. By optimization of the experimental conditions and improvement in the reconstruction algorithm, not only temporal Gaussian profiles can be reconstructed but also complicated profiles like modulated Gaussians can also be determined accurately.

5.5.2 High charge: 250pC beam

The MBI laser system was used to generate a temporal Gaussian laser beam with a transverse truncated Gaussian distribution. To extract a charge of 250 pC, BSA was set to 1.0 mm. Figure 5.42 shows the transverse distribution of the laser pulse at the virtual cathode camera.

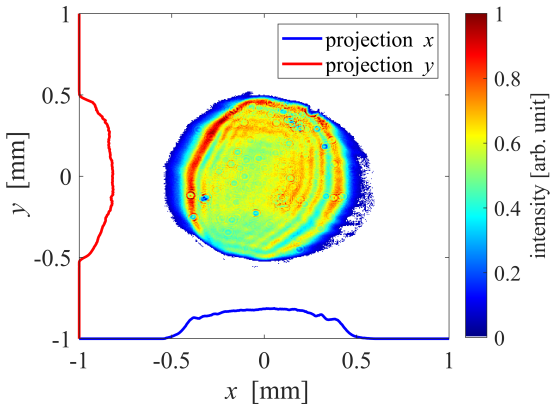

Figure 5.42: Transverse laser profile on the cathode. The iris was set to 1 mm, yielding a horizontal rms size $\sigma_x = 0.2424$ mm and a vertical rms size $\sigma_y = 0.2868$ mm.

Again, the gun was set to the MMMG phase after the LEDA scan and transported to the booster. The booster phase was varied and the momentum projections downstream the dipoles were recorded. Figure 5.43 shows all the projections corresponding to the booster phases. For this case, the gun phase range, booster phase range and the step size were kept such that one can cover both MMMG and the minimum energy spread phase. In contrast to the 10 pC charge, their corresponding phases are by 2° apart and the rms momentum spread is also high at off-crest phases. This is because of the presence of space charge forces which are dominant for 250 pC beam at around 17 MeV/c.

Beam momentum after the gun phase scan is shown in Figure 5.44 (left). The MMMG and the minimum rms momentum spread were found to be 6.43 MeV/c and 8.6 keV/c, respectively. For booster phase scan, the MMMG was found to be 16.79 MeV/c at set point 55° and the minimum energy spread was found to be 11.6 keV/c at set point 60°. The difference between the MMMG phase and the minimum energy spread phase was approximately 5°. Figure 5.44 (right) shows the

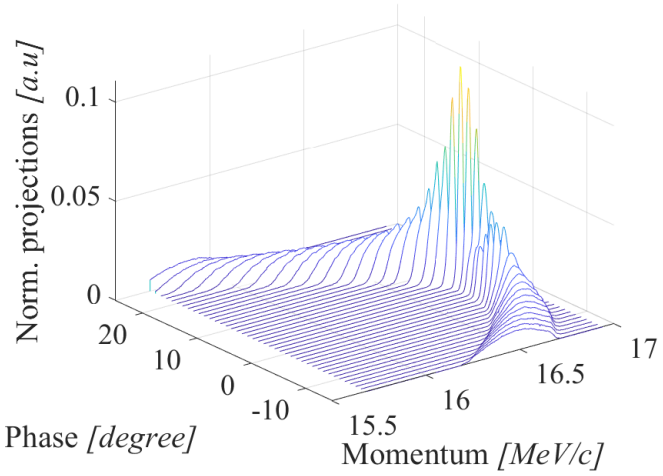

Figure 5.43: Measured p_z projections for 250 pC beam corresponding to booster phase scan for temporal Gaussian profile.

results of the mean momentum and the momentum spread along with the fitted model. Again, the mean momentum model fits very well to the measured data, while in the case of the momentum spread model, the measured values show higher energy spread. Since the space charge effects are not incorporated in the LPS model, the momentum spread values are underestimated.

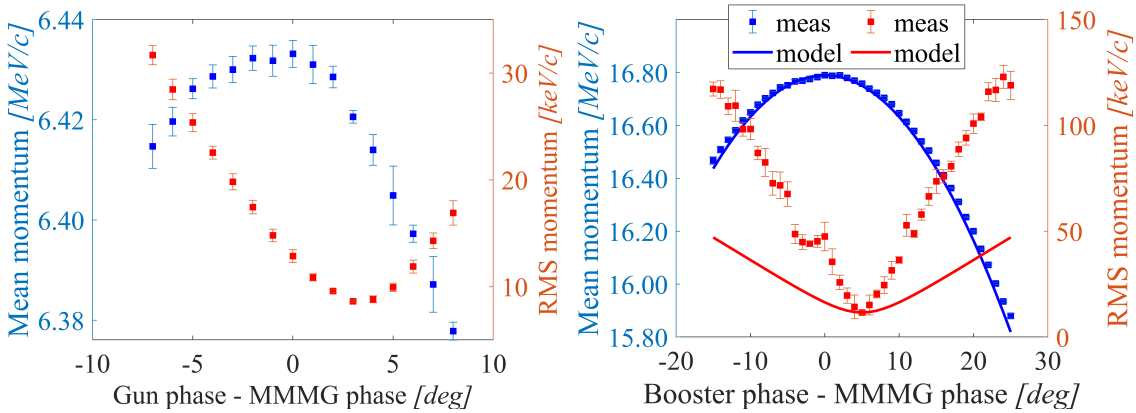

Figure 5.44: (left) Gun phase scan at LEDA for 250 pC temporal Gaussian laser, (right) Booster phase scan at HEDA1 with fitted model.

In order to strongly reduce the space charge forces, a slit at the location of Low.Scr1, at a distance of 0.8 m from the cathode, was inserted in the transverse plane. From simulations, the results looked promising. The same procedure was adopted in the experiment. Figure 5.45 (left) shows the 3D model of the slit at the location of Low.Scr1. The chopped beam was then observed on Low.Scr3 located downstream the slit, at a location of 1.71 m from the cathode, see Figure 5.45 (right). The charge of this beam measured by a faraday cup, also at Low.Scr3 location, was approximately 10 pC.

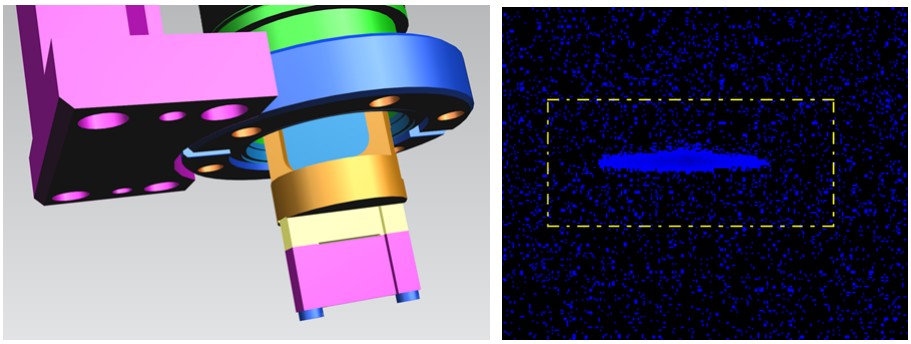

Figure 5.45: (left) 3D model of the 200 µm-wide vertical slit at the location of Low.Scr1, z = 0.8 m. (right) Beam at Low.Scr3, z = 1.71 m after the slit.

Once again the booster phase was varied. The MMMG after the booster was found to be 16.84 MeV/c at set point 56.6° and the minimum energy spread was 20.4 keV/c at set point 58.1°. Now the difference between the MMMG phase and the minimum energy spread phase was reduced to 1.5° indicating a significant reduction of the space charge effect. On the other hand, the minimum energy spread was increased almost by a factor of 2. Therefore, some additional tuning was done to improve the momentum resolution. For every booster phase, the quadrupoles (High1.Q6 and High1.Q7) were tuned in order to have the minimum vertical beam size at the reference screen, i.e. High1.Scr5 and their corresponding values were saved. Then the booster phase was varied, the saved quadrupole values were updated and the momentum projections were measured. The momentum resolution improved by 5 keV/c and the phase difference between MMMG phase and minimum energy spread phase further reduced to 0.5°, see Figure 5.46. Table 5.1 summarizes the values of MMMG and the minimum energy spread and their phases, respectively.

Table 5.1: Comparison of 250pC beam for different experimental cases

Case Charge (pC) + slit	$\langle p_z \rangle^{max}$ **phase** $(degree)$	σ_p^{min} **phase** $(degree)$	$\langle p_z \rangle^{max}$ (MeV)	σ_p^{min} (keV)
250	55	60	16.8	11.6
250 + slit	56.6	58.1	16.8	20.4
250 + slit + tuning	57	57.5	16.9	14.9

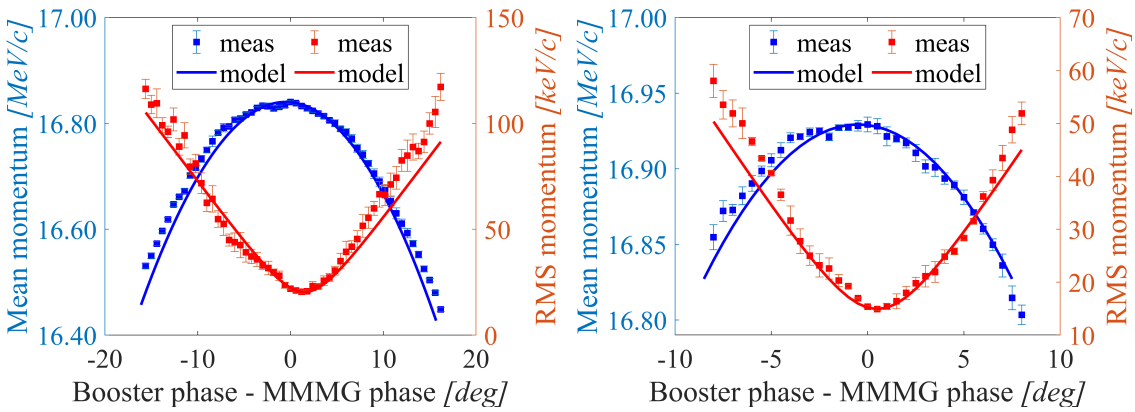

Figure 5.46: (left) Booster phase scan for 250 pC beam with slit (right) Booster phase scan for 250 pC beam with slit and tuned quadrupoles. The minimum energy spread resolution is improved by 5 keV.

The additional advantage of this method is that the booster phase range to be scanned is significantly reduced. One can plot the phase advance w.r.t the booster phase and observe that the phase advance already reaches 80° around booster phase 10° and starts to saturate as shown in Figure 5.47 (left). The relative energy spread also starts to saturate at the phase advance value of 80° as shown in Figure 5.47 (right).

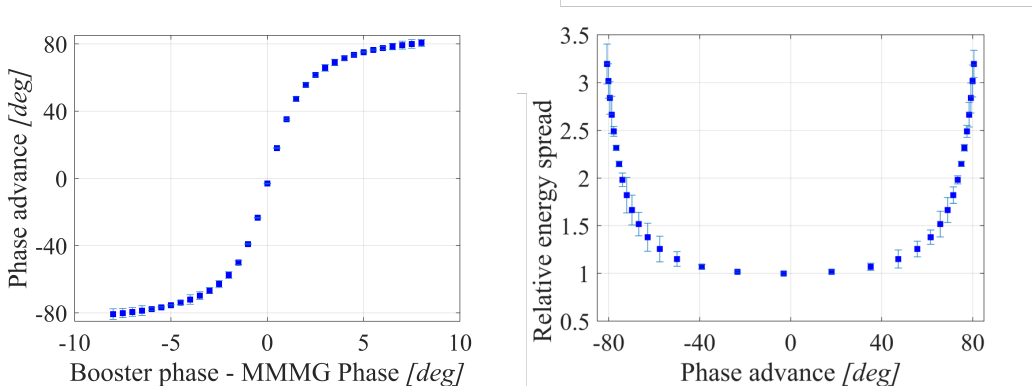

Figure 5.47: (left) Phase advance corresponding to the booster phase scan (right) Relative energy spread corresponding to the phase advance.

For the iterative reconstruction, as a first step, the initial estimate $\vec{x}^k$ was taken as a uniform vector of 1s. The results of first 50 iterations from ISRA are shown in Figure 5.48. The rms bunch length was calculated to be 1.46 mm and the rms energy spread was calculated to be 16.97 keV/c. The results obtained are converging and with few noise-like artefacts. In the next step, the initial estimate for the iterations was obtained from the gun phase scan. Figure 5.49 (left) shows the results after 50 iterations. The artefacts are almost removed and the overall structure is similar to the uniform initial estimate case. The initial estimate from LEDA not only removes the noise but also impacts the overall distribution of particles in phase space. One can compare the rms bunch length and the energy spread values of the reconstructed LPS to note this effect. The rms bunch length was reduced to 1.13 mm and the rms energy spread was reduced to 12.65 keV/c. The energy spread of the Gaussians distributions in the initial guess were kept 50 keV/c. Note, that if the energy spread of the initial guess is underestimated, a part of the actual LPS would be forced to be 0. Figure 5.49 (right) shows the case where the energy spread of the initial estimate was kept 10 keV/c and hence part of the LPS was cut. These results were also obtained after 50 iterations.

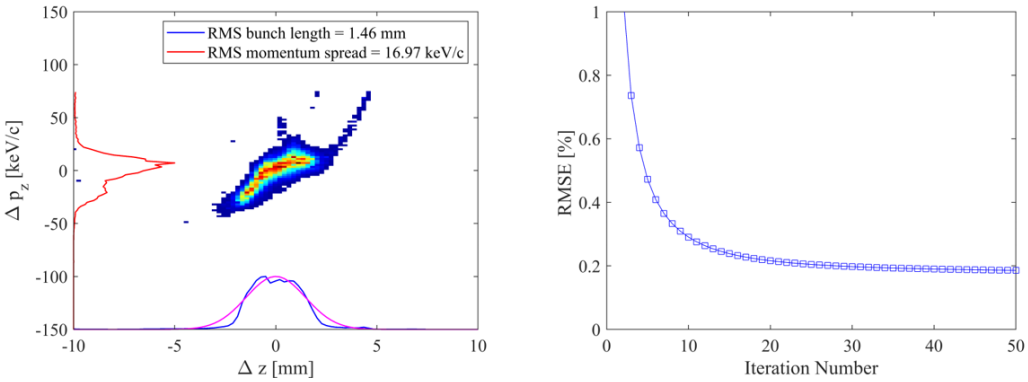

Figure 5.48: (left) Reconstructed LPS with uniform positive initial matrix. The purple line is the Gaussian fit of the bunch length profile. (right) RMSE after 50 iterations is around 0.2 %.

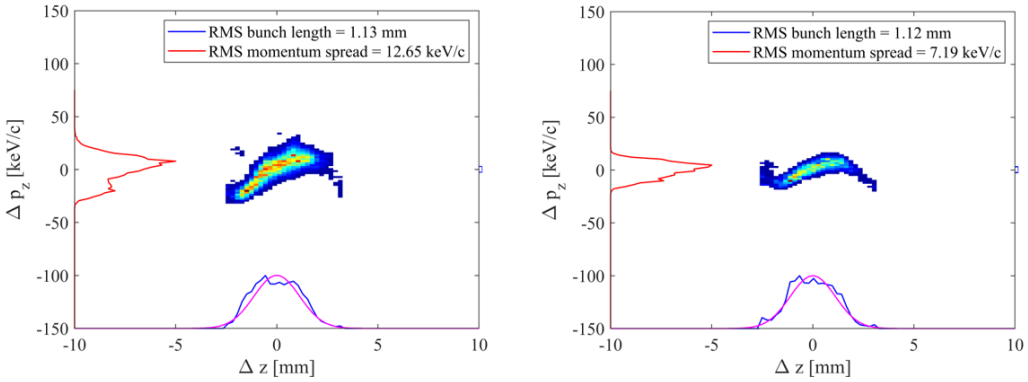

Figure 5.49: (left) Reconstructed LPS with initial estimate from LEDA with 50 keV energy spread. The purple line is the Gaussian fit of the bunch length profile. (right) Reconstructed LPS with initial estimate from LEDA with 10 keV energy spread. The purple line is the Gaussian fit of the bunch length profile.

Since we know the dipole introduces additional energy spread in the beam, an attempt was made to reconstruct the LPS after removing this energy spread. The momentum projections were deconvoluted with the High1.Scr5 y projection which reduced the energy spread introduced by the dipole. Again, starting from the initial matrix from the gun phase scan, 50 iterations were carried out. Interestingly, the rms bunch length and the energy spread results were comparable to the ones obtained by the LPS reconstructed without deconvoluted momentum projections. But, the rms error decreased to <0.1 % as the difference between the deconvoluted measured projections and the predicted forward projections further reduced. The results are shown in Figure 5.50. Hence, one can conclude that the ISRA algorithm, together with the initial well-defined estimate from the gun phase scan, gives reliable results with monotonic convergence even without deconvoluted momenta.

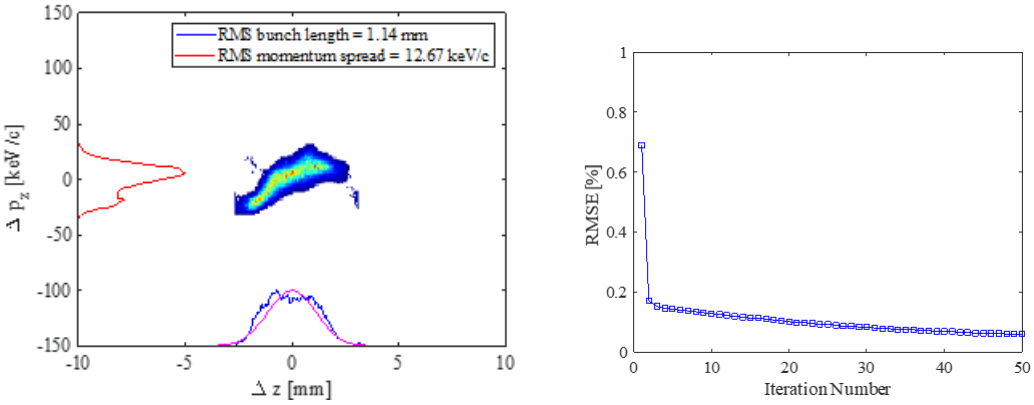

Figure 5.50: (left) Reconstructed LPS after deconvolving momentum projections with High1.Scr5 y projection. The purple line is the Gaussian fit of the bunch length profile. (right) RMSE after 50 iterations is less than 0.1 %.

Again, one can compare the bunch length profiles obtained from the reconstructed LPS with the profiles measured from the TDS. Figure 5.51 (left) shows the bunch length of 250 pC beam across both zero crossing phases. They are Gaussian-like with slightly different distribution depending upon the shear parameter. The rms bunch length was calculated to be 1.473 mm and 1.983 mm, respectively. Figure 5.51 (right) shows the bunch length profile of the truncated beam across both zero crossing phases. The rms bunch length at the zero crossing phases were calculated to be 1.34 mm and 1.64 mm. Both the profiles have a flat-top, similar to what was

observed in the x projection of the reconstructed LPS. The Gaussian fit on the flat-top profiles obtained from the reconstructed LPS are comparable to the bunch length profiles of the non-truncated beam measured by the TDS.

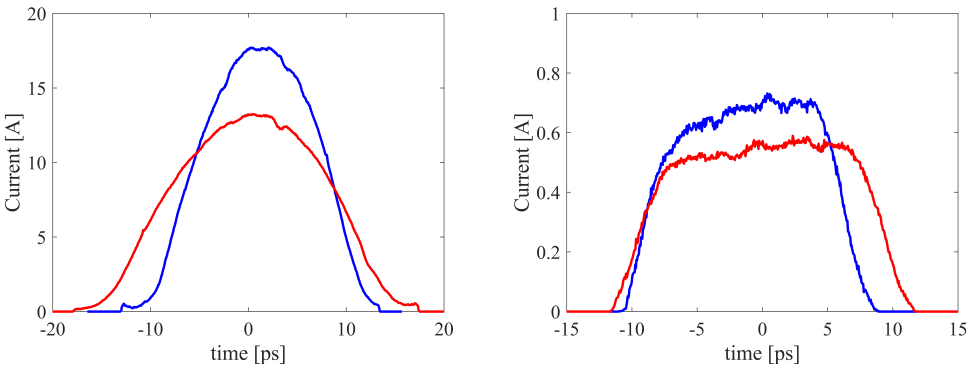

Figure 5.51: Bunch length profile measured using TDS for (left) 250 pC beam charge (right) 250 pC beam truncated by slit.

From these experimental results, one can conclude that it is possible to reconstruct LPS of 250 pC beam by LPS tomography, but under special experimental conditions. Since the analytical model of the LPS does not include the space charge forces, one can attempt to significantly reduce them in experiment by truncating the beam with a slit in the non-dispersive plane. The experimental results are also consistent with the simulation results.

5.6 Summary

LPS infront of the booster is reconstructed at PITZ by tomography [19]. In this method, the booster phase is varied and the measured momentum projections are fed to an iterative algorithm. The iterations are carried out until the results converge. Previously this was done at PITZ by using ART. Although ART is simple to implement with a good convergence speed, the results showed many artefacts and hence overestimated the energy spread and the bunch length. The aim of this work was to optimize the experimental procedure to obtain data for tomography as well as update the reconstruction algorithm to have noise free and reliable results without applying any charge cuts.

In the scope of this thesis work, some core concerns were addressed e.g. booster phase scan range, momentum resolution and space-charge effects. First, an analytical model was developed to quantify the rms energy spread, bunch length and the phase advance. With the LPS chirp and the bunch length estimated from the model, the phase advance was determined. Phase advance analysis identified the booster phase range and the step size to be used for obtaining the momentum projections. In the experimental procedure, the signal resolution of these projections was improved by careful beta function control at the reference screen of the momentum measurements. For the case of 250 pC, a slit before the booster was used to reduce the space charge effects. The reconstruction method was updated from ART to ISRA which showed promising results owing to its assurance of non-negative solution. The weight matrix that is crucial for the successive updates in the iterations was improved by bilinear interpolation. To cater the noisy artefacts that are inherent in tomography, an initial scientific presumption of LPS from the low energy section momentum measurements was established. The aforementioned modifications resulted in reduced noise-like artefacts, better convergence speed and more accurate results. After the methodical studies on the simulations, the technique was applied to the experimental data for 10 pC and 250 pC beam. Experiment with modulated laser beam was also designed that successfully demonstrated the diagnostic capability.

Chapter 6

Conclusion and outlook

High brightness photoinjector is a key component of a brilliant light source. Free electron lasers need coherent electrons with a small 6D phase space. This means that the electrons should have small transverse emittance, small energy spread and high peak current. FLASH and XFEL are such user facilities that serve to provide short intense radiation. The electron sources of these facilities are developed, conditioned and characterized at the Photoinjector Test facility at DESY in Zeuthen (PITZ). Basically PITZ characterizes the electron guns at the working point of these facilities, i.e., 250 pC bunch charge and 6.3 MeV/c beam energy. The characterization of both transverse and longitudinal phase space is crucial to optimize the beam in a photoinjector.

To characterize the beam in the transverse phase space, PITZ utilises single slit scanning technique [17, 40]. Usually the solenoid current is varied within a certain range to find the minimum emittance point corresponding to the horizontal and vertical phase space $\epsilon_{xy} = \sqrt{\epsilon_x \epsilon_y}$. It was observed at PITZ, that the beam was asymmetric in the transverse plane after the gun. Also, the horizontal and vertical phase spaces and their corresponding emittance numbers were not the same indicating coupling. In order to find the 4D transverse phase space, virtual pepper pot technique was developed and successfully tested on simulation as well as experimental data. It enabled to find ϵ_{4D} and reconstruct 4D transverse phase space. It was found that the source of rise in emittance comes from the cross planar coupling and in order to remove or minimize it, the optimum approach would be to fine tune the quadrupoles' current. As a next step, the tuning of number of bunches for each slit

position during the slit scan is planned to improve the signal to noise ratio. This can enable reconstruction of phase space halo without resorting to any charge cut methodology. Also, additional simulations with gun quadrupoles can be done to have conditions comparable to experiments.

At PITZ, the LPS after the gun is characterized by tomography [19], which requires no additional infrastructure like a TDS. But the space charge dominated nature of the beam poses a challenge for this method. Similar to the TPS reconstruction technique, inserting a slit can reduce the space charge forces, and since it is in the non-dispersive plane, the overall structure of the LPS is not affected. After developing an analytical model for LPS, the method was tested on simulations as well as the experimental data. It gave insight to the LPS phase advance and the importance of reconstruction algorithm. The simulation and the experimental results showed good agreement exhibiting the successful implementation of the methodology [73], which was further verified by the TDS measurement. However, LPS tomography should be further explored for an accurate measurement of the slice energy spread, since it is perturbed when the local charge density is modulated after inserting the slit. Owing to the vast interest of the FEL community in slice energy spread, as a next step, it is planned to improve the mean momentum model by either including the space charge effect [74] or by a physics informed machine learning model [75]. This would eradicate the need to insert a slit after the gun, enabling reliable measurement of the slice energy spread.

Appendix A

2D charge cut

The normalized integrated charge cut corresponding to the normalized weights of the projection was investigated. To quantify how much charge is cut in the projection of the EMSY1 distribution because of noise, the procedure described below was adopted.

- the EMSY1 x and y intensity distribution is cut into n intervals. Figure A.1 shows that the EMSY1 x projection is divided into 14 intervals.

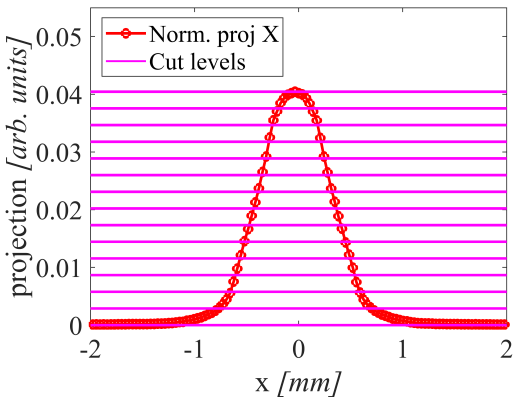

Figure A.1: EMSY1 x projection divided into 14 intervals.

- the integral of projection below i^{th} level is taken to yield Q_x. Figure A.2 (left) shows integrated charge normalized by the total charge Q_o. When the ratio Q_x/Q_o is unity, there is no charge lost.

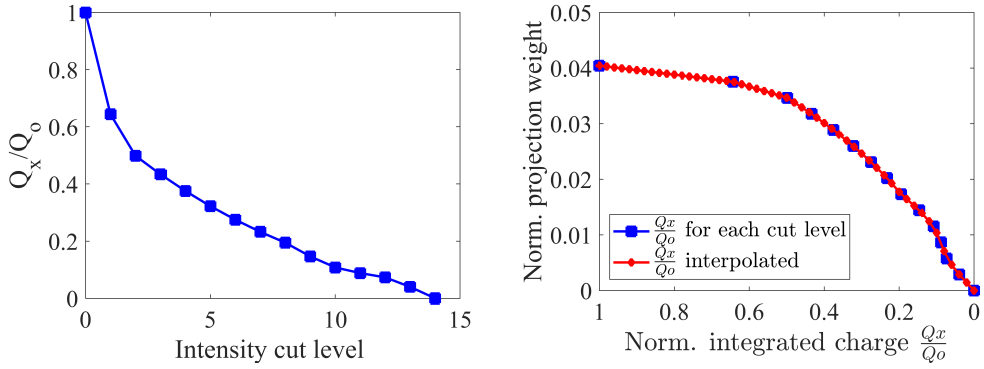

Figure A.2: (left) Normalized integrated charge corresponding to each cut level. (right) Normalized intensity of the projection corresponding to normalized integrated charge.

- The weights of the normalized projection corresponding to the normalized integrated charge are plotted to indicate which part of the EMSY1 distribution contributed to the beamlets. The points are interpolated to yield better estimate as shown in Figure A.2 (right).
- From the normalized integrated charge, one can then find the charge cut on the projection as shown in Figure A.3 (left). A comparison plot (right) is also shown to indicate how much projection was lost (put to 0) .

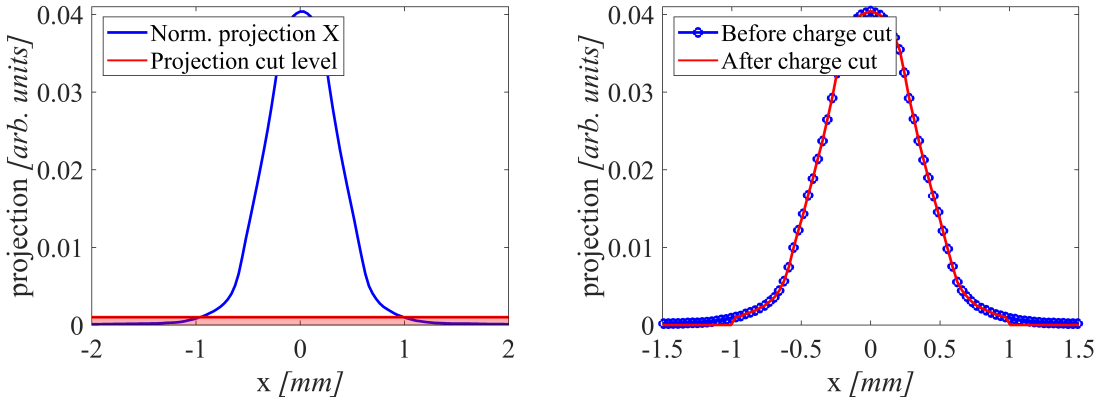

Figure A.3: (left) Part of the tail that is cut because of noise (right) Comparing EMSY1 projection before and after charge cut.

Appendix B

Systematic error in momentum measurements

For the on-crest phase, beam travels exactly through the center of the dipole and hence there is no dispersion from the dipole. The deviation of the beam trajectories in the dipole for the off-crest phases causes systematic error in the measurement. To quantify this deviation, the beam charge was tuned to 10 pC and the booster phase was set to the minimum energy spread phase. Then the beam was scanned on the dispersion screen Disp2.Scr1 by varying the dipole current.

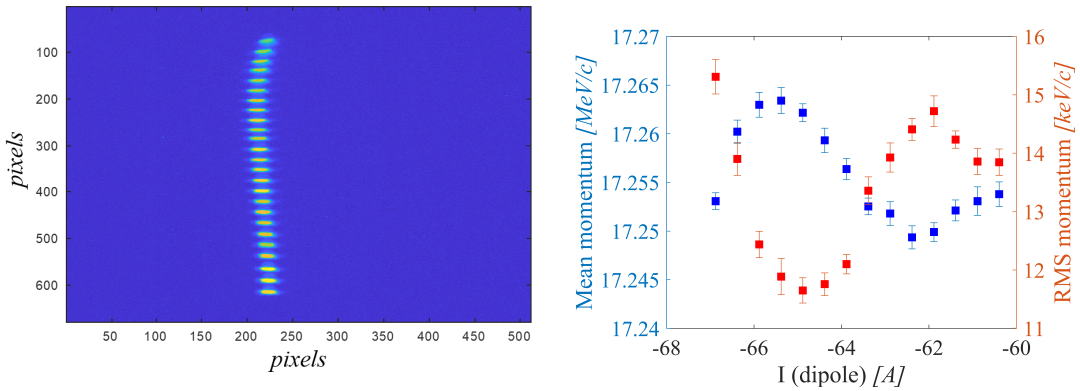

Figure B.1: (left) Beam distribution on the momentum measurement screen Disp2.Scr1. (right) Mean momentum and rms momentum of 10 pC beam at booster's minimum energy spread phase for different dipole currents from pixel 300 to 500.

Figure B.1 (left) shows the superimposed beam images for various dipole currents

as the beam traverses the screen. The beam images appear to be slightly tilted and horizontally displaced, with more dispersion at the start of the screen (till pixel number 200; see y axis) and then the beam distribution becomes more consistent towards the end of the screen (till pixel number 600). Figure B.1 (right) shows a plot of the mean momentum and momentum spread for the beam images in the central part of the screen (pixel 300 to 500 on y scale) since the beam is generally scanned in this region for the momentum measurements in case of low charge beams. The peak to peak deviation of these values was calculated. The number of pulses were tuned for each dipole current in order to have good signal-to-noise ratio. In this particular case, Δp_z and $\Delta\sigma_p$ were estimated to be 14.1 keV/c and 3.66 keV/c, respectively.

Ideally, during the booster phase scan to measure the momentum projections, the dipole current should be adjusted for each booster phase to bring the beam to the center of the screen, in order to minimize or eliminate the systematic error. This will give accurate estimation of mean momentum and momentum spread. Changing the dipole current also changes the momentum calibration of the screen for every measurement. Since in LPS tomography, one of the requirement is to keep the momentum range fixed, this measurement method is not suitable for our case.

Acknowledgment

My research work started in 2020, with the corona pandemic, and everything was a challenge for the PITZ team, from running accelerator to interaction with the colleagues and discussions with supervisors. I sincerely thank the whole PITZ team who continued the work despite all the challenges and helped me achieve my goal.
First of all, I would like to express my sincere gratitude to my supervisor Mikhail Krasilnikov for his support throughout my PhD tenure. I particularly appreciate his many good ideas, and am grateful for his close supervision, which allowed me to analyse scientific questions in great depth. I would also like to thank my professor, Wolfgang. His reviews always helped me to keep my timeline and work progress in check. I thank Houjun and Xiangkun for their co-supervision, pointing out what was lacking in my thesis and cross-checking my results.
I would like to extend special thanks to my group leader, Frank, who was very supportive and encouraged regular talks in PITZ physics seminars for fruitful discussions. He was generous in sending me to workshops and conferences, and facilitating my stay at PITZ, despite the overall political critical situation.
I would like to thank many people at PITZ specially Anne, Matthias, Grygorrii and other PITZ members and technical team who keep the accelerator up and running. I appreciate the exchange of ideas with all fellow PhDs and post-docs. I thank Raffael for teaching me screen alignment and helping me countless times with ASTRA and Matlab coding. I also want to thank Chris for thoroughly checking my thesis and critically looking into the results.
I learnt something from everyone at PITZ, specially while doing shifts and operating the machine for various measurement programs. PITZ connected me with an extraordinary accelerator scientific community and I look forward to continue working here.

Eidesstattliche Versicherung/Declaration on oath

Hiermit versichere ich an Eides statt, die vorliegende Dissertationsschrift selbst verfasst und keine anderen als die angegebenen Hilfsmittel und Quellen benutzt zu haben.
Die eingereichte schriftliche Fassung entspricht der auf dem elektronischen Speichermedium.
Die Dissertation wurde in der vorgelegten oder einer ähnlichen Form nicht schon einmal in einem früheren Promotionsverfahren angenommen oder als ungenügend beurteilt.

Zeuthen, den 18. Dezember 2023

Namra Aftab

References

[1] S. Dierker, U. Bergmann, J. Corlett, R. Falcone, J. Galayda, M. Gibson, J. Hastings, B. Hettel, J. Hill, Z. Hussain, *et al.*, "Science and technology of future light sources," tech. rep., Brookhaven National Lab.(BNL), Upton, NY (United States), 2008.

[2] F. Elder, A. Gurewitsch, R. Langmuir, and H. Pollock, "Radiation from electrons in a synchrotron," *Physical Review*, vol. 71, no. 11, p. 829, 1947.

[3] J. Feikes, K. Holldack, P. Kuske, and G. Wüstefeld, "Sub-picosecond electron bunches in the bessy storage ring," *EPAC04, Lucerne, Switzerland*, 2004.

[4] A. Zholents and M. Zolotorev, "Femtosecond x-ray pulses of synchrotron radiation," *Physical Review Letters*, vol. 76, no. 6, p. 912, 1996.

[5] D. A. Deacon, L. Elias, J. M. Madey, G. Ramian, H. Schwettman, and T. I. Smith, "First operation of a free-electron laser," *Physical Review Letters*, vol. 38, no. 16, p. 892, 1977.

[6] P. Schmüser, M. Dohlus, J. Rossbach, and C. Behrens, "Free-electron lasers in the ultraviolet and x-ray regime," *Springer Tracts in Modern Physics*, vol. 258, 2014.

[7] J. Andruszkow, B. Aune, V. Ayvazyan, N. Baboi, R. Bakker, V. Balakin, D. Barni, A. Bazhan, M. Bernard, A. Bosotti, *et al.*, "First observation of self-amplified spontaneous emission in a free-electron laser at 109 nm wavelength," *Physical Review Letters*, vol. 85, no. 18, p. 3825, 2000.

[8] P. Emma, R. Akre, J. Arthur, R. Bionta, C. Bostedt, J. Bozek, A. Brachmann, P. Bucksbaum, R. Coffee, F.-J. Decker, *et al.*, "First lasing

and operation of an ångstrom-wavelength free-electron laser," *nature photonics*, vol. 4, no. 9, pp. 641–647, 2010.

[9] H. Weise, W. Decking, *et al.*, "Commissioning and first lasing of the european xfel," *Proc. FEL'17*, pp. 9–13, 2017.

[10] E. Prat, R. Abela, M. Aiba, A. Alarcon, J. Alex, Y. Arbelo, C. Arrell, V. Arsov, C. Bacellar, C. Beard, *et al.*, "A compact and cost-effective hard x-ray free-electron laser driven by a high-brightness and low-energy electron beam," *Nature Photonics*, vol. 14, no. 12, pp. 748–754, 2020.

[11] W. Decking, S. Abeghyan, P. Abramian, A. Abramsky, A. Aguirre, C. Albrecht, P. Alou, M. Altarelli, P. Altmann, K. Amyan, *et al.*, "A mhz-repetition-rate hard x-ray free-electron laser driven by a superconducting linear accelerator," *Nature photonics*, vol. 14, no. 6, pp. 391–397, 2020.

[12] Y. Chen, F. Brinker, W. Decking, M. Scholz, L. Winkelmann, and Z. Zhu, "Virtual commissioning of the european xfel for advanced user experiments at photon energies beyond 25 kev using low-emittance electron beams," in *Journal of Physics: Conference Series*, vol. 2420, p. 012026, IOP Publishing, 2023.

[13] E. J. Jaeschke, S. Khan, J. R. Schneider, and J. B. Hastings, *Synchrotron light sources and free-electron lasers: accelerator physics, instrumentation and science applications*. 2016.

[14] E. Schneidmiller, M. Yurkov, M. Krasilnikov, and F. Stephan, "Tunable ir/thz source for pump probe experiments at the european xfel," in *Advances in X-ray Free-Electron Lasers II: Instrumentation*, vol. 8778, pp. 151–156, SPIE, 2013.

[15] F. Stephan, M. Gross, A. Grebinyk, Z. Aboulbanine, Z. Amirkhanyan, V. Budach, V. H. Ehrhardt, A. Faus-Golfe, M. Frohme, J.-F. Germond, *et al.*, "Flashlab@ pitz: New r&d platform with unique capabilities for electron flash and vhee radiation therapy and radiation biology under preparation at pitz," *Physica Medica*, vol. 104, pp. 174–187, 2022.

[16] L. Staykov, "Characterization of the transverse phase space at the photo-injector test facility in desy, zeuthen site," 2012. Universität Hamburg, Dissertation, https://bib-pubdb1. desy.de/record/85111 ,(2008).

[17] G. Vashchenko, "Transverse phase space studies with the new cds booster cavity at pitz," 2013. Universität Hamburg, 10.3204/DESY-THESIS-2013-043, (2013).

[18] H. Qian, M. Krasilnikov, A. Lueangaramwong, X. Li, O. Lishilin, Z. Aboulbanine, G. Adhikari, N. Aftab, P. Boonpornprasert, G. Georgiev, *et al.*, "Slice energy spread measurement in the low energy photoinjector," *Physical Review Accelerators and Beams*, vol. 25, no. 8, p. 083401, 2022.

[19] D. Malyutin, "Time resolved transverse and longitudinal phase space measurements at the high brightness photo injector pitz," tech. rep., Deutsches Elektronen-Synchrotron (DESY), 2014.

[20] R. Niemczyk, *Subpicosecond-resolved emittance measurements of high-brightness electron beams with space charge effects at PITZ*. PhD thesis, Staats-und Universitätsbibliothek Hamburg Carl von Ossietzky, 2021.

[21] H. Wiedemann, *Particle accelerator physics*. Springer Nature, 2015.

[22] K. Wille, *The physics of particle accelerators: an introduction*. Clarendon Press, 2000.

[23] M. Ferrario, M. Migliorati, and L. Palumbo, "Space charge effects," *arXiv preprint arXiv:1601.05214*, 2016.

[24] M. Ferrario, M. Migliorati, and L. Palumbo, "Beam instabilities in linear machines: Wakefields effects," *CERN Yellow Reports: School Proceedings*, vol. 3, pp. 165–165, 2017.

[25] E. Prat, "Spurious dispersion effects at flash," Jul 2009. Universität Hamburg, Dissertation, 10.3204/DESY-THESIS-2009-026, (2009).

[26] F. Stephan, "Photo injector test facility under construction at desy zeuthen," in *Proc. of the International Free Electron Laser Conference, Durham, USA*, 2000.

[27] H. Qian, J. Good, C. Koschitzki, M. Krasilnikov, F. Stephan, *et al.*, "Beyond uniform ellipsoidal laser shaping for beam brightness improvements at pitz," in *Proc. 60th ICFA Advanced Beam Dynamics Workshop on Future Light Sources (Shanghai)*, pp. 146–149, 2018.

[28] M. Gross, H. Qian, P. Boonpornprasert, Y. Chen, J. Good, H. Huck, I. Isaev, C. Koschitzki, M. Krasilnikov, S. Lal, *et al.*, "Emittance reduction of rf photoinjector generated electron beams by transverse laser beam shaping," in *Journal of Physics: Conference Series*, vol. 1350, p. 012046, IOP Publishing, 2019.

[29] S. K. Mohanty, M. Krasilnikov, A. Oppelt, F. Stephan, D. Sertore, L. Monaco, C. Pagani, and W. Hillert, "Development and characterization of multi-alkali antimonide photocathodes for high-brightness rf photoinjectors," *Micromachines*, vol. 14, no. 6, 2023.

[30] M. Gross, J. Engel, J. Good, H. Huck, I. Isaev, G. Koss, M. Krasilnikov, O. Lishilin, G. Loisch, Y. Renier, *et al.*, "Observation of the self-modulation instability via time-resolved measurements," *Physical review letters*, vol. 120, no. 14, p. 144802, 2018.

[31] G. Loisch, G. Asova, P. Boonpornprasert, R. Brinkmann, Y. Chen, J. Engel, J. Good, M. Gross, F. Grüner, H. Huck, *et al.*, "Observation of high transformer ratio plasma wakefield acceleration," *Physical review letters*, vol. 121, no. 6, p. 064801, 2018.

[32] H. Qian, M. Groß, M. Krasilnikov, A. Oppelt, F. Stephan, *et al.*, "Investigation of high repetition rate femtosecond electron diffraction at pitz," *Proc. IPAC'17*, pp. 3727–3729, 2017.

[33] P. Boonpornprasert, *Investigations on the capabilities of THz production at the PITZ facility*. PhD thesis, Staats-und Universitätsbibliothek Hamburg Carl von Ossietzky, 2020.

[34] M. Krasilnikov, P. Boonpornprasert, H.-D. Nuhn, E. Schneidmiller, F. Stephan, and M. Yurkov, "Start-to-end simulations of thz sase fel proof-of-principle experiment at pitz," tech. rep., SLAC National Accelerator Lab., Menlo Park, CA (United States), 2018.

[35] MBI, https://mbi-berlin.de/research/projects/41-implementation-of-lasers-and-measuring-techniques/topics/t1-laser-systems-for-accelerators/flat-top-uv-pulses-for-pitz.

[36] I. Will, G. Koss, and I. Templin, "The upgraded photocathode laser of the tesla test facility," *Nuclear Instruments and Methods in Physics Research Section A: Accelerators, Spectrometers, Detectors and Associated Equipment*, vol. 541, no. 3, pp. 467–477, 2005.

[37] Website Light Conversion, https://lightcon.com/product/pharos-femtosecond-lasers/, 30-07-2021.

[38] M. Krasilnikov, G. Asova, J. Bähr, C. Boulware, U. Gensch, H. Grabosch, M. Hänel, L. Hakobyan, Y. Ivanisenko, M. Khojoyan, *et al.*, "Recent electron beam measurements at pitz with a new photocathode laser system," *Proceedings of PAC09, Vancouver, BC, Canada*, 2009.

[39] G. Georgiev, N. Aftab, P. Boonpornprasert, N. Chaisueb, J. Good, M. Gross, C. Koschitzki, M. Krasilnikov, X. Li, O. Lishilin, *et al.*, "Beam preparation with temporally modulated photocathode laser pulses for a seeded thz fel," 2021.

[40] M. Krasilnikov, F. Stephan, G. Asova, H.-J. Grabosch, M. Groß, L. Hakobyan, I. Isaev, Y. Ivanisenko, L. Jachmann, M. Khojoyan, *et al.*, "Experimentally minimized beam emittance from an l-band photoinjector," *Physical Review Special Topics-Accelerators and Beams*, vol. 15, no. 10, p. 100701, 2012.

[41] I. Isaev, *Stability and performance studies of the PITZ photoelectron gun*. PhD thesis, Staats-und Universitätsbibliothek Hamburg Carl von Ossietzky, 2017.

[42] V. Paramonov, A. Naboka, A. Donat, L. Jachmann, W. Koehler, M. Krasilnikov, J. Meissner, D. Melkumyan, M. Otevrel, B. Petrosyan, *et al.*,

"The pitz cds booster cavity rf tuning and start of conditioning," in *Proceedings of Linear Accelerator Conference LINAC2010, Tsukuba, Japan*, pp. 241–243, 2010.

[43] R. Niemczyk, P. Boonpornprasert, Y. Chen, J. Good, M. Groß, H. Huck, I. Isaev, D. Kalantaryan, C. Koschitzki, M. Krasilnikov, *et al.*, "Comparison of yag screens and lyso screens at pitz," in *Proc. of the International Beam Instrumentation Conference, Shanghai, China*, vol. 10, 2019.

[44] Website Allied Vision, https://www.alliedvision.com/en/products/cameras.html, 15.04.2020.

[45] V. Miltchev, *Construction and commissioning of a Transverse Emittance Measurement System for the Photoinjector Test facility at DESY Zeuthen.* PhD thesis, Master's thesis, Humboldt-Universität zu Berlin, 2002.

[46] S. Khodyachykh, J. Bähr, M. Krasilnikov, A. Oppelt, L. Staykov, F. Stephan, T. Garvey, D. Lipk, and J. Rönsch, "Design of multipurpose dispersive section at pitz," in *28th International Electron Laser Conference (FEL 06)*, pp. 601–604, Joint Accelerator Conferences Website, 2006.

[47] J. Rönsch, "Investigations on the electron bunch distribution in the longitudinal phase space at a laser driven rf electron source for the european x-fel," 2010. Universität Hamburg, Dissertation.

[48] D. Alesini, G. Di Pirro, L. Ficcadenti, A. Mostacci, L. Palumbo, J. Rosenzweig, and C. Vaccarezza, "Rf deflector design and measurements for the longitudinal and transverse phase space characterization at sparc," *Nuclear Instruments and Methods in Physics Research Section A: Accelerators, Spectrometers, Detectors and Associated Equipment*, vol. 568, no. 2, pp. 488–502, 2006.

[49] R. Akre, L. Bentson, P. Emma, and P. Krejcik, "A transverse rf deflecting structure for bunch length and phase space diagnostics," in *PACS2001. Proceedings of the 2001 Particle Accelerator Conference (Cat. No. 01CH37268)*, vol. 3, pp. 2353–2355, IEEE, 2001.

[50] L. Kravchuk, A. Anisimov, D. Churanov, A. Donat, C. Gerth, M. Hoffmann, M. Huening, E. Ivanov, W. Koehler, M. Krasilnikov, *et al.*, "Layout of the pitz transverse deflecting system for longitudinal phase space and slice emittance measurements," *Proceedings of LINAC10, Tsukuba, Japan*, 2010.

[51] Danfysik Website, https://www.danfysik.com/, 15.04.2020.

[52] M. Krasilnikov, Q. Zhao, I. Isaev, P. Boonpornprasert, J. Good, M. Gross, H. Huck, D. Kalantaryan, O. Lishilin, G. Loisch, *et al.*, "Investigations on electron beam imperfections at pitz," in *Proc. LINAC*, vol. 16, 2016.

[53] V. Miltchev, "Investigations on the transverse phase space at a photo injector for minimized emittance," Aug 2006. Universität Hamburg, Dissertation.

[54] G. Georgiev and M. Krasilnikov, "Virtual Pepper-Pot Technique for 4D Phase Space Measurements," p. 4, 8th International Beam Instrumentation Conference, Malmö (Sweden), 8 Sep 2019 - 12 Sep 2019, Sep 2019.

[55] M. Zhang, "Emittance formula for slits and pepper-pot measurement," tech. rep., Fermi National Accelerator Lab., 1996.

[56] Y. Yamazaki, T. Kurihara, H. Kobayashi, I. Sato, and A. Asami, "High-precision pepper-pot technique for a low-emittance electron beam," *Nuclear Instruments and Methods in Physics Research Section A: Accelerators, Spectrometers, Detectors and Associated Equipment*, vol. 322, no. 2, pp. 139–145, 1992.

[57] D. Marx, J. G. Navarro, D. Cesar, J. Maxson, B. Marchetti, R. Assmann, and P. Musumeci, "Single-shot reconstruction of core 4d phase space of high-brightness electron beams using metal grids," *Physical Review Accelerators and Beams*, vol. 21, no. 10, p. 102802, 2018.

[58] E. Prat and M. Aiba, "Four-dimensional transverse beam matrix measurement using the multiple-quadrupole scan technique," *Physical Review Special Topics-Accelerators and Beams*, vol. 17, no. 5, p. 052801, 2014.

[59] Q. Zhao, M. Krasilnikov, H. Qian, F. Stephan, *et al.*, "Beam transverse coupling and 4d emittance measurement simulation studies for pitz," in *Linear Accelerator Conf.(LINAC'18), Beijing, China, 16-21 September 2018*, pp. 945–948, JACOW Publishing, Geneva, Switzerland, 2019.

[60] G. Rangarajan, F. Neri, and A. Dragt, "Generalized emittance invariants," in *Proceedings of the 1989 IEEE Particle Accelerator Conference,.'Accelerator Science and Technology*, pp. 1280–1282, IEEE, 1989.

[61] K. Floettmann, "Some basic features of the beam emittance," *Physical Review Special Topics-Accelerators and Beams*, vol. 6, no. 3, p. 034202, 2003.

[62] ASTRA Website, https://www.desy.de/ mpyflo/, 27.11.2019.

[63] C. J. Richard, "Systematic error corrections in emittance measurements," PITZ Collaboration Meeting, Zeuthen (Germany), 16 May 2023 - 17 May 2023, May 2023.

[64] M. Krasilnikov, J. Bahr, H.-J. Grabosch, J. Han, V. Miltchev, A. Oppelt, B. Petrosyan, L. Staykov, F. Stephan, and M. Hartrott, "Beam-based procedures for rf guns," in *Proceedings of the 2005 Particle Accelerator Conference*, pp. 967–969, IEEE, 2005.

[65] M. Krasilnikov, I. Isaev, G. Amatuni, G. Asova, P. Boonpornprasert, Y. Chen, J. Good, B. Grigoryan, M. Gross, H. Huck, *et al.*, "Electron beam asymmetry compensation with gun quadrupoles at pitz," *Proceedings of FEL2017 (Santa FE)*, pp. 421–423, 2017.

[66] Y. Chen, H. Qian, M. Krasilnikov, I. Isaev, Q. Zhao, P. Boonpornprasert, J. Good, and H. Huck, "Coaxial coupler rf kick in the pitz rf gun," *Proc. FEL'17*, pp. 422–425, 2017.

[67] Q. Zhao, M. Krasilnikov, I. Isaev, H. Qian, P. Boonpornprasert, G. Asova, Y. Chen, J. Good, M. Gross, H. Huck, *et al.*, "Beam asymmetry studies with quadrupole field errors in the pitz gun section," *Proc. FEL'17*, 2017.

[68] A. C. Kak and M. Slaney, *Principles of computerized tomographic imaging*. SIAM, 2001.

[69] L. A. Shepp and Y. Vardi, "Maximum likelihood reconstruction for emission tomography," *IEEE Transactions on Medical Imaging*, vol. 1, no. 2, pp. 113–122, 1982.

[70] H. Loos, P. Bolton, J. Clendenin, D. Dowell, S. Gierman, C. Limborg, J. Schmerge, T. Shaftan, and B. Sheehy, "Longitudinal phase space tomography at the slac gun test facility and the bnl duv-fel," *Nuclear Instruments and Methods in Physics Research Section A: Accelerators, Spectrometers, Detectors and Associated Equipment*, vol. 528, no. 1-2, pp. 189–193, 2004.

[71] S. F. Gull and G. Daniell, "The maximum entropy method," in *International Astronomical Union Colloquium*, vol. 49, pp. 219–225, Cambridge University Press, 1979.

[72] M. E. Daube-Witherspoon and G. Muehllehner, "An iterative image space reconstruction algorthm suitable for volume ect," *IEEE transactions on medical imaging*, vol. 5, no. 2, pp. 61–66, 1986.

[73] N. Aftab, P. Boonpornprasert, G. Georgiev, J. Good, M. Gross, A. Hoffmann, M. Krasilnikov, X. Li, R. Niemczyk, A. Oppelt, *et al.*, "Improvements in longitudinal phase space tomography at pitz,"

[74] M. Kelisani, S. Barzegar, P. Craievich, and S. Doebert, "Six-dimensional beam-envelope equations: An ultrafast computational approach for interactive modeling of accelerator structures," *Physical Review Applied*, vol. 19, no. 5, p. 054011, 2023.

[75] C. Emma, A. Edelen, M. Hogan, B. O'Shea, G. White, and V. Yakimenko, "Machine learning-based longitudinal phase space prediction of particle accelerators," *Physical Review Accelerators and Beams*, vol. 21, no. 11, p. 112802, 2018.